FERRITIN NANOCAGE AS A MAGNETIC CARRIER

A THESIS SUBMITTED TO
THE GRADUATE SCHOOL OF NATURAL AND APPLIED SCIENCES
OF
MIDDLE EAST TECHNICAL UNIVERSITY

BY

TUĞBA NUR ASLAN

IN PARTIAL FULFILLMENT OF THE REQUIREMENTS
FOR
THE DEGREE OF DOCTOR OF PHILOSOPHY
IN
CHEMISTRY

FEBRUARY 2015

Approval of the Thesis;

FERRITIN NANOCAGE AS A MAGNETIC CARRIER

submitted by **TUĞBA NUR ASLAN** in a partial fulfillment of the requirements for the degree of **Doctor of Philosophy in Chemistry Department, Middle East Technical University** by

Prof. Dr. Gülbin Dural Ünver _____
Dean, Graduate School of **Natural and Applied Sciences**

Prof. Dr. İlker Özkan _____
Head of Department, **Chemistry**

Prof. Dr. Mürvet Volkan _____
Supervisor, **Chemistry Dept., METU**

Examining Committee Members:

Prof. Dr. E. Hale Göktürk _____
Chemistry Dept., METU

Prof. Dr. Mürvet Volkan _____
Chemistry Dept., METU

Prof. Dr. Semra Kocabıyık _____
Biology Dept., METU

Prof. Dr. İnci Gökmen _____
Chemistry Dept., METU

Prof. Dr. A. Rehber Türker _____
Chemistry Dept., Gazi University

Date: 02 / 02 / 2015

I hereby declare that all information in this document has been obtained and presented in accordance with academic rules and ethical conduct. I also declare that, as required by these rules and conduct, I have fully cited and referenced all materials and results that are not original to this work.

Name, Last name: Tuğba Nur Aslan

Signature:

ABSTRACT

FERRITIN NANOCAGE AS A MAGNETIC CARRIER

Aslan, Tuğba Nur

Ph.D., Department of Chemistry

Supervisor: Prof. Dr. Mürvet Volkan

February 2015, 153 pages

There is a large focus on ferritin protein cages due to its biological importance, its behaviour as a useful platform for material synthesis and also providing chemical modification of the exterior surface to create functionality.

In this study, iron oxide nanoparticles were synthesized within the cavity of the ferritin (magnetoferritin). Non-radioactive rhenium was incorporated on the protein exterior via conjugation of histidine molecules by using glutaraldehyde crosslinker. ^{185}Re was also bound to magnetoferritin. The rhenium was bound to histidine modified magnetoferritin surface ~ 6 fold more than those bound directly to non-modified magnetoferritin surface and it has the stability of 88% ± 1.8 after 3 days in human blood serum.

The toxicity and cellular uptake experiments of prepared biomaterial were tested in MCF-10 (healthy) and MDA-MB-231 (cancerous) cell lines. The biocompatibility is still protected for apoferritin after treatment with cells for 3 days. Thus, utilizing apoferritin holds promise for cancer therapy with a reduced toxicity. The uptake of nanoparticles by the cells increased in 4 hours and cancerous cells exhibited the highest uptake than healthy cells.

The effect of iron loadings on relaxivities for MRI application and peroxidase-like activity of magnetoferritin were also investigated. r2 relaxivity and peroxidase-like properties of magnetoferritin showed an increase as the iron loadings increase. The high r2 relaxivity shows that magnetoferritin may serve as T_2 contrast agent with high efficiency.

Keywords: Magnetoferritin, Iron Oxide Nanoparticles, Rhenium Tri-Carbonyl Complex, Magnetic Resonance Imaging, Cytotoxicity.

ÖZ

MANYETİK TAŞIYICI OLARAK FERRİTİN NANOKAFESİ

Aslan, Tuğba Nur
Doktora, Kimya Bölümü
Tez Yöneticisi: Prof. Dr. Mürvet Volkan
Şubat 2015, 153 sayfa

Ferritin protein kafeslerine; biyolojik önemi, material sentezi için kullanışlı bir platform olması ve aynı zamanda fonksiyonellik kazandırmak için dış yüzeyinin modifikasyonuna olanak sağlaması açısından, büyük bir ilgi duyulmaktadır.

Bu çalışmada, ferritin iç boşluğunda demir oksit nanoparçacıkları sentezlenmiştir (manyetoferritin). Radyoaktif olmayan renyum çapraz bağlayıcı olarak glutaraldehit kullanılarak histidin molekülleri protein kafesin dış yüzeyine bağlanmıştır. ^{185}Re aynı zamanda manyetoferritine de bağlanmıştır. Histidin ile modifiye edilmiş manyetoferritine bağlanan renyum, modifiye edilmemiş manyetoferritin yüzeyine bağlanana göre ~ 6 kat daha fazla bağlanmıştır ve hazırlanan biyomateryal insan kan serumunda 3 günden sonra 88% ± 1.8 oranında kararlılığa sahiptir.

Hazırlanan biyomateryalin toksisite ve hücre içi alım deneyleri MCF-10 (sağlıklı) ve MDA-MB-231 (kanserli) hücre hatlarında test edilmiştir. Hücrelerin 3 gün boyunca işlem görmesinin ardından apoferritin için hala biyouyumluluk korunmaktadır. Yani, apoferritin kullanımı düşük bir toksisite ile kanser tedavisi için umut vadetmektedir.

Nanoparçacıkların hücrelerin içine alımı 4 saatte artmıştır ve kanserli hücreler sağlıklı hücrelere göre daha fazla alım göstermiştir.

Manyetoferritin nano kafeslerinin manyetik rezonans görüntüleme için relaksasyon ve peroksidaz benzeri aktivite özellikleri üzerine demir yükleme faktörünün etkisi incelenmiştir. r2 relaksasyon ve peroksidaz benzeri özellikleri demir yüklemesi arttıkça artış göstermiştir. Yüksek r2 relaksasyon değeri manyetoferritinin yüksek etkinlikle T_2 kontrast ajanı olarak kullanılabileceğini gösterir.

Anahtar Kelimeler: Manyetoferritin, Demir Oksit Nanoparçacıkları, Renyum Tri-Karbonil Kompleks, Manyetik Rezonans Görüntüleme, Sitotoksisite.

To my family,

especially to my spouse Fuat Aslan…

ACKNOWLEDGMENTS

I would like to express my sincere gratitude to my supervisor, Prof. Dr. Mürvet Volkan for her guidance, support, encouragement and valuable suggestions throughout this study. I learned many things from her experiences about not only science but also life. I am heartily thankful to her for everything and I also appreciate her for her patience and listening me.

I thank the members of the thesis committee Prof. Dr. E. Hale Göktürk, Prof. Dr. Semra Kocabıyık, Prof Dr. İnci Gökmen, Prof. Dr. A. Rehber Türker, Prof. Dr. Ceyhan Kayran for their invaluable time, suggestions and assistance.

I am thankful to late Prof. Dr. Mesude İşcan for her valuable guidance at the beginning of the cytotoxicity studies. These cytotoxicity studies had been carried out in Prof. Dr. Tülin Güray's laboratory, sincere thanks to her. Thanks for their comments and helps during the studies.

I would like to thank Assoc. Prof. Dr. A. Elif Erson Bensan for the donation of Human mammary epithelial cell lines and Assoc. Prof. Dr. Mayda Gürsel for the flow cytometer measurements.

Special thanks to Elif Aşık, not only for good jobs about cytotoxicity studies and learning too much thing about biology from her during my study, but also for all good times, her warm friendship and team-soul.

I would like to thank Prof. Dr. Trevor Douglas (Indiana Uni., USA) for his support and helps during the time I worked in his laboratory. Thanks to Dr. Masaki Uchida (Indiana Uni., USA) and Dr. Shefah Qazi for their helps and friendship during the relaxivity and activity studies performed in Douglas laboratory.

I would like to thank Prof. Dr. O. Yavuz Ataman and Assoc. Prof. Dr. Gülay Ertaş for their valuable ideas comments and helps.

Huge thanks all C-49 laboratory members, especially to Emrah Yıldırım, Selin Bora, Feriye Kaptı, Başak Dügencili and Erhan Özdemir. They were very helpful throughout the spectroscopy measurements. I am grateful for their helps and warm friendship.

I would like to thank my labmates from C-50 laboratory for their friendships during this study. Special thanks come for Ufuk Özgen for his moral support, friendship and encouragement. I learned too much thing with his invaluable involvement; he was the first to whom I asked suggestions and who help first whenever I need. Thanks to Ceren Uzun, my junior student and friend for her helps, friendship and kindness. I never felt alone during my studies and my energy was enlarged by her energy in the laboratory.

I would like to thank Dr. Tuğba Endoğan Tanır during this study. She helped me so much during TEM measurement in Central Laboratory in METU and thanks for her supports and friendship.

Grateful thanks go to my family; my mother Emetullah Alp, my father Mustafa Alp, my brother İsmail Emre Alp and my sister Nurgül Alp for their endless love during every step of my life, they always believe in me and support me every situation. Thanks to my little 8 month nephew Mustafa Alp, his presence gave me moral and happiness so much. Precious thanks to all my family, especially to my cousin and sister, Hilal Elmacı Okutan for her love, support, and understanding in my all life. Thanks to İdil Okutan for being in our life with her smiles.

My special thanks go to Çiğdem Acar İçhedef, Mutlu İçhedef, Sibel Kılıç, Açelya Bağlı Keskin for their love, endless support and ideas for every situation of my life. I am very lucky to have such good friends, they are always with me whenever I laugh, I cry and I need them.

My deepest thanks and gratitude go to Arzu Zabun, Sevgi Aydın, Duygu Fındık Coşkunçay and Nurcan Alkış for their valuable friendship. They were always with me whenever I need something ever since the first days in Ankara. I always found them right by my side to talk and share lots.

I am especially grateful and thankful to; Merve İçli Özkut, Onur Özkut, Hülya Kayandan, Anıl Kayandan for everything shared. I have lots of memories with them that will never be forgotten. Thank you so much for your kind friendships and your support.

My special and emotional thanks go to my dear spouse Fuat Aslan. Thank you for your endless love, support, patience and many happy moments you brought to me. If you were not in my life, I could not achieve this study. You had to endure too much 'chemistry talk' throughout my university studies. You always picked me up when I was down and I always know that you will be with me whereever I am in the world.

I also wish to thank all my colleagues in Chemistry Department of METU.

I would like to thank to TUBİTAK for supplying financial support during my PhD work.

I would like to extend my deepest due to Gaziantep University for supporting me to complete my PhD in the Chemistry Department of METU.

TABLE OF CONTENTS

LIST OF FIGURES

FIGURES

LIST OF TABLES

TABLES

LIST OF EQUATIONS

EQUATIONS

ABBREVIATIONS

MRI	Magnetic Resonance Imaging
PET	Positron Emission Tomography
SPECT	Single photon Emission Computed Tomography
XTT	2,3-bis-(2-methoxy-4-nitro-5-sulfophenyl)-2H-tetrazolium-5- carboxanilide
IC_{50}	Inhibitory Concentration
DAB	3,3′-Diaminobenzidine
PS	Phosphatidylserine
FI	Flourescence Intensity
T2	Transverse Magnetization
T1	Longitudinal Magnetization
RF	Radio Frequency
B_O	Magnetic Field
NMR	Nuclear Magnetic Resonance
TEM	Transmission Electron Microscopy
HPLC-ICP-MS	High Performance Liquid Chromatography-Inductively Coupled Plasma-Mass Spectrometer
AAS	Atomic Absorption Spectroscopy
rHFn	Recombinant Human Ferritin
SEC	Size Exclusion Chromatography
HoSF	Horse Spleen Ferritin
MWCO	Molecular Weight Cut Off
MDA-MB-231	Human Breast Metastatic Adenocarcinoma
MCF-10A	Human mammary Epithelial Cell Line
ATCC	American Type Culture Collection
FPLC	Fast Protein Liquid Chromatography

PAGE	Polyacrylamide Gel
SDS	Sodium Dodecyl Sulfate

CHAPTER 1

INTRODUCTION

1.1 An Introduction to Nanomaterials and Protein Cage Architectures

Recently, there have been many studies carried out on nanomaterials due to their different chemical and physical properties compared to those of bulk materials, thus they have many applications especially in biomedical field such as cancer therapy due to the intrinsic property of hypertherapy of the magnetic particles, drug delivery and as magnetic resonance imaging (MRI) contrast agents [1]. For especially these medical applications, soluble, biocompatible, nontoxic and effective magnetic particles should be synthesized. The critical points are the particle sizes, surface charecteristics and their magnetic responses [2,3].

In order to obtain water soluble nanoparticles, there have been many methods being used, since the dispersibility in water is the first requirement for biocompatibility. Thus, among these methods, the synthesis of the nanoparticles in water is the main concern and there are some methods commonly used such as coprecipitation method [4]. It is an economic and an easy way for the synthesis of water soluble particles, however obtaining particles with narrow size distribution is really difficult by this method [5]. Thus the surface modification of the nanoparticles with some water soluble coating materials especially silica are mostly being under investigation to be able to prepare chemically stable and homogenously dispersed particles in water [6]. There are a large number of studies performed with silica coating especially for iron oxide nanoparticles due to its magnetic properties [6,7].

These surface coating materials used for the transfer of the nanoparticles into aqueous solutions, also provides surface modification in order to attach biologically important moieties for the purposes of diagnosis and therapy [5].

For many applications, it is important to have dispersed nanoparticles, however small particles generally form agglomerates. Thus, to protect nanoparticles against degradation during synthesis, to provide stabilization and also for further functionalization, some strategies have been developed for coating them with some organic molecules [5,8]. Among these surface coating materials, small organic molecules or surfactants [8], polymers [9], and biomolecules, or coating with an inorganic material [8], metal or metal oxides [10,11] were studied and used to prevent agglomeration and improve biocompatibility.

The major difficulty in the synthesis of nanoparticles is to prepare them with narrow size distribution. The control of the size is very important since the properties of nanoparticles are significantly affected by the particle size [12]. Sizes in ranging from 1 to tens of nanometers are the dimensions those of a virus and a protein with (20—450 nm) and (5—50 nm), respectively, thus this is important especially in order to improve tissular diffusion and to have long sedimentation times [2].

Protein cage architecture is a cage like and self assembled naturally occured biological systems that are composed of different sizes of their subunits. The use of these architectures such as ferritins, virus capsids and heat shock proteins provide a size-constrained reaction environment in other words, serving as a template, thus this cage like proteins are of importance for especially inorganic mineral formation in their inner cavity with a narrow size distribution and also these systems prevent coagulation between the nanoparticles, so they can function as carriers and storage devices for metal ions for biomedical applications [13–16].

There are three distinct interfaces in a protein cage structure; these are the interior surface, the exterior surface, and the interface between subunits.

These interfaces can be modified by the help of chemical and genetic ways in order to impart multifunctionality to the prepared bionanomaterial without damaging the structure of the cage (Figure 1) [15,17].

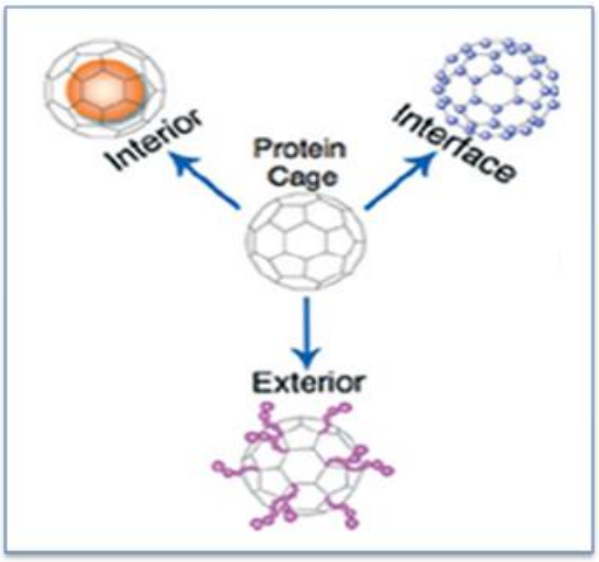

Figure 1. Schematic representation of the interfaces of a protein cage.

They also provide surface modification for the attachment of biological agents such as cell targeting ligands due to the naturally existed functional groups on the exterior surface, while the interior cavity is carrying the synthesized mineral, a kind of drug or therapeutics [18,19]. The interfaces are used to determine the effect of the protein-protein interactions to the self-assembly systems and to design multi component proteins [15,20]. Thus, protein cage like architectures have numerous advantages as mentioned.

There are a number of cage like structures that are currently being studied. A small library is given for protein shells with cage like architectures with different sizes as seen in Figure 2 [15]. These are viral capsids like cowpea chlorotic mottle virus (CCMV), ferritins and ferritin-like proteins, [21] heat shock proteins (Hsps) [22] and DNA binding proteins [23].

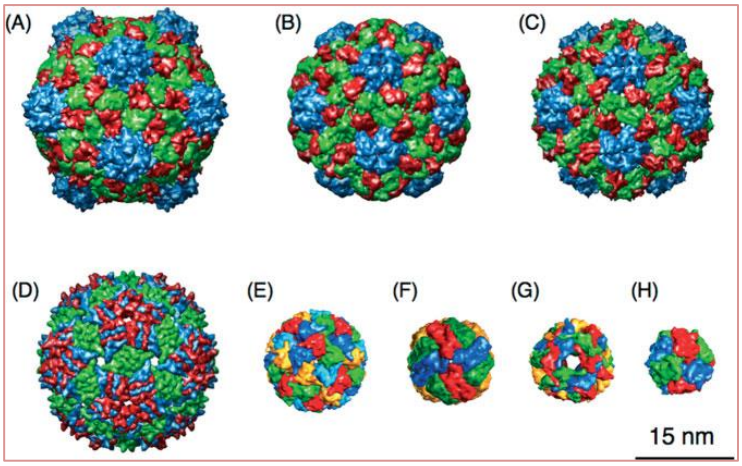

Figure 2. Images of some protein cages.

As shown in figure 2, the protein cage architectures are; A) Cowpea mosaic virus with 31 nm in diameter. B) Brome mosaic virus with 28 nm in diameter. C) Cowpea chlorotic mottle virüs with 28 nm in diameter. D) MS2 bacteriophage with 27 nm in diameter. E) Lumazine synthase with 15 nm in diameter. F) Ferritin with 12 nm in diameter. G) Small heat shock protein with 12 nm in diameter. H) DNA binding protein from starved cells with 9 nm in diameter [15].

1.2 Ferritin Protein Cage

In this study, human H-chain ferritin and horse spleen ferritin were used. Ferritin is one of the best choices of protein cages because it is already found in living systems and serves as an iron storage protein.

Thus immune system does not recognize it as a threat to a large extent when compared with the other protein cages and naked nanoparticles. It is also a very stable protein under working conditions at a very wide pH and temperature ranges to be manipulated by chemical ways [24,25].

1.2.1 Ferritin Structure and Function

As an iron storage protein; ferritins are found in biological species, such as bacteria, plants and animals [26]. The protein is abundant in liver, spleen and bone marrow [27]. Iron is in the form of hydrous ferric oxide with the similar structure of the ferrihydrite mineral $FeOOH_{(s)}$ in the protein and ferritin concentrates up to 4500 Fe atoms per cage with the intrinsic functionality of the sequestration of iron [23,28,29]. 450 kDa molecular mass of ferritin has a very robust and stable protein shell. The diameters of ferritin are 8 nm and 12 nm for inner cavity and exterior shell, respectively (Figure 3) [30,31].

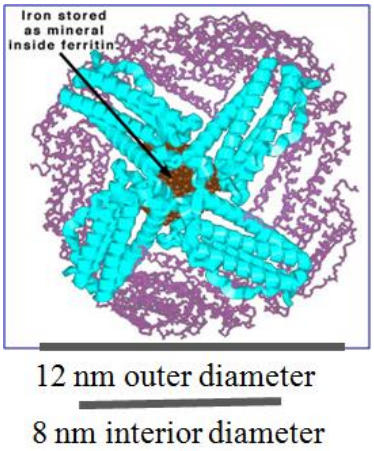

Figure 3. Schematic representation of horse-spleen ferritin and the diameters for inner and exterior cavity [32].

The packing of ferritin with 4:3:2 symmetry produces 2 types of channels that are hydrophilic and hydrophobic channels.

Around the three-fold symmetry axis, 8 pores are formed by the accumulation of acidic amino residues and these pores produce hydrophilic channels that serve as a pathway for metal ions.

Besides, around four fold symmetry axis, 6 hydrophobic channels are formed by hydrophobic amino acids accumulation that is considered to be an outlet of proton or entrance of electron, (Figure 4) [26,33–35].

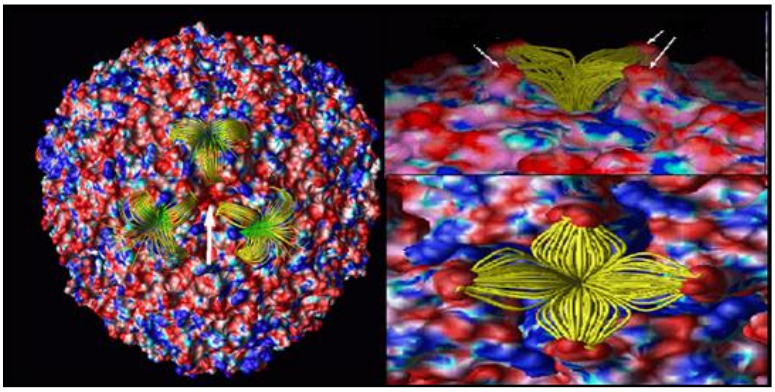

Figure 4. Illustration of pores on the exterior surface of the protein [36].

It is also composed of 24 subunits that include H- and L- polypeptide units responsible for the mineral formation in the cavity. The amount of the H- and L-units vary according to the organs and biological species. The most abundant organs in terms of H-chain subunit are; heart and brain. However, liver and spleen are rich in L subunit with 90 % ratio. H and L-subunits are about %55 similar in their amino acid sequences with the identical molecular weights [37–40].

There are di-iron ferroxidase centers in H-chain subunit that is responsible for enzymatic oxidation reaction of iron and so Fe (II) is oxidized to Fe (III) at these centers [41]. L-subunit does not have such a site but contains additional glutamate residues on the inner surface of the protein [42,43].

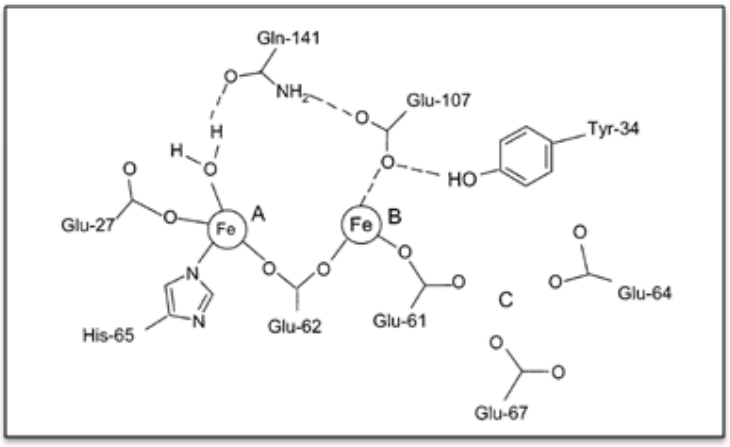

Figure 5. Ferroxidase center of human H-chain ferritin. A and B; Dinuclear iron centers, C; Nucleation site [44].

As shown in Figure 5, there are ferroxidase centers and nucleation sites with additional amino acids for human H-chain ferritin. These additional residues creates more negatively charged inner surface [44] that facilitate mineralization to form the iron core in vivo [45].

The presence of hydrophilic and hydrophobic channels also makes possible to remove iron from the cage by a slow reductive dissolution process. This empty protein is named as ‘apoferritin’ and without disturbing the structure of protein cage [12], it is used in the mineralization of some metals. In all the mineralization processes, the negatively charged interior surface creates an electrostatic gradient and this situation facilitates the metal entry from the pores and so that the mineralization beginning from the nucleation and core growth [13,46].

Besides iron oxide biomimic mineralizalion, some metal oxide nanoparticles including Mn(O)OH [47], Mn_3O_4 [48], Co(O)OH [49], Co_3O_4 [31], CdS [30], FePt [48] are synthesized for their magnetic properties in the cavity of ferritin.

The synthesis of metalic nanoparticles, such as Ni, Cu, Ag and Au for their optical, electrical and physiochemical properties such as intrinsic photoluminescence and selective catalytic activities for especially their potential biomedical, [50–53] could be achieved by the reduction reaction with a metal salt interested and a strong reducing agent like $NaBH_4$ in the ferritin cavity [46].

Ferritin has another intrinsic property that allows encapsulation of nanoparticles or drugs inside the protein. It is the capability of disassemble to its subunits and reassemble of ferritin to reform the 24-mer protein structure again while trapping the molecules within its interior, at the low pH (<3) values and then at higher pH values (>6), respectively [54,55].

As an magnetic resonance imaging (MRI) contrast agent; Gd-HPDO3A (gadolinium-[10-(2-hydroxypropyl)-1,4,7,10-tetraazacyclododecane-1,4,7-triaceticacid]) molecule [56] and also as an anti-cancer drug; cisplatin and carboplatin was encapsulated inside ferritin by utilizing this way [57].

Amine groups coming from amino acid residues like lysine [58] and carboxylic acid groups located on the ferritin exterior surface [59,60] can be used for the further modification as mentioned before. As an example, in some surface modification studies; fluorophore 4-(2-hydroxyethoxy)-7-nitro-2,1,3-benzoxadiazole (NBD) molecule was covalently coupled to the lysine groups exposed on the external ferritin shell to obtain a water soluble fluorescent nanostructure [61] and by coupling N,N-dimethyl-11,3-propanediamine molecules to the carboxyl groups of the protein, a cationized ferritin was obtained for the labeling of negatively charged cell and tissues [62].

Ferritin can be designed as a targeting agent by incorporating, on its exterior, some small peptides that have the specific binding property to some receptors. As an example for this; Douglas group has incorporated RGD-4C (CDCRGDCFC) peptide that has a binding affinity to $\alpha_v\beta_3$ and $\alpha_v\beta_5$ cell receptors.

These receptors is upregulated on tumor vasculature, so RGD-4C peptide can be used as a targeting ligand to cancerous cells and they have also showed that RGD-4C modification did not disturb the ferritin intact structure [12].

Ferritin mostly accumulates in liver, so this makes it difficult to direct ferritin to the tumor region. For this reason, in order to increase in vivo blood clearance time of ferritin, the surface was modified by dextran. Dyomics Dy-776 as a near-infrared fluorescence compound was also attached to the dextran surface to detect the nanostructure [63].

As another example for imparting multifunctonality to the ferritin cage, a triple loading process was achieved for tumor imaging. A RGD4C peptide and Cy5.5 molecules were introduced on to the surfaces of two kind of ferritin samples by genetic and chemical ways and then by utilizing the intrinsic property of ferritin protein cage allowing disassembling and then reassembling, these two kind of ferritin samples were mixed and ^{64}Cu was encapsulated within the cavity for the aim of radiolabeling by the help of reassemble method [64].

1.2.2 Iron Mineralization Mechanism in Apoferritin Protein Cage

Apoferritin can be obtained by a chemical procedure that includes firstly the reduction of Fe^{3+}, which is bound to the protein, to Fe^{2+}, then gradual removal of iron as soluble ferrous complex. This procedure is a repetitive cycles of a demineralization process until the colour change of the solution from red-brown to colourless is observed. This indicates that all the iron is removed and an empty cage is obtained [65,66].

Iron can be mineralized as superparamagnetic magnetite and/or maghemite form in the apoferritin cage, so then the final biomaterial is called ‘magnetoferritin’ [65].

In all the procedures, the magnetoferritin synthesis involves incremental additions of Fe (II) and oxidant (H_2O_2) to protein. Firstly the flow of Fe^{2+} through the hydrophilic channels of ferritin takes place, and then Fe^{2+} is oxidized to Fe^{3+} by the catalysis of ferroxidase centers and finally, the nucleation of Fe^{3+} to form Fe (III) oxide that reacts with excess Fe (II) at the nucleation sites occurs (Figure 6) [42,66].

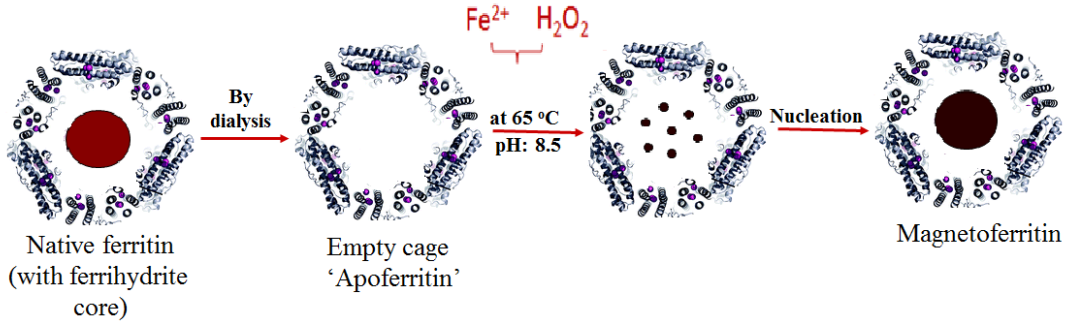

Figure 6. The reaction pathways for magnetoferritin beginning from native ferritin.

By controlling the amount of iron and protein, nanoparticles with variable particle sizes can be synthesized. If the amount of loaded iron is increased, larger cores can be obtained [66].

The mineral is synthesized with a very different magnetic property from that of native ferritin, and very similar to that of magnetite (Fe_3O_4) and maghemite (Fe_2O_3), thus producing this biocompatible ferrofluid 'magnetoferritin' is of importance in especially magnetic resonance imaging applications [65,67].

1.3 An Introduction to Radiochemistry and Radiotherapy

Radiochemistry is the field that deals with the radioactive materials. While radioactive isotopes of elements are of interest, also the non radioactive isotopes that are called stable isotopes are being under investigation by utilising the properties and

chemical reactions of the radioactive isotopes. In the radiochemistry studies, both natural and man made radioactive isotopes are being used.

The absorption of radiation within the living materials has an effect at the molecular state and leads to changes in biochemistry that provides biological outcomes.
Thus, this improves the understanding of some medical treatments such as cancer radiotherapy.

Radiotherapy is a kind of therapy using high energy radiation such as x-rays and gamma rays in order to kill or damage the cancerous tumor. This can control or stop the growth of the cancer cells, since radiation cause damage to the DNA of these cells that may also result cellular death.

In the radiotherapy treatments, whole body is exposed to the radiation, so it is also mostly possible to encounter normal cell damages as well as the tumor ones. The damaged normal cells have the ability to repair themselves however there may seen some side effects on the the body being treated.

In order to overcome this problem, there should be a treatment that easily target tumor cells and just kill these cells as possible. Therefore, nanoparticles are good candidates at this stage.

By the way of chemical or genetic modifications of the nanoparticles, radionuclides can be irreversibly binded to the surface of the nanoparticles for example; magnetic particles, by functionalization with radionuclide-binding molecules [68]. Thus, tumor could be magnetically targeted with the radiolabeled nanoparticles as carriers resulting in effective localized radiation theraphy. Thus, it is aimed to affect the part of the body in which the cancerous tumors accumulate. In imaging (diagnosis) and theraphy techniques, radioactive labeling process in which one atom in a molecule is replaced by a radioactive one is seen as a very effective way. Lists of radionuclides used in imaging and radiotherapy are given in Table 1 and Table 2, respectively.

Table 1. Some radionuclides used in radioimaging and their properties [69].

Radionuclide	Emission type	Half-life	E_{max} (keV)
^{131}I	γ (81.2%), β	8.0 days	(γ); 284,364,637
^{67}Ga	γ	78.3 h	93,184,300,393
^{111}In	γ	67.2 h	171,245
^{123}I	γ	13.2 h	159
^{99m}Tc	γ	6.0 h	140
^{18}F	Positron	1.83 h	640
^{11}C	Positron	20.4 min	960
^{13}N	Positron	9.96 min	1190
^{15}O	Positron	2.07 min	1720

Table 2. Some radionuclides with their properties used in radiotherapy [69].

Radionuclide	Emission type	Half-life	E_{max} (keV)	Range in tissue
^{186}Re	γ, β	89.2 h	(β); 1069	Max. 5 mm
^{166}Ho	γ, β	26.9 h	(β); 1853	Max. 10.2 mm
^{188}Re	γ, β	17.0 h	(β); 2120	Max. 11 mm
^{89}Sr	β	52.7 days	1463	Max. 3 mm
^{32}P	β	14.3 days	1710	Max. 8.7 mm
^{90}Y	β	64.1 h	2280	Max. 12 mm
^{225}Ac	α	10 days	5830, 5792	40-80 μm
^{211}At	α	7.2 h	5870	60-80 μm
^{213}Bi	α	45.7 min	5869	50-80 μm

Radionuclide imaging is commonly performed by; positron emission tomography (PET) and single photon emission computed tomography (SPECT) [69]. PET is a technique that can be referred as a noninvasive nuclear imaging way and produces images of the tissues and organs based on their metabolic activity.

A short lived positron emitting radioactive isotope or a radiopharmaceutical is introduced into the body as a source by either intravenous injection or inhalation way and then the amount of gamma rays emitted indirectly by this positron emitting radionuclide is measured. SPECT is the nuclear imaging technique using a gamma emitting radioisotope as a source of gamma rays and then creating a 3D information of the tissue.

While Tc is mostly preferred to be used in SPECT, the radioactive isotopes of its congener, rhenium as ^{186}Re and ^{188}Re; is the promising radiotrace for the aim of therapeutic applications. Their carbonyl complexes are of interest due to their small size providing easy labeling of biomolecules and their resistant to oxidation, chemically robust structure and low cost [70,71].

In the structure of the tricarbonyl complexes $[M(CO)_3(H_2O)_3]^+$ of Tc and Re, carbonyl groups have an inert behaviour and the labile water molecules can easily be exchanged by some functional groups such as amines and imines [72,73].

1.3.1 The Chemistry of Rhenium

For radiation therapy application, β^- emitting radioisotope of Re is one of the preferred candidates for its maximum energy of 2.12 MeV that is so useful in tumor therapy, it has the ability of damaging cancerous cells with the maximum size of 11 mm in tissue with the penetration range of 2.6 mm. On the other hand, β^- electrons are attenuated and does not damage to the adjacent organs beyond this range. In addition to these, Re emits gamma radiation with the energy of 155 keV similar to that of Tc, so it can be also used for radioimaging studies [74–76].

Non-radioactive Re occurs as a mixture of ^{185}Re (37.4%) and ^{187}Re (62.6%) in nature. The radioactive isotopes of Re that are used in medicine are ^{186}Re and ^{188}Re. The properties of the isotopes are given in Table 3.

.

Table 3. Radioactive Isotopes of Rhenium.

Isotope	Half-life	Max. B energy (MeV)	γ-Energy (keV)
^{186}Re	90 hours	1.07 (71%)	137 (9%)
^{188}Re	17 hours	2.12 (100%)	155 (15%)

1.3.2 The Chemistry of Technetium

It has been reported that there exists 22 technesium isotopes with the molecular weights between 90 and 111. Some radioactive isotopes are given in Table 4. There are not any stable isotopes of technesium.

The radioactive isotopes with the longest half life of technesium; are ^{97}Tc ($t_{1/2}$ =2.6 x 10^6 years), ^{98}Tc ($t_{1/2}$ = 4.2 x 10^6 years) and ^{99}Tc ($t_{1/2}$ = 2.1 x 10^5 years). Two isotopes are of importance that are; ^{99}Tc and its metastable nuclear isomer ^{99m}Tc [77]. The γ-emitting isomer; ^{99m}Tc is the short lived radioactive isotope and usually preferred for medical imaging. The reason for this is its suitable half-life and gamma emission energy of 141 keV [77,78].

Table 4. Some radioactive Isotopes of Technetium.

Isotope	Preparation	Half-life
^{97}Tc	^{97}Mo(d,2n)^{97}Tc	2.6 x 10^6 years
^{97m}Tc	^{96}Ru(n,2γ)^{97}Ru, ^{97m}Tc	91 days
^{98}Tc	^{98}Mo(p,n)^{98}Tc	4.2 x 10^6 years
^{99}Tc	fission of U (6.2%)	2.11 x 10^5 years
^{99m}Tc	^{98}Mo(n,γ)^{99}Mo, ^{99m}Tc	6.01 hours

1.3.3 Non-radioactive Surrogate/Isotope of ^{99m}Tc/$^{186/188}$Re

It is so difficult to study with radioactive materials in usual laboratories, since the requirement of special equipments for the necessity of safety. Thus, working with a surrogate element that possesses similar chemical properties with the radioactive isotope we are interested in may facilitate the studies.

The surrogate of Tc is rhenium and as mentioned, its chemical properties are very close to Tc. Therefore, the nonradioactive isotope of rhenium was used in all the experiments. After achieving the targeted and satisfactory results in the experiments, the method can be adapted for the radioactive isotopes of Re or Tc.

1.4 Chromatographic Separation

Chromatography is basicly a separation technique by which the constituents of a mixture are separated between two phases. Size exclusion chromatography and ion exchange chromatography methods are used in the thesis [79].

Size exclusion chromatography (SEC) is used for the separation of the biological molecules by their sizes by using a porous material, as a column packing material, serving as a molecular sieve. Two types of column materials are used in the thesis.

A superose 6 (GE Healthcare) is an agarose based, gel like material and it consists of crosslinked sugar molecules, so that the pores in the material have different pore sizes.

A sephadex medium contains cross-linked dextran gel and used to remove of small molecules from large molecules and also used for buffer exchange. G-25 fraction range is 1000-5000 Da.

Ion exchange chromatography is the separation technique based on the affinities of the constituents in a mixture to the ion exchanger. An anion exchange material was used that retains anions using a positively charged functional group in a column for the separation [79].

1.4.1 Gel Electrophoresis

Gel electrophoresis is the separation and analysis method used for the molecules such as DNA and proteins.

Its' working principle is based on the molecules' size and charge. During the separation, positively charged molecules move towards the cathode; negatively charged part and for the negatively charged molecules, the movement is towards the anode; positively charged part.

The gels that are commonly used are agarose and polyacrylamide gels. Agarose gels the natural polysaccharide polymers that are made from seaweed and these are used for the proteins larger than 200 kDa.

The electrophoresis using polyacrylamide gel is generally abbreviated as PAGE. This gel is used for the proteins between the sizes of 5 to 2,000 kDa. Pore sizes can be arranged by changing the ratios of the concentrations of acrylamide and bis-acrylamide while preparing the gel. Resolving gels are made between 6% and 15% and stacking gels that are poured on top of the running gel are made in 5% proportions. In order to compare the sizes of the analytes, there are some markers which include a mixture of known sizes [80].

Electrophoresis is divided into two categories; native and denaturing gel electrophoresis. The running conditions of the native gels are non-denaturing, that provides the maintanance of the analyte's natural structure. Thus, native gel does not need a charged denaturing agent. The molecules are separated according to their size

and their charge that are affecting the mobilities and visualized with a staining chemical. Besides, by running with the denaturing gels, the structures of the analytes are disrupted that result in unfolding of the subunits of the molecules. Thus, the linear lenght and mass-to-charge ratio affects the mobilities of the subunits. It is needed a denaturating agent and the common used one is sodium dodecyl sulfate (SDS) especially for proteins. The method is abbreviated as SDS-PAGE.

Most common gels used for the proteins are polyacrylamide gels in the presence of SDS. SDS coats the protein and makes it negatively charged, thus the separation is made by the sizes of the proteins.

1.5 Cytotoxicity Studies

Cytotoxicity is the degree of an agent of being toxic to cells, i.e. have specific destructive action on cells. Cells can give different responses to cytotoxic materials, like necrosis (losing membrane integrity) or apoptosis (generating a program of controlled cell death). Also cells may undergo rapid death (forming cell lysis) and they may stop growing and dividing (decrease in cell viability). These events can be triggered by some toxic agents, drugs or by disturbance of the cellular homeostasis in the presence of some disease. As necrosis happens, a rapid swelling of cells take place and membrane integrity is lost, after that cells shut down their metabolism and release their contents outside [81].

In the case of apoptosis, firstly some nuclear changes happen, beginning from the cell membrane damage. Then some morphological changes follow; these involve chromatin condensation, nuclear fragmentation and shrinkage. At last, cells mostly undergo necrosis, in other words; forming lysis (Figure 7) [79].

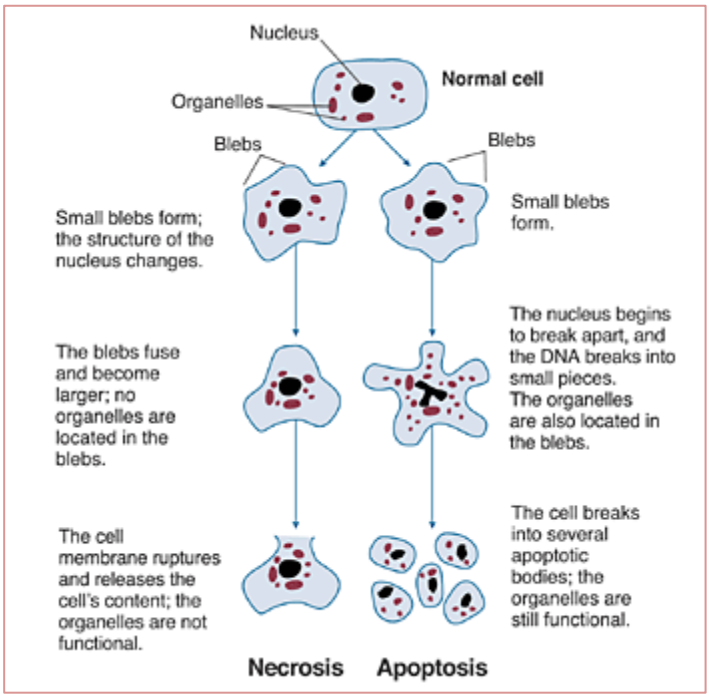

Figure 7. Structural changes of cells during necrosis or apoptosis [83].

During apoptosis, cells generate a programme for the removal of damaged cells during cell development when they experience a threat such as infections with viruses, a genetic damage progression and in the situation of aged immune cells. Therefore, apoptosis is vital for survival and development of the cells [84]. On the other hand, apoptosis also takes place for the formation of the organisms like the formation of fingers and toes of the fetus, the loss of frog tail [81]. These are the examples for the proliferation of the organisms. Thus, this balance between life and death indicates the importance of apoptosis, but any problem in its mechanism may cause cancer or other diseases.

Apoptosis and necrosis differs in every aspect; apoptosis is a genetically programmed event and in contrast to the apoptosis, necrosis takes place under the harsh conditions that damage the cells and it happens randomly when cells encounter a serous injury, since it does not programmed by the cells.

Therefore, in order to evaluate the potential of the materials or drugs to cause damage to the healthy and cancerous cells, some cytotoxicity tests and assays are being used. These assays are necessary to screen the toxicity for compounds used in medicine and to develop a therapeutic agent; may be in the form of a nanoparticle or a drug. In order to assess the cytotoxic effects to the cells, one of the common ways is measuring the cell membrane integrity and cell viability. Materials having toxic effects mostly interfere in the cell membrane integrity. Some dyes, for example, propidium iodide and trypan blue has the ability to penetrate through the damaged cell membrane and stain the intracellular contents, however it is excluded from the healthy cell membrane and staining can not be achieved (Figure 8).

.

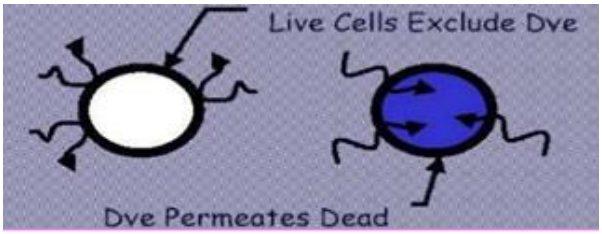

Figure 8. The situation of the live and dead cells when exposed to the dye.

1.5.1 XTT Cell Viability Assay

XTT (2,3-bis-(2-methoxy-4-nitro-5-sulfophenyl)-2H-tetrazolium-5- carboxanilide) assay is a commonly used cytotoxicity test for the determination of viable cells upon treatment with therapeutic agents or drugs and to find out the toxic concentration of the agents that are incubated with the cells by measuring the metabolic activity of the cells and membrane permeability [85].

In the assay, if the cells are incubated with XTT molecule, it penetrates into the cell membrane with the metabolic activity and is reduced to its purple formazan salt

(Figure 9) and trapped inside the cell. The coloured product is then measured spectrophotometrically at 415 nm.

Figure 9. Conversion of XTT to formazan [86].

Dead cells do not have mitochondrial activity, so XTT is not reduced and the purple formazan is not formed. By measuring the absorbance of formazan, cell viability is calculated, since the amount of measured formazan is proportional to the number of viable cells. % cell viability versus concentration graps are drawn in order to find out the IC_{50} values.

IC_{50} is the concentration of a chemical, drug or a therapeutic agent that is required for 50% inhibition in vitro. It is an important parameter leading to the estimations and designs of the other cytotoxicity assays.

1.5.2 Annexin V/PI Staining

Apoptotic cells are determined by Annexin V and PI staining. Annexin V is a cellular protein that has the affinity to bind the phosphatidylserine (PS) groups normally located on the inner surface of the cell membrane that is the cytoplasmic surface. For the detection of annexin V, a fluorescent compound; FITC (fluorescein isothiocyanide) was conjugated to annexin V that emits at 518 nm. PI; propidium iodide is called as vital dye, emits fluorescence at 617 nm [87].

In the case of apoptosis event, translocation of PS groups from inner to outer membrane takes place. Annexin V-FITC conjugate binds on PS groups from Annexin V group. This is called the early apoptotic stage.

If membrane permeability increases, PI enters inside of the cell, and then the fluorescence signal of PI is measured. This is called the late apoptotic stage (Figure 10).

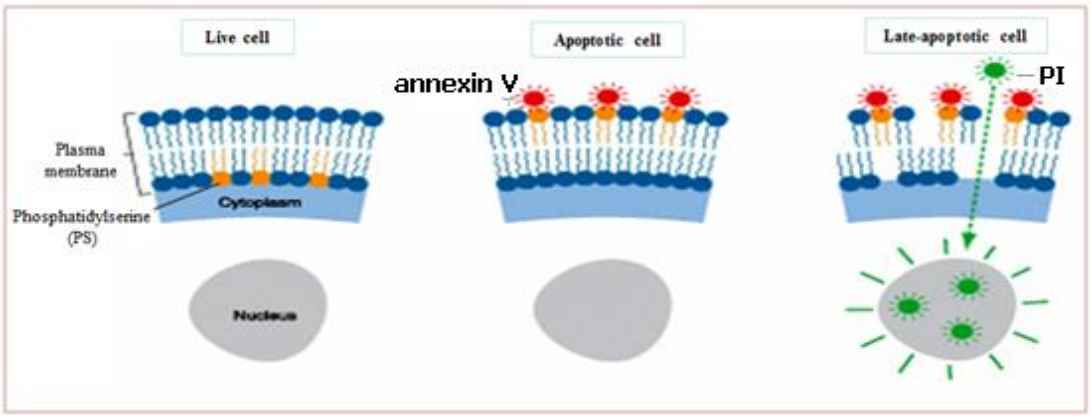

Figure 10. The annexin V and PI function during apoptosis [88].

Therefore, the incubated cells with the agents are stained with Annexin V/PI and their fluorescence signals are measured by using flow cytometer instrument. A flow cytometer measures the fluorescence intensity of the stained cells, as they flow through the beam in a suspension fluid.

The fluid carries the cells past the light one by one and signals from the individual cells are detected for the analysis. Data is given as histograms (Figure 11).

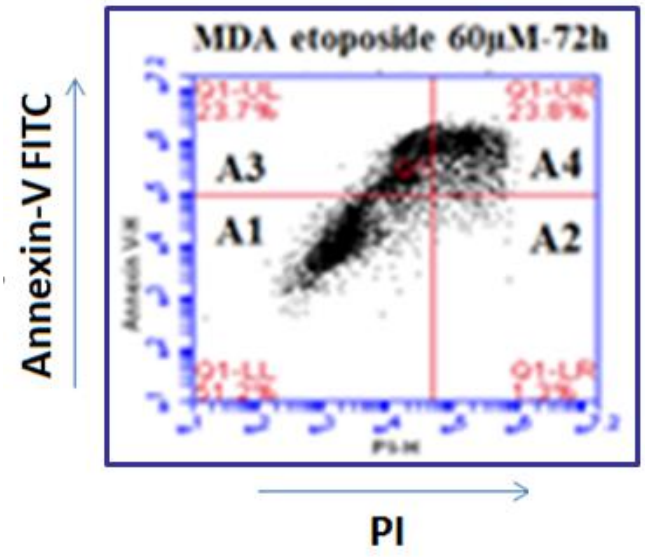

Figure 11. The cell cycle histogram for etoposide

The etoposide is a well known drug undergoing apoptosis that is used for control experiments. In the histogram, one axis shows the FI (flourescence intensity) of PI while the other is showing FI of Annexin V-FITC.

In the flow cytometry profiles; there are four areas showing the percent populations of the events. These are; Area A1: viable cells, Area A2: dead cells, Area A3: early apoptotic, Area A4: late apoptotic events. From the profiles, apoptotic cell populations (the total % population of early and late apoptosis) were obtained and drawn versus concentration (Figure 11).

1.5.3 Cellular Uptake and Prussian Blue Staining

In order to observe and quantify the nanoparticles taken up by the cells, Prussian Blue staining method and spectroscopic measurements were used in the study.

Prussian Blue staining is the method used to visualize the distribution of iron in tissue sections, since the nanoparticles synthesized includes iron in this study.
The reaction is between iron oxide nanoparticles taken up by the cells and acidic solution of ferrocyanide. The presence of acid facilitates the degradation of nanoparticles into Fe (III) ions in the cells, then Fe (III) and ferrocyanide form a blue complex called Prussian Blue and this can be observed by the use of light microscope. The reaction is shown in Equation 1.

$$K^{+} + Fe^{3+} + [Fe^{2+}(CN)_6]^{4-} \longrightarrow KFe^{3+}[Fe^{2+}(CN)_6]$$

Equation 1. The reaction between Fe (III) and ferrocyanide to form Prussian Blue.

By staining with Prussian Blue, only the iron existence in the cells can be observed, however by staining the background with a counterstain, it can be possible to observe both the iron and the cell cycle better. Nuclear Fast Red staining was used for this aim. Nuclei and cytoplasma are counterstained with this dye and the colour of the stained sections become pink to light red.

1.6 Peroxidase-like Activity

The peroxidase enzyme catalyzes the oxidation of the organic molecules by hydrogen peroxide while it is reduced to water. The nanoparticles possess the similar activity in the presence of a substrate with hydrogen peroxide [89].

As a substrate, a molecule of which oxidized form is coloured is preferred such as DAB (3,3′-Diaminobenzidine) as shown in the Figure 12.

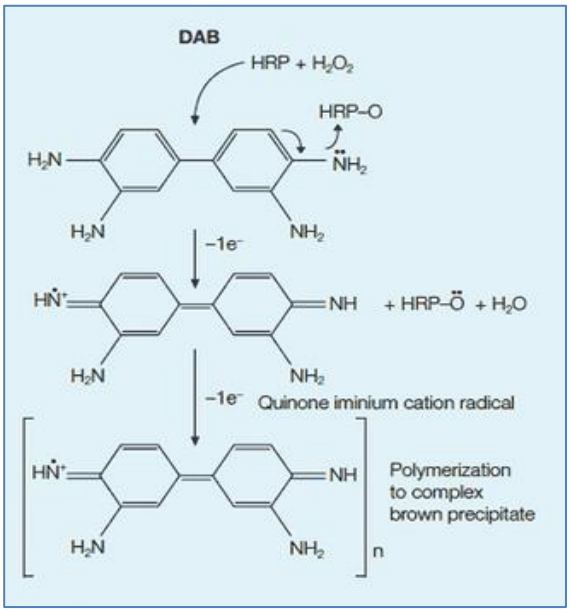

Figure 12. HRP (Horseradish peroxidase enzyme) catalyzes the oxidation of the DAB as a substrate by H_2O_2 into a brown precipitate product [90].

The peroxidase-like activity has some applications especially in biological systems. For example, it can be used to reduce the organic molecules toxicities and at the treatment of waste water with the help of the colour change [91]. Some nanoparticles have been found to scavenge the hydrogen peroxide and superoxide anion; this is also important in maintaining redox balance in biological systems by scavenging excess reactive oxygen species, since these species may cause oxidative stress and damage the cells [92].

1.7 Magnetic Resonance Imaging (MRI)

The imaging techniques concentrate on understanding of the physiology of the living organisms, early detection and assesment of the diseases [93]. For an example, macrophages are the immune system cells that are formed in the situation of an infection or damaged cell formation and these are important for the defense system.

On the other hand, macrophages are associated with some diseases such as atherosclerosis that results from plaques and arthritis, so imaging these large cells is one of the important and useful aims for assessing the state of the diseases.

Magnetic resonance imaging technique is a noninvasive and common way in clinical medicine for the visualization of the plaques and also the organs [94,95].

A magnetic field and radio frequencies are used in magnetic resonance imaging technique. Most clinical MRI is generally performed at 1.5 - 3 T (tesla) and relies on the magnetic properties of the H atom to produce images, since H has a single proton and large magnetic moment. On the other hand, the nuclei of some atoms such as sodium, fluorine can be used for imaging studies [96].

The human body is made up of around 70% H_2O and so the most abundant element is hydrogen. The proton densities in tissues are really different due to water content and environment, so tissues have different proton relaxation times from each other that are allowing clinicians to see the tissues with different image contrasts.

In order to figure out the varying contrasts of the tissues on MRI, understanding of the effect of 'free water and bound water' on the images are necessary. Free water moves disorganized and rapidly. They are not so close to the macromolecules like proteins and DNA, however bound water's motion is restricted due to the proximity to the macromolecules by hydrogen bonding.

The amounts of free and bound water in tissues vary to a large extent. The organs such as brain and liver, called soft tissues, having a large intracellular surface area, posses a huge number of bound water. However, free water exists in tissues such as glands, cysts, cerebrospinal fluid and urine to a large extent. Thus, the images appear different in these locations than the soft tissues [96]

In normal conditions, H atoms are oriented randomly if a magnetic field is not applied. When a magnetic field (Bo) is applied, H atoms align parallel to the field, on the other hand; some are aligned against the field (antiparallel) as seen in Figure 13 and so there will be a net number of protons aligned with the magnetic field direction. It is called longitudinal magnetization. The direction of the longitudinal magnetization is given in the direction of z and called Mz, conventionally.

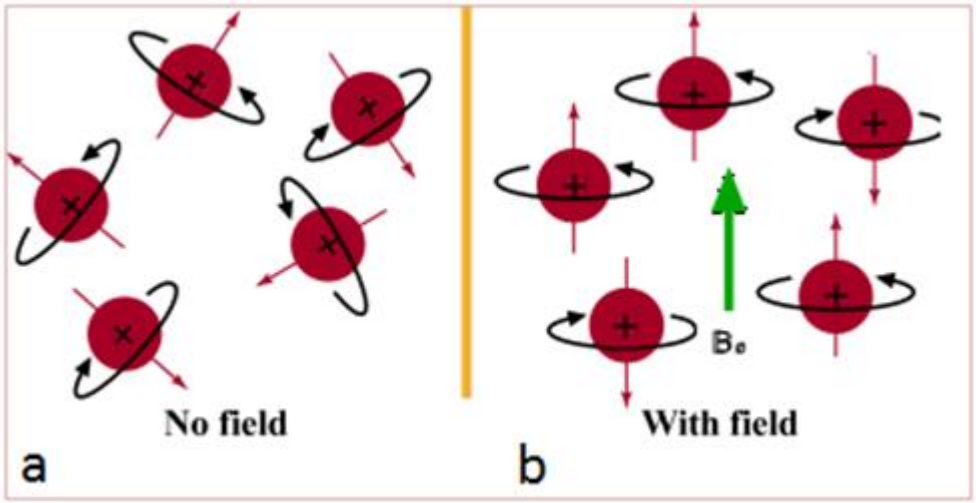

Figure 13. a. H atoms in the absence of external field, b. H atoms in the presence of external field [97].

In the application, patient lies in the MRI scanner, the hydrogen protons in his/her body lines up by using an electromagnet, for example; iron, and a large number of these aligned protons will cancel each other. Only a small number of protons are not canceled out, that is responsible for producing the image.

In the next step, a part of the body is exposed to a 90^0 radio frequency (RF) pulse. The protons in that area absorb this energy and due to their angular momentum they start to spin and wobble about the axis of the external field by the radio frequency application and so a net magnetization is developed towards the transverse plane that

is perpendicular to the magnetic field (along z axis). It is called Transverse magnetization (in xy plane) as seen in Figure 14.

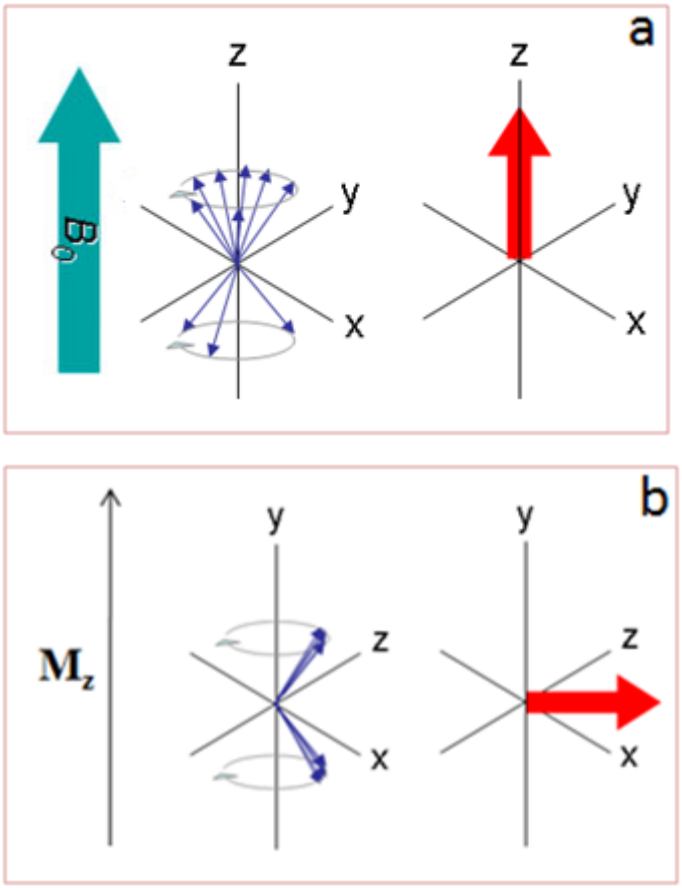

Figure 14. (a) Spinning protons wobble around the magnetization (Bo) axis. (b) Formation of transverse magnetization.

By removing the pulse application, the protons relax back to their original positions and the excess energy is released. This produces the MR signal, forming an image.

Thus, relaxation is the measurement of how fast these hydrogen atoms relax; while relaxivity is a measurement of the ability of a magnet to make the atoms relax.

Therefore, two independent processes in two directions, longitudinal relaxation and transverse relaxation, can be measured to generate an MR image as mentioned above. Relaxation in the longitudinal axis and transverse axis is called as; T1 and T2 relaxation, respectively or in other words; recovery and decay.

1.7.1 Longitudinal Magnetization and T1 contrast

After the application of RF pulse, several protons flip back to the lower energy state that is parallel to magnetic field; z axis, giving up the energy to the surroundings or in other words; the lattice. This is also called spin-lattice relaxation. So, T1 is the time at which longitudinal (Mz) component of the magnetization vector recovers the 63% of its equilibrium magnetization in the direction of Bo (Figure 15).

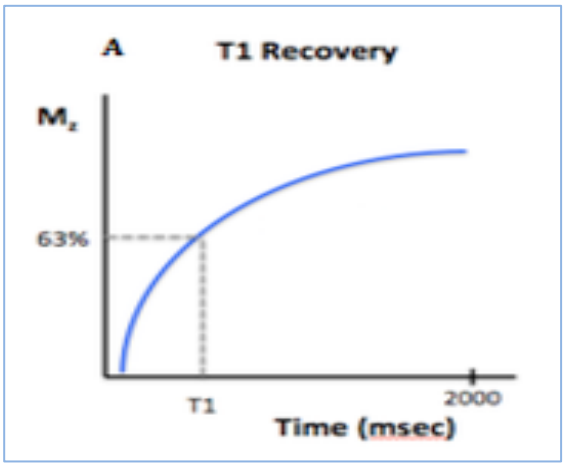

Figure 15. Gain in magnetization in z axis [98].

The recovery of magnetization occurs due to an exchange of energy between protons and their environment, so T1 is most efficient when there are interactions with the lattice and T1 relaxation times of the tissues varies with the mobility of their protons. Thus, it is a characteristic of the sample and indicates how faster the sample magnetizes again.

As mentioned before, free and bound water molecules have different relaxation rates since they have different motional energy.

Free water molecules move rapidly and they recover magnetization slowly. On the other hand, bound water has slow motions due to the coordination of the molecules and this situation lowers the average energy of the water molecules, so water nearby the molecules magnetizes faster than free water [99].

The rate of the recovery is equal to 1/T1 and called 'r1' relaxivity. The shorter T1 value results in higher relaxivity (r1) [100].

1.7.2 Transverse Magnetization and T2 contrast

After a 90^0 RF pulse, the proton magnetization converts to the transverse magnetization. Firstly, a strong signal is observed due to the spinning protons together, called in phase. After a time, due to the different spinning rates of the protons (out of phase situation) signal starts to decay through a process known as transverse relaxation [96].

In the transverse magnetization, protons perturb its neighbour protons' magnetic field with its own small magnetic field. Thus, protons start to spin at a little varying spinning rate and then spin in different and also opposite directions result in the cancellations in the magnetization in xy plane, this is a spin-spin relaxation. Then a reduction in signal in a time interval occurs. So T2 is the time taken for the signal to decay to 37% of its initial value and it is a tissue specific fenomena (Figure16) [96].

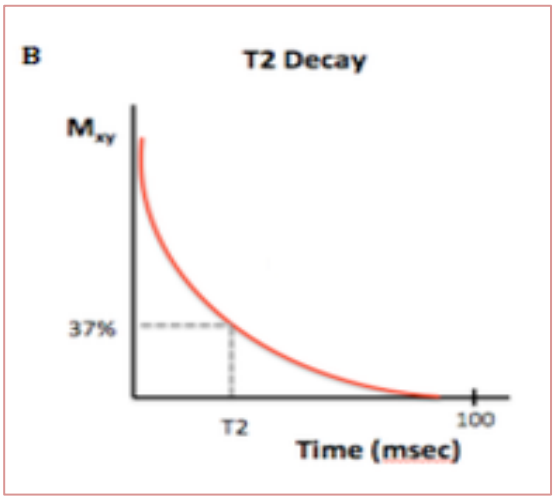

Figure 16. Loss in magnetization in xy axis [98].

Thus, T2 is the parameter that determines how fast the signal decays. The rate of the decay is 1/T2 and called ‘r2’ relaxivity.

The main parameter that affects T2 relaxation is the local magnetic field created, so it is directly proportional to the number of spins and water exchange is not required for the T2 relaxation [96].

The equilibrium, in other words longitudinal magnetization can not be determined by an easy way, for this reason, it should be converted into the transverse axis to be able to measure easily. Also these are simultaneous processes and so clinicians can choose which process to monitor (Figure17).

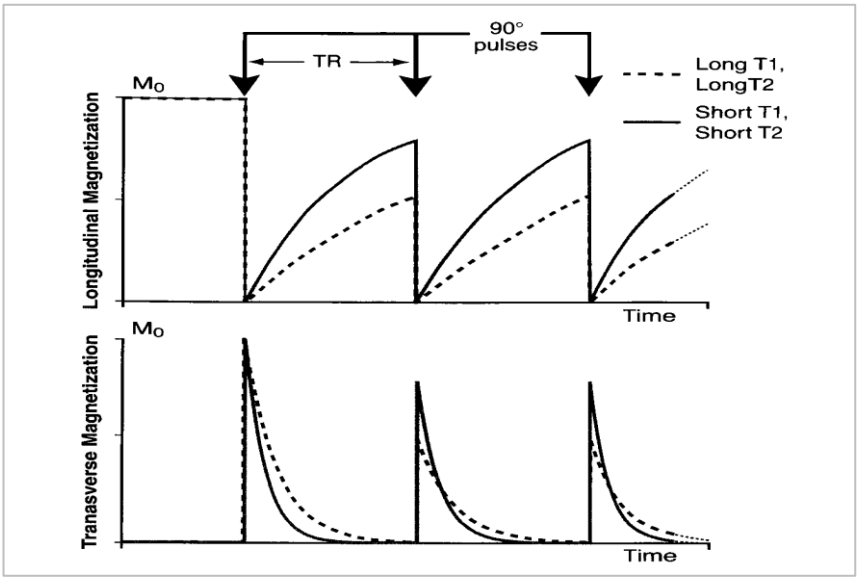

Figure 17. Simultaneous changes in longitudinal and transverse magnetizations for two different tissues shown in dotted and solid lines [96].

Depending on the process, either bright contrast (T1) or dark contrast (T2) images can be produced as seen in Figure 18. As a note, water concentration and mobility effect brightness of images.

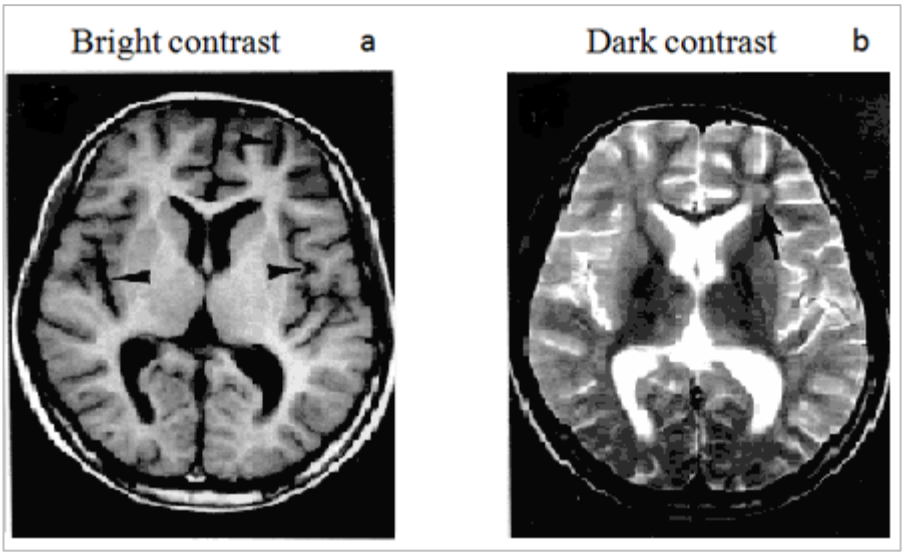

Figure 18. a. T1 enhanced MRI, b. T2 enhanced MRI [96].

1.7.3 MRI Contrast Agents

Magnetic nanoparticles have been studied and found applications in therapeutic and diagnostic techniques, in hyperthermia and magnetic drug targeting to specific sites in the body and especially in MRI [96,101,102] for many years because of their smaller sizes and unique magnetic properties [103,104]. The size of nanoparticles is of importance since size affects the magnetic properties of the particles. In addition to these, the ideal MRI contrast agent should have high relaxivity that means high contrast enhancement [104].

Thus, a large variety of magnetic particles have been synthesized by using different methods with varying sizes ranging from 10 and 3500 nm [104,105] and several synthetic and biological attempts including apoferritin [14], dendrimers [106] and phospholipid membranes [107] were reported for a well defined sized magnetic nanoparticles as mentioned before.

Paramagnetic metal ions are mostly being used contrast agents up to now due to their several unpaired electrons in their outer orbitals that create magnetic dipoles under a magnetic field.

It is important since an electron's magnetic moment is larger (~700 fold) than that of a proton. This makes nearby protons having a fluctuating magnetic field and results in an increase in proton relaxation. This is the difference between water relaxation and relaxation in the presence of a contrast agent.

There are three main parameters that affect r1 relaxivity; these are (τ_M); which is the mean residence lifetime for metal-bound water, the rotational correlation time (τ_R); which is the time it takes for molecule to tumble and (q) ; which is the number of metal-bound water molecules [108,109].

Relaxivity is directly proportional to the number of bound water molecules and rotational correlation time, however inversely proportional to the residence time for metal bound water as seen in equation and Figure 19 [99,110].

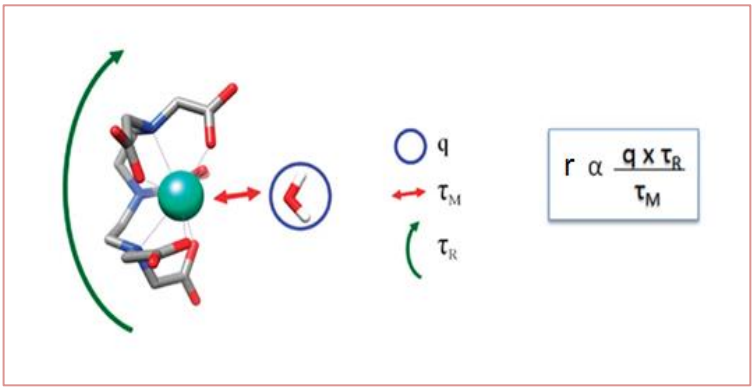

Figure 19. A schematic molecule acting MRI contrast agent and the parameters related with the r1 relaxivity [108].

These parameters helped to figure out the r1 relaxivity results for magnetoferritin system as given in results and discussion section.

There are so much paramagnetic metal ions used in MRI (Table 5), but Gd complexes are the mostly used contrast agent due to Gd metal's seven unpaired electrons and its long electron spin relaxation time that renders it an efficient T1 relaxation agent.

Table 5. A list for some of the paramagnetic metal ions [111].

Ion	Configuration	Magnetic moment
$^{24}Cr^{3+}$		3.9
$^{25}Mn^{2+}$		5.9
$^{26}Fe^{3+}$		5.9
$^{29}Cu^{2+}$		1.7
$^{63}Eu^{3+}$		3.4
$^{64}Gd^{3+}$		7.9
$^{66}Dy^{3+}$		10.6

Superparamagnetic materials are referred to as small ferromagnetic or ferrimagnetic nanoparticles with the sizes below 50 nm. Each nanoparticle contains several numbers of paramagnetic ions. As these paramagnetic ions are magnetically ordered within its structure, the total magnetic moment of the nanoparticles can be considered as one large magnetic moment that is composed of all the magnetic moments of the individual atoms that fabricate the nanoparticle and this magnetic moment value greatly exceeds that of a paramagnetic ion. This is called as superparamagnetism and this magnetization disappears after the presence of an applied magnetic field.

Based on the structure and size of the nanoparticles, superparamagnetic agents can also present the property of shortening the T1 relaxation of water; however their dominant effect is on T2 relaxation due to their large magnetic moment (Figure 20).

.

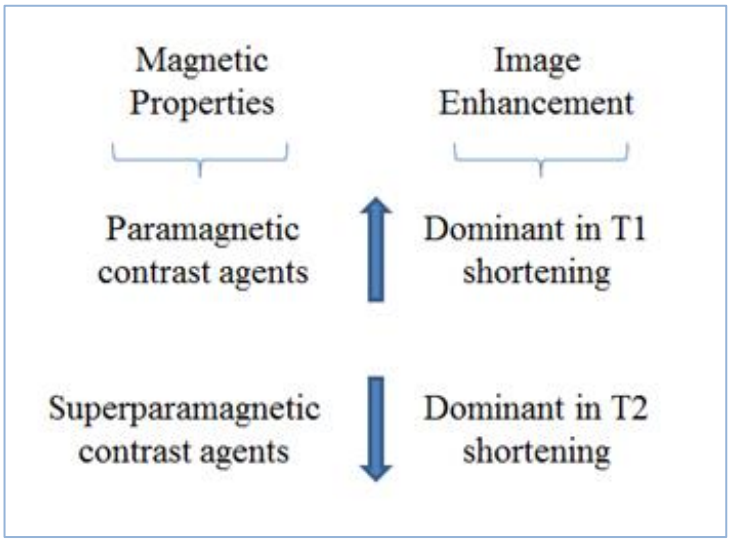

Figure 20. Comparision of MR contrast agents in terms of their magnetic characters and image enhancements.

The effectiveness of a contrast agent is characterized by their normalized r1 and r2 relaxivities over a range of contrast agent concentrations, which are 1/(T1 x Concentration) and 1/(T2 x Concentration), respectively. The relaxivity value of a sample also changes with magnetic field strength, temperature and the medium in which the measurements are carried out, so while comparing the contrast agents, these parameters should be taken in consideration.

Superparamagnetic iron oxide nanoparticles, mostly as magnetite and maghemite, are good contrast agents with the higher r2 relaxivities due to their larger magnetic moments compared with a single molecule of paramagnetic substances under a magnetic field [112,113] as mentioned and there are some contrast agents having higher relaxivity values in terms of both r1 and r2 relaxivities than Gd complexes which have been prepared and used commercially such as ferumoxtran-10, ferumoxides are in magnetite/maghemite origin [114,115]

Among the MR contrast agents, biocompatible magnetic materials prepared in the protein cage architectures especially in ferritin cages are of importance.

There are some studies that characterize ferritin-magnetic composite materials as MRI contrast agents. Magnetoferritin samples were prepared for relaxometry measurements under varying magnetic fields between 1 to 64 MHz, at varying temperatures and it was found out to be a promising MRI contrast agent with especially the higher r2 value [116,117]. In this study, the r1 and r2 relaxivity properties were investigated in order to figure out the effect of iron loading on these properties in detail and given in results and discussion part.

1.8 Aim of This Study

In this study, the main goal is to design and synthesize a functional biomaterial with the aim of diagnosis and therapy of the cancerous cells. For this purpose, apoferritin protein cages were mineralized with iron oxide nanoparticles for the use of MRI contrast agents. The exterior surface of protein cages were chemically modified by incorporating histidine molecules via glutaraldehyde crosslinker and then protein was labeled with a nonradioactive Re complex. The cytotoxicity effects were tested on healthy and cancerous cell lines. Finally, the effect of Fe loading factor on relaxivity for MRI application and peroxidase-like activity of magnetoferritin samples were investigated. In the experiments, all necessary optimization and characterization studies were carried out.

CHAPTER 2

EXPERIMENTAL PART

2.1 Instrumentation and Characterization Techniques

2.1.1 Chromatography

In this thesis size exclusion chromatography (SEC), ion exchange chromatography and gel electrophoresis separation techniques were used. Protein was passed over size exclusion chromatography before and after the mineralization and surface modification reactions for both purification and characterization of the prepared protein.

2.1.1.1 Size Exclusion Chromatography (SEC)

Akta Pharmacia (Montana State University) fast protein liquid chromatography (FPLC) system equipped with a quad-tech UV-Vis detector was used for the SEC applications and a superose 6 (GE Healthcare) columns were preferred.

The second system for the application of size exclusion chromatography was passing the samples through PD-10 desalting columns (GE Healthcare) prepacked with G-25 sephadex column (1.5 cm x 5.5 cm) and collecting the fractions as 1 mL of solutions, then measuring the absorbances of fractions at 280 nm and 410 nm.

2.1.1.2 Ion Exchange Chromatography

In the study, an anion exchange column was used for the purification and characterization of the protein before mineralization.

As an anion exchange, a mono Q column (GE Healthcare) was used. The mono Q is a hydrophilic resin containing a strong anion exchanger with the particle size of 10 μm. As the charged groups, there are $–CH_2-N^+ (CH_3)_3$ molecules on the resin and it has the capability of separation of molecules with molecular weights up to 10^7.

2.1.2 Gel Electrophoresis

Two kinds of electrophoresis methods were used; these are Native page electrophoresis and SDS page electrophoresis that were utilized under non-denaturing and denaturing conditions, respectively.

2.1.3 Bradford Assay

This method is a colorimetric protein assay that is used to determine the concentration of protein in solution. Dye Coomassie Brilliant Blue G-250 binds to the protein through its amine groups. The dye has absorbance maxima at 470 nm and 650 nm. As dye binds to protein, the absorbance maximum shifts to 595 nm and then protein concentration is determined by measuring the absorbance at 595 nm. The increase of absorbance at 595 nm is proportional to the amount of protein. The disadvantage of the method is its short linear range, from 0 mg/mL to 2 mg/mL.

There are two protocols; Standard Assay and Micro Assay, their working ranges are 0.2-1.5 mg/mL protein and 0.001-0.010 mg/mL protein, respectively [118]. In the study, standard assay protocol was used. According to the protein, Bovine serum albumin standart solutions are prepared containing a range of 0.2-1.5 mg/mL protein and 0.1 M NaCI in 10μL solutions. 10μL solutions of unknown protein sample are

prepared by dilutions and in the medium of 0.1 M NaCI. 200 μL of dye reagent is added to the standarts and samples and they are vortexed. After incubation of 5-10 min., absorbances were measured and calibration curve is prepared.

2.1.4 Transmission Electron Microscopy (TEM)

For the shape and size characterization of the protein samples, TEM (JEOL 2100 F) at the accelerating voltage of 100 kV at METU Central Laboratory and TEM (LEO 912AB) at 100 kV at Montana State University was used.
Samples were stained with 1 % uranyl acetate solution in order to visualize the protein hollow shell, since uranyl acetate produces contrast around protein cage. Uranyl acetate is a negative stain commonly used in electron microscopy. In negative staining, to produce contrast, background is stained and leaving the protein visible.

2.1.5 Nuclear Magnetic Resonance (NMR) Instrument

Magnetic characterizing measurements of the two sets of mineralized samples with the theoretical number of 500 to 5000 iron loadings were carried out on Anasazi FT-NMR 90 MHz (2.1 T) and Bruker DPX 300 MHz (7.0 T) spectrometers (Montana State University).

2.1.6 Inductively coupled plasma mass spectrometry (ICP-MS)

ICP-MS (Thermo Scientific X series) instrument with a concentric nebulizer and Peltier effect cooled spray chamber was used for the determination of ^{185}Re and ^{187}Re isotopes in the experiments. Instrumental working parameters are given in Table 6.

Table 6. Operating conditions for ICP-MS instrument.

Plasma power	1300 W
Nebulizer gas flow rate	0.84 L/min
Auxiliary gas flow rate	0.5 L/min
Plasma gas flow rate	13 L/min
Integration time for each mass	20/10 ms

ICP-MS system can be coupled with a variety of separation techniques; Here, High Performance Liquid Chromatography-Inductively Coupled Plasma-Mass Spectrometer (HPLC-ICP-MS) coupled system was used for the separation and detection (Figure 21).

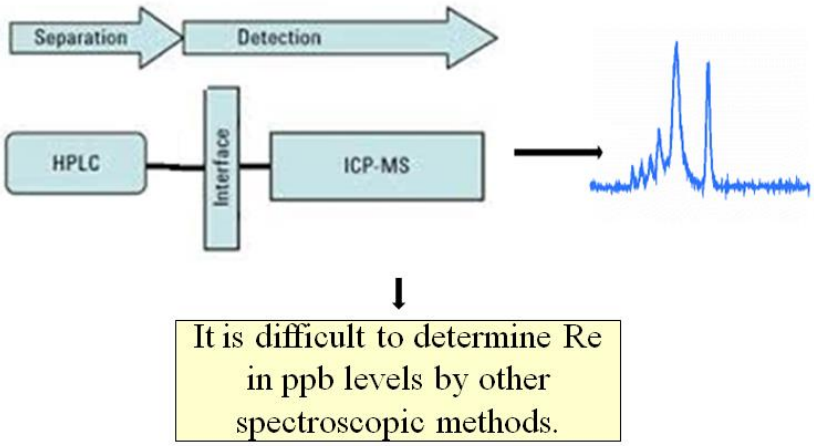

Figure 21. Illustration of the HPLC-ICP-MS instrumentation.

HPLC instrument was hyphenated to ICP-MS by use of PTFE tubing (40 cm 0.56 mm i.d.). Column outlet was connected directly to the nebulizer by passing the peristaltic pumps and Tygon connections were used at the junctions.

2.1.7 High performance liquid chromatography (HPLC)

Dionex 3000 HPLC pump with online degasser system was used for the chromatography experiments. For the injection, A Rheodyne 8125 flow injection system with 100 μL sample loop was used. Species were separated using S5 SAX anion exchange column. Instrumental working parameters are given in Table 7.

Table 7. Working conditions for HPLC instrument.

Column	Spherisorb S5 SAX
Mobile phase	5.0 mM sodium citrate in 10.0% MeOH at pH 4.5, 5.0 mM sodium citrate in 10.0% MeOH at pH 3
Flow rate	1.50 mL/min.
Injection volume	100 μL

2.2 Chemical List

In all the experimental studies, Millipore water purification system (Molsheim, France) was used to obtain deionized water of 18 MΩ cm.

All chemicals and reagents are given below with their names, formulas and manufacturer names. All are available as analytical grade and with highest purity.

2.2.1 Iron Oxide Mineralization in Protein Cages and Characterization Experiments (Bradford Asssay, AAS, SEC, TEM)

During the nanoparticle synthesis in protein cages, oxygen free water was used by sending nitrogen gas for 45 min from the solutions in interest.

i. Ammonium iron (II) sulfate hexahydrate, $(NH_4)_2Fe(SO_4)_2.6H_2O$, ≥ 99%, Sigma-Aldrich

ii. Hydrogen Peroxide, H_2O_2, ≥ 99%, Fluka

iii. Sodium Citrate, $HOC(COONa)(CH_2COONa)_2.2H_2O$, ≥ 99%, Aldrich

iv. Hepes Buffer, N-(2-Hydroxyethyl)piperazine-N′-(2-ethanesulfonic acid), ≥ 99,5 %Sigma

v. Sodium chloride, NaCl, ≥ 99%, Merck

vi. Nitric Acid, HNO_3, ≥ 70%, Sigma-Aldrich

vii. Sodium Hydroxide, NaOH, ≥ 98%, Sigma-Aldrich

viii. Bovine Serum Albumin, BSA, ≥ 98%, Sigma-Aldrich

ix. Bradford Reagent (Coomassie Brilliant Blue G-250), Sigma

x. Nitrogen Gas, N_2(g), Linde Gas

2.2.2 Surface Modification of Protein Exterior Surface and Characterization Experiment

i. Phosphate Buffer Solution, 0.1 M sodium phosphate, pH 7.0, Sigma

ii. Glutaraldehyde, $HOC(CH_2)_3CHO$, 25 %, Sigma-Aldrich

iii. L-Histidine, $C_6H_9N_3O_2$, ≥ 99 %, Sigma-Aldrich

iv. Sodium Borohydride GR for analysis, NaBH4, ≥ 96 %, Merck

v. Sodium Nitrite, $NaNO_2$, ≥ 97 %, Sigma-Aldrich

vi. Sulfanilic Acid, $(H_2N)C_6H_4SO_3H$, ≥ 99 %, Sigma-Aldrich

2.2.3 Rhenium Complex Formation and Characterization

‘Rhenium complex’ or ‘rhenium carbonyl complex’ is used instead of ‘$[Re(CO)_3(H_2O)_3]^+$’ formulation.

i. Borane ammonia complex, BH_3NH_3, 97%, Aldrich

ii. Carbon monoxide gas, CO (g), pure, OKSAN

iii. Sodium perrhenate, $NaReO_4$, 99.99% metal basis, Aldrich

iv. Phosphoric acid, H_3PO_4, 85%, Baker

2.2.4 Toxicity Tests of Re-labeled Magnetoferritin Samples on Healthy and Cancerous Cell Lines

For cell culture studies, all the reagents and chemicals were cell culture grade.

i. RPMI-1640 medium with phenol red and without phenol red, Lonza BE12-115F, Belgium
ii. Dulbecco's Modified Eagle Medium/Ham's F-12, DMEM/Ham's F12, Lonza-BE12-719F
iii. Fetal bovine serum, FBS, Sigma
iv. Gentamycin sulfate, Biological Industries
v. Hank's Balanced Salt Solution, BSS, Biochrom AG
vi. Dulbecco's Phosphate Buffered Saline, PBS, Lonza
vii. Trypsin/EDTA, Lonza BE02-007E
viii. Tryphan Blue, Biological Industries
ix. DMSO sulfoxide, Applichem
x. Epidermal Growth Factor, EGF, Peprotech, New Jersey, USA
xi. Hydrocortisone and insulin, Sigma-Aldrich, Saint Louis, Missouri, USA
xiii. 2,3-bis-(2-methoxy-4-nitro-5-sulfophenyl)-2H-tetrazolium-5- carboxanilide, XTT, Cell Proliferation Kit, Biological Industries, Haemek, Israel
xiv. Potassium ferrocyanide trihydrate, ($K_4Fe(CN)_6.3H_2O$), ≥ 98,5 %, Sigma-Aldrich
xv. 60-15mm tissue culture disc, Sarstedt
xvi. 25-cm^2 (T-25) and 75 cm^2 (T-75) tissue culture flasks 6-well-96 well microplates, cryovials (sterile, DNase RNase free, nonpyrogenic), Greiner Bio-One (Frickenhausen, Germany)

2.2.5 Peroxidase Activity and Relaxivity Measurements of Magnetoferritin Samples with Different Iron Loadings

i. Tris buffer, 1M Tris-HCl (pH 8.0), Sigma
ii. 3,3′-Diaminobenzidine, DAB, Sigma

iii. Hydrogen Peroxide, H_2O_2, ≥ 99%, Fluka

iv. Hepes (4-(2-hydroxyethyl)-1-piperazineethanesulfonic acid) buffer (50 mM Hepes, 100 mM NaCI, pH 7.5), Fluka

2.3 Experimental Procedures

2.3.1 Preparation of Protein Samples

In the experiments, ferritin samples were prepared by using two methods that were human H-chain ferritin (HFn) gene expression from e.coli and the dialysis of horse spleen ferritin (HoSF) to obtain 'apoferritin' (protein that lacks iron core).

2.3.1.1 Human H-Chain Ferritin Expression and Purification from E.coli

Cultures of E.coli, transformed with the plasmid containing the Human H-chain ferritin (HFn) gene, were grown in 1.0 L of LB (Lysogeny broth) media in the presence of 30 μg/mL of kanamycin. The E.coli from a glycerol stock was added to 1 mL of LB Broth with kanamycin (30 μg/mL) in a tube and it was placed in a shaker at 37 ºC for a few hours to overnight since a cloudy yellow media was obtained. This solution was poured into 1.0 L of LB Broth to start the growth of E.coli containing HFn and incubated at 37ºC until absorbance at 600 nm reached 0.6 a.u.
For HFn induction, IPTG (isopropyl β-D-1-thiogalactopyranoside) with the final concentration of 0.3 mM and incubated at 37 ºC over night. Then, the culture was centrifuged at 3700 g for 20 minutes to remove E. coli cells from LB media and supernatant was discarded.

Cell pellets were resuspended in 35mL of lysis buffer which is 50 mM Hepes, 100 mM NaCl, pH 7.5. 100 μL of enzyme mix of lysosome, Dnase, RNase and a pinch of deoxyribonuclease were added and the lysate was incubated at room temperature for 30 minutes followed by sonication on ice to digest and break the cell component. The solution was centrifuged at 12000g for 45 minutes to remove cell debris and supernatant was heated at 60°C for 10 min to precipitate many of the E.coli proteins followed by centrifugation at 12000 g for 20 minutes. The resulting supernatant was dialysed against 50 mM Hepes, 100 mM NaCl, pH 7.5. For the purification of protein, supernatant was subjected to size exclusion chromatography (SEC) using a

Superose 6 (GE Healthcare) column and anion exchange chromatography using a mono Q column (GE Healthcare). The fractions that contain the protein of interest were determined by SDS gel electrophoresis under native denaturing conditions using a 5% native polyacrylamide gel and protein concentration was determined by absorbtivity at 280 nm (extinction coefficient of rHFn = 1 mL/mg).

rHFn abbreviation is used instead of 'Recombinant Human H-chain Ferritin'.

2.3.1.2 Preparation of Apoferritin by Dialysis

Horse spleen ferritin (HoSF) was used for the dialysis procedure. The Fe (III) oxo-hydroxide core of HoSF was removed by reductive dissolution to form apoferritin according to established procedures. Ferritin (10 mg, 0.2 mL) was placed into a dialysis bag (MWCO of 12-14 Da) and diluted (x5) with acetic acid / sodium acetate buffer (pH: 4.5). The bag was floated into 1L of acetic acid / sodium acetate buffer (pH: 4.5) and purged with N_2 for 15-30 min. Thioglycolic acid (final concentration of 0.02 M) was added as the reducing agent into the buffer solution. After 2 hours, a further TGA (final concentration of 0.01M) was added and dialysis continues for 1 h. The buffer was refreshed, purged with N_2 for 15-30 min and procedure was repeated. The procedure was repeated until the solution becomes colourless from brown colour (Figure 22).

Figure 22. Native ferritin sample before and after dialysis process.

Protein was exhaustively dialyzed against 0.1 M NaCI solution and then, subjected to size exclusion chromatography (SEC) using G-25 Sephadex column (1.5 cm x 5.5 cm) equilibrated with 0.1 M NaCI solution. 1 mL of fractions was collected for UV-VIS masurements at 280 nm and then, the protein-containing fractions were isolated. Protein concentration was measured by the absorbance value at 595 nm in the UV-VIS spectrum according to Bradford Assay method.

For 'Horse Spleen Ferritin', HoSF abbreviation will be used from now on.

2.3.2 Cell Culture

Cell culture experiments were carried on HERA safe Class II Biological safety laminar flow. Two types of cell lines; human breast metastatic adenocarcinoma, MDA-MB-231 and human mammary epithelial cell line, MCF-10A were used.

After incubation for a determined period, the cells were subsequently analyzed for the viability and morphological changes.

2.3.2.1 Growth Conditions of the Cell Lines

Human breast metastatic adenocarcinoma, MDA-MB-231 (Monroe Dunaway Anderson - Metastatic Breast) monolayer cell lines were obtained from ATCC (American Type Culture Collection). These cells were grown in RPMI 1640 cell culture medium with phenol red containing 10% heat-inactivated fetal bovine serum (FBS) and 0.2% (50 mg/mL) gentamycin in the flasks. They were incubated in Hepa filtered Heraeus Hera Cell 150 incubator at 37°C in 95% humidified atmosphere of 5% CO_2.

Human mammary epithelial cell line, MCF-10A was kindly donated by Assoc. Prof. Dr. A. Elif Erson Bensan (METU, Ankara, Turkey). MCF-10A were grown in complete growth media containing DMEM/Ham's F: 12 cell culture medium with

phenol red containing 5% horse serum, 100 µl EGF from 100 µg/mL stock, 250 µl hydrocortisone from 1 mg/mL stock, 500 µl insulin from 10 µg/mL stock, 5 mL pen/strep and these cells were incubated at 37 ^{o}C in a 95% humidified atmosphere of 5% CO_2. The medium was changed in every 2-3 days. Cell culture experiments were carried on HERA safe Class II Biological safety laminar flow. After incubation for a determined period, the cells were subsequently analyzed for the viability, morphological changes.

2.3.2.2 Viable Cell Counting

Trypan Blue is a dye that only penetrates across the membranes of dead/non-viable cells. Viable cells are seen as small, round and retractile while non-viable cells are observed as swollen and dark blue under light microscope when trypan blue is applied. Before usage, trypan blue stock solution (0.5 % (w/v)) is diluted in 1:1 ratio with PBS.

In the experiment 20µL trypan solution and 20µL cell suspension were mixed thoroughly in order to obtain homogenous mixture. A coverslip was put on to a Neubauerhemacytometer (Bright-line, HausserScientic and Horseam, PA, USA).
10 µL of the mixture was filled in each of the two counting chambers of hemacytometer by placing the micropipette at the midside of the coverslip and the suspension was allowed to fill the space by capillary action.

Each chamber of hemacytometer consists of 9 squares each of which is 1mm^2. Coverslip sits 0,1mm over the chambers. Therefore, the volume of each square becomes 0.1mm^3 or 10^{-4} mL. In order to calculate number of cells per mL in suspension, number of cells counted in middle square is multiplied by 10^4 since the volume of 1 square is 10^{-4} mL (Equation 2).

$$\text{Cell number / mL} = \text{Average cell number of the two chambers x DF x } 10^4$$

Equation 2. The equation for the cell number/mL.

DF is; Dilution factor (dilutions were with Trypan Blue).

2.3.3 Constrained Synthesis of Iron Oxide Nanoparticles Ferritin Nanocages

Here the synthesis and characterization of two different mineral phases of iron oxides prepared in the inner cavity of the stable ferritin protein cage is presented. The two mineral systems that are examined are the ferrimagnetic mineral magnetite (Fe_3O_4) and ferrihydrite (FeOOH) and two kinds of proteins that are rHFn and HoSF were used.

2.3.3.1 FeOOH Mineralization in rHFn Protein Cage

A solution of rHFn was diluted to 0.5 mg/mL in 100 mM NACI. A deaerated solution of 12.5 mM $(NH_4)_2Fe(SO_4)_2$ was added at a rate of 100 Fe atoms/protein.min using a syringe pump (KD Scientific, Holliston, MA) until the desired loading ratio was reached. The reaction vessel was continued to stirring and left open to the air; no additional oxidant was added. Ferrihydrite minerals were synthesized with loading factors of 1000, 2000 and 3000 Fe/cage.

The H^+ generated during the reaction was titrated continously with the automatic titrator using 25 mM NaOH to maintain a constant pH 6.8 at room temperature. The air oxidation reaction of Fe (II) is shown in Equation 3.

$$4Fe^{2+} + O_2 + 6H_2O \rightarrow 4Fe(O)OH + 8H^+$$

Equation 3. The air oxidation reaction of Fe (II).

A buffer system was not used to protect any iron complex formation with the buffer components. After the mineralization, 200μL of 300 mM sodium citrate was added to chelate for the remaining free Fe in the solution and purified by SEC using Superose 6 column.

2.3.3.2 Fe_3O_4 Mineralization in rHFn Protein Cage

A solution of rHFn (0.6 mg/mL in 100 mM NaCl) was added to a jacketed reaction vessel under N_2 atmosphere to maintain an oxygen free environment. The temperature was increased to 65 ^oC by flowing water through the jacketed flask and the pH was titrated to 8.5 with 100 mM NaOH (718 Auto Titrator, Brinkmann). To achieve a theoretical Fe loading factors of 500 Fe, 1000 Fe, 2000 Fe, 3000 Fe, and 5000 Fe per protein cage, 316 μL, 632 μL, 1264 μL, 1896 μL and 3160 μL of degassed $(NH_4)_2Fe(SO_4)_2.6H_2O$ (12.5 mM) solution and stoichiometric equivalents of degassed H_2O_2 solution were used, respectively. The $(NH_4)_2Fe(SO_4)_2.6H_2O$ and H_2O_2 solutions were added simultaneously into the reaction vessel at a constant rate of 63.2 μL/min (100Fe/(cage.min)) using a syringe pump (Kd Scientific, Holliston, MA). The H^+ generated during the reaction was titrated continously with the automatic titrator using 100 mM NaOH to maintain a constant pH 8.5. The mineralization reaction in ferritin is shown in Equation 4.

$$3Fe^{2+} + H_2O_2 + 2H_2O \rightarrow Fe_3O_4 + 6H^+$$

Equation 4. The mineralization reaction in ferritin.

After the mineralization procedure, 200μL of 300 mM sodium citrate was added to chelate for remaining free Fe and the mineralized proteins were subjected to SEC analysis.

2.3.3.3 Fe_3O_4 Mineralization in Apoferritin Protein Cage

In the mineralization procedure, ferrous ammonium sulfate ($(NH_4)_2Fe(SO_4)_2 \cdot 6H_2O$) and trimethylamine N-oxide (Me_3NO) were used as Fe(II) source and oxidant, respectively. The reaction was carried out at pH: 8.6, using 3-[(1,1-Dimethyl-2-hydroxyethyl)amino]-2-hydroxy-propanesulfonic acid (AMPSO) buffer. All the solutions were deaerated with N_2 before used. Apoferritin was added to buffer solution and reaction vessel was placed in a preheated (65^oC) water bath under N_2 atmosphere. The $(NH_4)_2Fe(SO_4)_2.6H_2O$ (12.5 mM) and and stoichiometric equivalents of Me_3NO solutions (3Fe(II) : 2Me_3NO) were injected simultaneously into the reaction vessel at a constant rate of 100Fe/(cage.min). Samples with theoretical loading of 2000 Fe atoms/protein molecule were prepared. After the mineralization procedure, 200μL of 300 mM sodium citrate was added to chelate any remaining free Fe. The mineralization reaction in ferritin is shown in Equation 5.

$$3Fe^{2+} + 2Me_3NO + 4H_2O \rightarrow Fe_3O_4 + 2Me_3N + 6H^+ + H_2O$$

Equation 5. The mineralization reaction in ferritin.

2.3.4 Characterization Experiments of Fe_3O_4 Nanoparticles

2.3.4.1 Size Exclusion Chromatography

In order to get rid of the aggregation products from the mineralized rHFn, proteins were purified and analyzed by SEC by following the absorbances at 280 nm and 410 nm for protein and mineral elutions, respectively.

Centrifugation was applied to the mineralized samples at 17000 rpm for 5 minutes and the supernatant was allowed to pass through a 50 mL Superose 6 (GE Healthcare) column using Akta Pharmacia FPLC.

The flow rate was 0.5 mL/min and HEPES buffer (50 mM Hepes, 100 mM NaCl, pH 7.5) was used. Only mono-dispersed mineralized proteins were used for subsequent experiments.

The mineralized apoferritin was purified and analyzed by SEC using G-25 Sephadex column (1.5 cm x 5.5 cm) equilibrated with 0.1 M NaCI solution.

2.3.4.2 Particle Characterization

Magnetoferritin samples synthesized in rHFn were dissolved in 70 % nitric acid (1:1 v/v) and 10 fold dilutions were done with 5 % nitric acid for Atomic Absorption Spectrometry analysis to determine the iron concentration in the ferritin cages. The protein concentration of the magnetoferritin solutions were determined by the Bradford method at 595 nm using an Agilent 8453 UV-Vis Spectrophotometer.

The core size of iron oxide nanoparticles were investigated by TEM (Montana State Uni.). Samples were concentrated and transferred into deionized H_2O using centrifugal filter units (Millipore, Amicon Ultra-100K) with 100kDa M_w cut-off and the solution of magnetoferritin sample (5 μL) was air-dried on a carbon coated copper grid, and then observed by a TEM (LEO 912AB) at the accelerating voltage of 100 kV. By measuring the diameters of more than 100 particles in the TEM image, average particle size was calculated.

Mineralized apoferritin sample was negatively stained with 1% uranyl acetate solution and air-dried on a carbon coated copper grid. The core size of iron oxide nanoparticles were investigated by transmission electron microscopy (TEM, METU) operating at 80kV and the average particle size was determined by measuring the diameters of more than 100 particles in the TEM image. The purified sample was dialysed overnight against 0.1M phosphate buffer (pH 7.0) at 4^oC for subsequent experiments.

2.3.5 Surface Modification of Protein Exterior Surface and Preparation of Rhenium Carbonyl Complex

2.3.5.1 Histidine Immobilization to Magnetoferritin Protein Surface via Glutaraldehyde Crosslinker

1 mg/mL of magnetoferritin sample (theoretical loading: 2000 Fe/ferritin) synthesized in apoferritin was suspended in 0.1M phosphate buffer (0.1 M NaCl, pH 7.0) and 10 µL 2.5% glutaraldehyde solution were mixed for 15 minutes at room temperature and incubated 2 hours at 4 ^{0}C. To remove excess reagent, protein was dialysed using a 12-14 kDa molecular weight cutoff (MWCO) dialysis membrane (Sigma-Aldrich) against 0.1M phosphate buffer (0.1 M NaCl, pH 7.0). Then 1mL of (5mg/mL) freshly prepared L-Histidine solution in 0.1 M PBS buffer (0.1 M NaCl, pH 7.0) was added to the protein and mixed for 1 hour at room temperature and incubated overnight at 4 ^{0}C. To reduce the resultant Schiff bases and any excess aldehydes, 100 µL of $NaBH_4$ (final conc. 1 mg/mL) was added, reduced for 1h at 4^{0}C. By a a 0.20 µm filter syringe, solution was filtered and then dialysed via 0.1 M PBS buffer (0.1 M NaCl, pH 7.0) overnight.

2.3.5.2 Spectrophotometric Determination of Histidine

6 mL of 0.05M sodium nitrite solution was prepared with deionized water. 100 µL of hydrochloric acid was added and the mixture was kept at room temperature for one hour. 50 mg of sulfanilic acid was then added and diluted to 10 mL with deionized water. This reagent is the colouring reagent and it was used 30 min after the preparation.

Protein samples were used with the same concentrations and magnetoferritin sample that is not modified with histidine were used as control. 1.5 mL of 1M NaOH solution was added to 500 µL of protein samples and vortexed.

3 mL of colouring reagent was added to the protein solutions and absorbances were measured at 405 nm at the sixth min., using 1 M NaOH as blank.

2.3.5.3 Preparation and Charazterization of $[Re(CO)_3(H_2O)_3]^+$

$[Re(CO)_3(H_2O)_3]^+$ complex was synthesized from ^{187}Re-perrhenate ($NaReO_4$ with the nonradioactive rhenium isotope) through reductive carboxylation reaction using gaseous carbon monoxide as a source of carbonyl and amine borane (BH_3NH_3) as reducing agent, according to a literature procedure with some modifications [70].

Briefly, 10 mg of $BH_3.NH_3$ was added into a 10-mL glass vial. The vial was covered with a cap and then CO gas was passed from the vial over 10 min. The mixture of 2mL of $4.4x10^{-5}$ M ReO_4^- and 60 μL H_3PO_4 (85%) was added to the vial and incubated in a water bath at 70–80 ^oC for 15 min. H_2 gas is formed during the reaction between water and amino borane, this should be taken into consideration in order to keep the balance of H_2 gas with the help of 10-mL syringe. The optimization studies were carried out for the amounts of reagents and reaction time. In all the optimization experiments, it was seen that the maximum efficiency of complex formation was around 65%. Thus, the products from the experiments were collected and subjected to further purification and concentration with a second anion exchange resin with the same mobile phase.

HPLC-ICP-MS system (Dionex, LPG-3400A model HPLC equipped with Thermo Electron Corporation X Series model ICP-MS system) was used with S5 SAX anion exchange column as stationary phase to characterize rhenium tricarbonyl complex and the other species to be formed as by-products. 5.0 mM sodium citrate in 10.0% MeOH at pH 4.5 and 5.0 mM sodium citrate in 10.0% MeOH at pH 3.0 were used as mobile phases at the flow rate of 1.50 mL/min.

2.3.5.4 Re Labeling of Histidine Immobilized Magnetoferritin

The pH of rhenium complex solution was adjusted to 6-7 with 0.2M NaOH. Then 500 μL of histidine conjugated protein and 500 μL of rhenium complex solution were mixed and placed into a shaker thermostated at 60 °C for 40 minutes.

Labeled protein was purified by G-25 Sephadex column (1.5 cm x 5.5 cm) with 0.1 M PBS buffer (0.1 M NaCl, pH 7.0) and 1 mL of fractions were collected for UV-Vis and ICP-MS measurements to determine the protein and Re concentrations in the fractions.

2.3.5.5 Stability Test in Human Blood Serum

To test the serum stability of rhenium labeled magnetoferritin, the labeled protein was suspended in (1:1) human blood serum and 0.1 M PBS buffer (0.1 M NaCl, pH 7.0) in separate experiments simultaneously. Samples were dialysed against 0.1 M PBS buffer (0.1 M NaCl, pH 7.0) for 72 h. Aliquots of samples were removed after 12, 24, 48 and 72 h from the dialysis bag and suspected to ICP-MS for Re determination.

2.3.5.6 Gel Electrophoresis

2.3.5.6.1 Native Page Electrophoresis

The solutions and their volumes for a 5mL native page stacking gel are given in Table 8.

Table 8. The solutions and their volumes for native page stacking gel.

0.375 M Tris-HCl pH=8.8	4.275 mL
Acrylamide/Bis-acrylamide (30%/0.8% w/v)	670 µL
10% (w/v) ammonium persulfate (AP)	50 µL
TEMED	5 µL

The solutions and their volumes for a 10mL native page resolving gel are given in Table 9.

Table 9. The solutions and their volumes for native page resolving gel.

Acylamide percentage	6%	8%	10%	12%	15%
Acrylamide/Bisacrylamide (30%/0.8% w/v)	2 mL	2.6 mL	3.4 mL	4 mL	5 mL
0.375 M Tris-HCl (pH=8.8)	7.89 mL	7.29 mL	6.49 mL	5.89 mL	4.89 mL
10% (w/v) ammonium persulfate (AP)	100 µL	100 µL	100 µL	100 µL	100 µL
TEMED	10 µL	10 µL	10 µL	10 µL	10 µL

2.3.5.6.2 SDS-PAGE Electrophoresis

The solutions and their volumes for about 3 mL SDS page stacking gel are given in Table 10.

Table 10. The solutions and their volumes for SDS page stacking gel.

0.375 M Tris-HCl pH=8.8, Acrylamide / Bis-acrylamide (30% / 0.8% w/v)	3 mL
10% (w/v) ammonium persulfate (AP)	40 µL
TEMED	20 µL

The solutions and their amounts for about 7 mL SDS page resolving gel are given in Table 11.

Table 11. The solutions and their volumes for SDS page resolving gel.

Acrylamide / Bisacrylamide (30% / 0.8% w/v)	2,8 mL
1,5 M Tris-HCl (pH=8.8) + 10% SDS	1,9 mL
10% (w/v) ammonium persulfate (AP)	40 µL
TEMED	20 µL
Water	2,3 mL

The constituents of the sample buffer and running buffer for both of the electrophoresis types are given in Table 12.

Table 12. The constituents of the sample buffer and running buffer.

Sample Buffer:	Running Buffer:
62.5 mM Tris-HCl, pH 6.8	(should be ~ pH 8.3)
25% Glycerol	25 mM Tris
1% Bromophenol Blue	192 mM Glycine

Appropriate volumes of resolving gel solution are prepared with the given volumes of the constituents above and pipeted into the gap between the glass plates of gel casting. Rest of the space is filled with isopropanol and the solution is allowed for 20-30 min for a complete gelation.

While the resolving gel is gelating, the stacking gel solution can be prepared with the given volumes of the constituents above. Isopropanol solution is poured out and stacking gel solution is pipeted into the gap. The comp is inserted and solution is allowed to gelate for 20-30 min.

Sample is not heated; if the method is native page electrophoresis and if the method is SDS-PAGE, sample is heated in boiling water for 5 min. Sample is mixed with sample buffer and loaded to the gel. The voltage is adjusted to 35 mV to run the electrophoresis. After the electrophoresis, the gel was stained overnight with 0.25% Coomassie Brilliant Blue R-250, followed by destaining with an aqueous solution containing 7% (v/v) acetic acid and 5% (v/v) methanol.

2.3.6 Biological Tests for Prepared Biomaterial

2.3.6.1 XTT Cell Viability Assay

Re-labeled magnetoferritin samples of varying concentrations were prepared and the samples were subjected to centrifugation at 17000g for 5 min. prior to the treatment

to cell lines. The cytotoxic effects of the prepared nanoparticles in MDA-MB-231 and MCF-10A cell lines were investigated with the Cell Proliferation XTT Kit.

The cells were seeded into 96 well plates and left for 24hours to let them grow. Then, medium was changed and 90 µL of fresh complete medium was added. 10 µL solutions of protein samples with the concentrations of 0.5, 1, 1.5, 2 mg/mL were added and left for 24-48-72hours incubation in CO_2 incubator at 37°C.

XTT reagent and activation reagent were defrosted at 37°C and reaction mixture was prepared by adding 0.1 mL activation reagent containing PMS (N-methyl dibenzopyrazine methyl sulfate) to 5 mL XTT reagent. From the reaction mixture, 50 µL aliquots were added to each well. Following the incubation with XTT reagent mixture for 20 hours in CO_2 incubator at 37 ^{0}C, the absorbance of the dye was measured at a wavelength of 415 nm with Bio-tek ELISA reader linked to a PC supplied with KC Junior program. 3 independent experiments were performed and each one had triplicate wells. The inhibitory concentration (IC_{50}) values were determined by Graph Pad Prism Version5 according to dose-response curve drawn according to percent viability. The 96 well plate representation of XTT assay is shown in Figure 23.

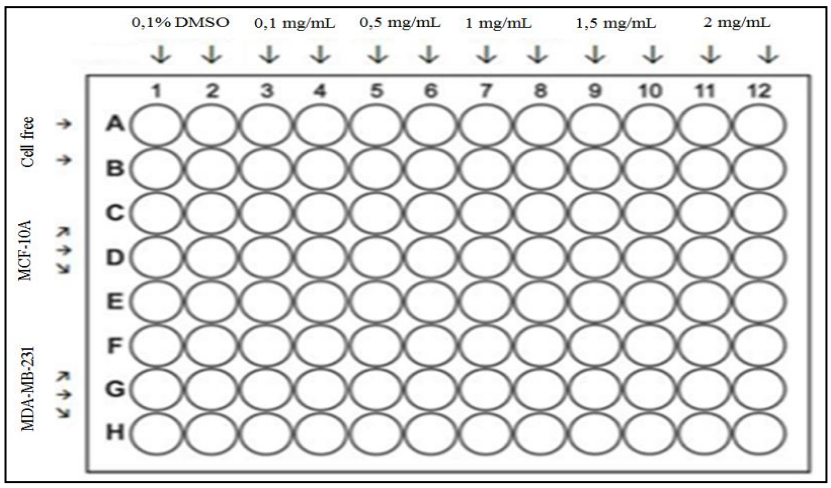

Figure 23. The scheme of XTT assay organization in 96-well plate.

The first two rows are cell free, the next three rows and the following three rows were incubated with MCF-10A and MDA-MB-231, respectively. The treatment of rhenium labeled magnetoferritin samples with different concentrations were performed as indicated.

The cell free wells were used as blank to eliminate interferences at 415 nm. 0.1 % DMSO, the cell growth medium, treatment was used as control.

The results were expressed in terms of percentage cellular viability with respect to concentrations and calculated with the formula given in Equation 6.

$$\%\text{Cell Viability} = \frac{\text{Avg.OD}_{415}\text{ of treated well (with cell)- Avg.OD}_{415}\text{ of treated well (without cell)}}{\text{Avg.OD}_{415}\text{ of control well (with cell)- Avg.OD}_{415}\text{ of control well (without cell)}} \text{ x } 100$$

Equation 6. The formula for Cell Viability %.

The flow chart of the procedure is shown in Figure 24 as a summary of the XTT assay.

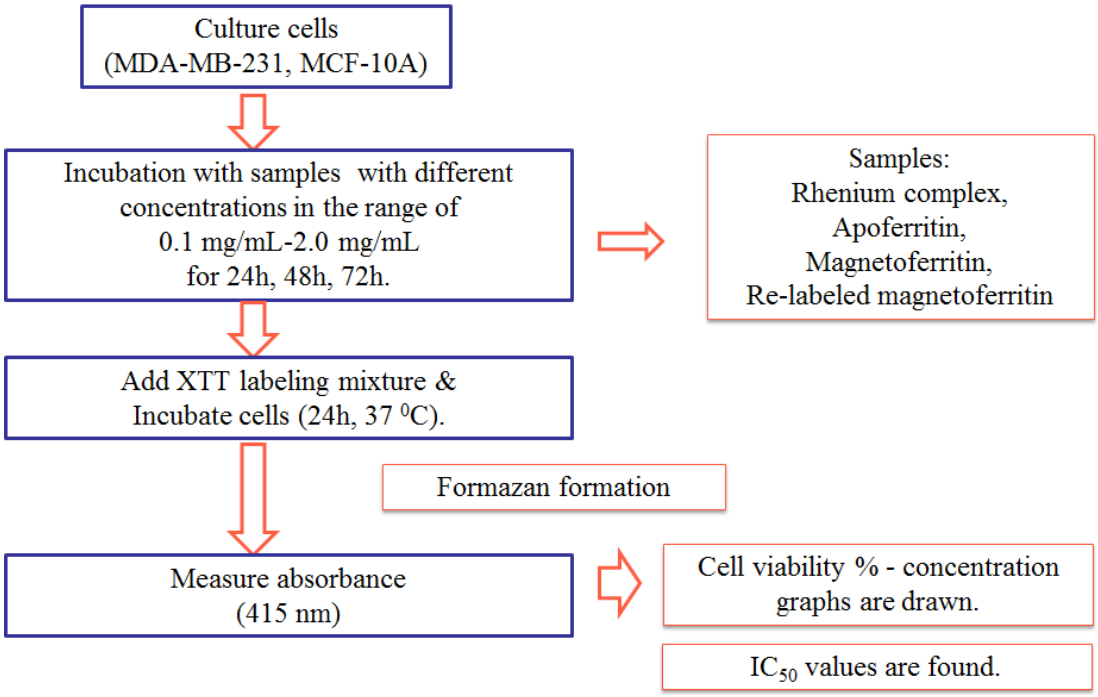

Figure 24. The flow chart of the XTT assay.

2.3.6.2 Annexin V-FITC/PI Staining

The half maximal inhibitory concentration (IC_{50}) value was determined from the cell viability XTT assay and the subsequent experiments were designed according to IC_{50} value.

The apoptotic effects of the prepared nanoparticles in MDA-MB-231 and MCF-10A cell lines were investigated by using FITC Annexin V Apoptosis Detection Kit with PI (Biolegend, USA).

MDA-MB-231 and MCF-10A cells (1×10^6) were treated with Re-labeled magnetoferritin for 24, 48, 72h and stained with PI and fluorescein isothiocyanate (FITC)-conjugated Annexin-V using the Annexin V-FITC Apoptosis Detection Kit (Biolegend).

The stained cells were incubated on ice and a minimum of 10,000 events were acquired by using BD C6 flow cytometer (Becton-Dickinson, Franklin Lakes, NJ) and absorbances were recorded at 518 nm and 617 nm for Annexin V-FITC and Propidium iodide, respectively.

From the Annexin V signal (early apoptotic phase), PI signal alone (necrotic phase) or both (late apoptotic phase), the percentage of cells for each event was obtained by using the Cell Quest Pro software (Becton- Dickinson).

The flow chart of the procedure is shown in Figure 25 as a summary of the Annexin V-FITC/PI Staining.

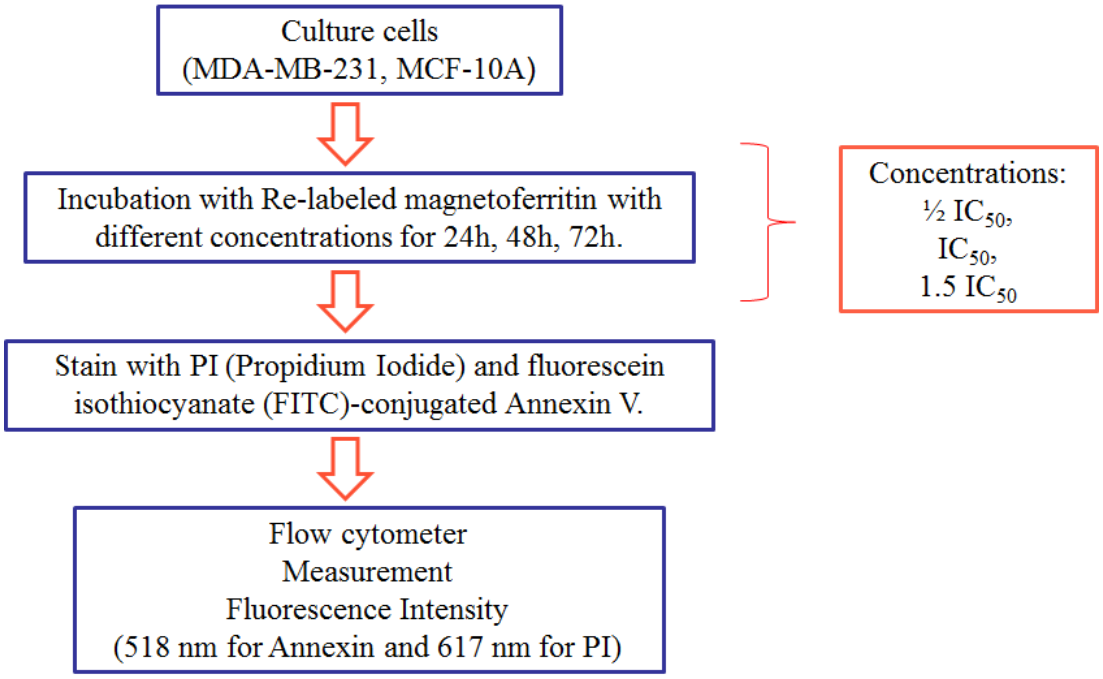

Figure 25. The flow chart of the Annexin V-FITC/PI Staining.

2.3.6.3 Uptake Studies

To investigate the uptake route, $2x10^6$ cells were plated in 60x15 mm culture dish. After 24h of incubation, Re-labeled magnetoferritin nanoparticle samples were added to each culture dish with the final concentration of IC_{50} value (1 mg/mL).

Re-labeled nanoparticles were incubated for 4h, 24h and 72h in separate experiments in CO_2 incubator at 37°C and then cells were washed at least five times with PBS and trypsinized. The cell suspensions were collected in 15 mL falcon tubes.

Cells were counted by using trypan blue dye under light microscope as described above. For the determination of rhenium content, cells were digested with concentrated HCl acid overnight. Then, samples were 10 fold diluted with deionized water and subjected to ICP-MS (Thermo X series) analysis.

The flow chart of the procedure is shown in Figure 26 as a summary of the uptake studies.

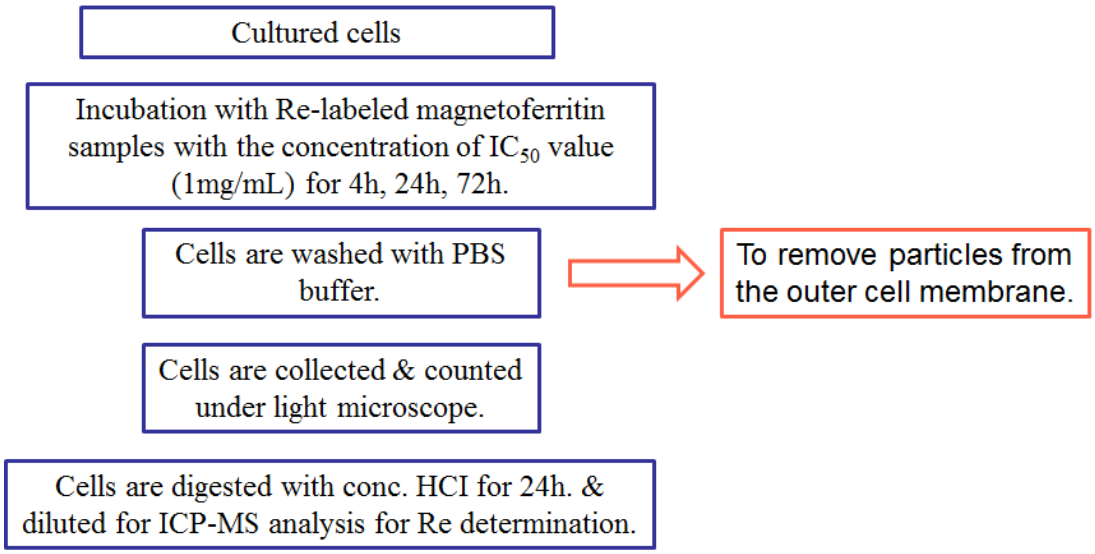

Figure 26. The flow chart of the uptake studies.

2.3.6.4 Prussian Blue Staining

MDA-MB-231 and MCF-10A cells were incubated with Re-labeled magnetoferritin samples at 37°C in 5% CO_2 atmosphere for 24h. After incubation, cells were washed two times with DPBS to remove the nanoparticles excluded from the cells and collected using 0.25% trypsin.

The cells were fixed with 4% of formaldehyde then washed with distilled water three times. Working solution for staining was prepared by mixing 5% potassium ferrocyanide (stored in dark bottle) and 5% hydrochloric acid solutions at a ratio of 1:1 just before use for staining.

Fixed cells were incubated with the working solution for 30 min at room temperature, washed by distilled water three times, and counterstained with Nuclear Fast Red for 5 min.

The flow chart of the procedure is shown in Figure 27 as a summary of the Prussian Blue Staining.

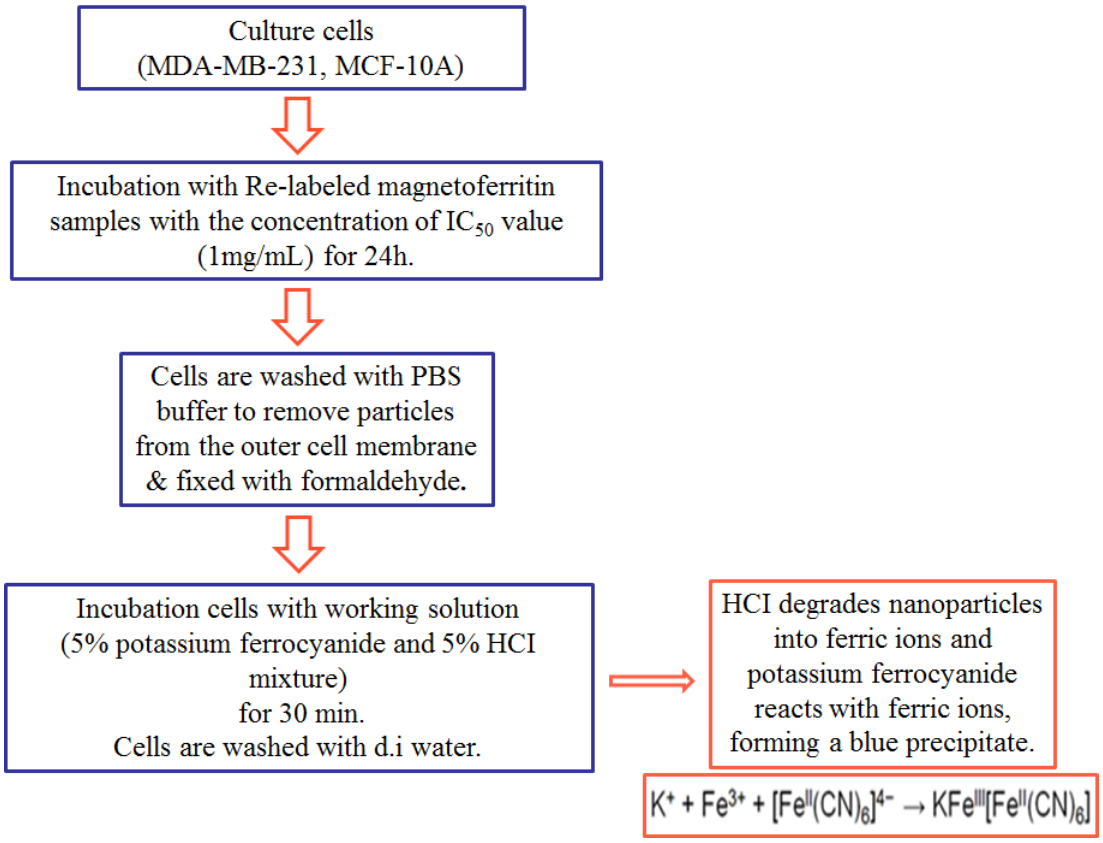

Figure 27. The flow chart of the Prussian Blue Staining.

The flow chart of the procedure is shown in Figure 28 as a summary of the Prussian Blue Staining together with counterstaining with nuclear fast red.

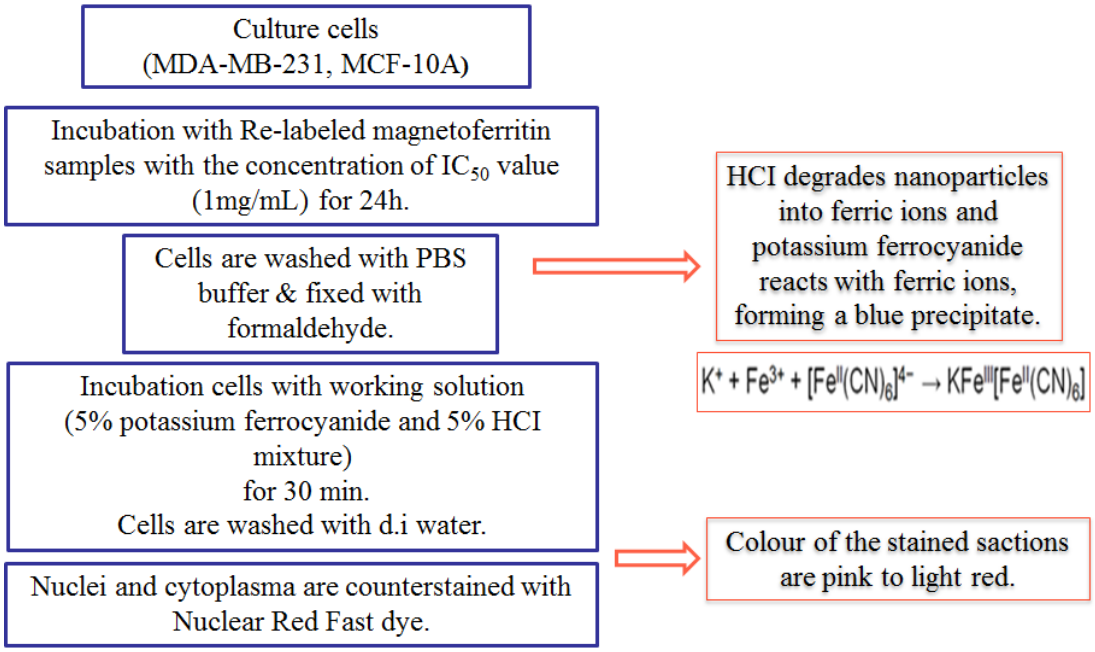

Figure 28. The flow chart of the Prussian Blue Staining and Counterstaining.

2.3.7 Peroxidase-like Activity and Relaxivity Measurements of Magnetoferritin Samples with Different Iron Loadings

2.3.7.1 Peroxidase-like Activity

Peroxidase activity tests were carried out on magnetoferritin samples with 798 Fe/cage, 2590 Fe/cage and 5329 Fe/cage with using the same concentrations of protein and same concentrations of iron, in separate experiments. Samples were dialyzed against Tris buffer (50 mM Tris-HCI, pH: 7.5) overnight before peroxidase assays. Magnetoferritin solutions were mixed with DAB (Sigma) as the substrate in Tris buffer (50 mM Tris-HCI, pH: 7.5). All the reactions were monitored at 455 nm using an Agilent 8453 UV-Vis Spectrophotometer for 60 minutes, immediately after adding H_2O_2 at room temperature. Final concentrations were 0.47 mM DAB and 1% H_2O_2 in Tris buffer. For the control experiments, apoferritin sample and DAB solution without protein sample were used at the same conditions.

To investigate the mechanism, assays were carried out under standard reaction conditions as described above by varying concentrations of DAB at a fixed concentration of H_2O_2.

2.3.7.2 T_2 and T_1 Relaxivity Measurements

All magnetoferritin samples were diluted with hepes buffer (50 mM Hepes, 100 mM NaCI, pH 7.5) to yield a dilution series for the measurements by using both of the instruments that are working under 90 MHz and 300 MHz.

CHAPTER 3

RESULTS AND DISCUSSION

3.1 Purification and Characterization of rHFn After Chromatography and Gel Electrophoresis

In order to purify the recombinant protein cages that were obtained by gene expression, firstly the protein was subjected to SEC and the protein fractions were collected for the second purification using anion exchange column. The collected protein fractions were subjected to the anion exchange column and then the fractions are kept for the electrophoresis analysis. From the electrophoresis results, the purified fractions were used in all the subsequent experiments.

SEC profiles after the gene expression of rHFn were obtained and given in Figure 29 as follows.

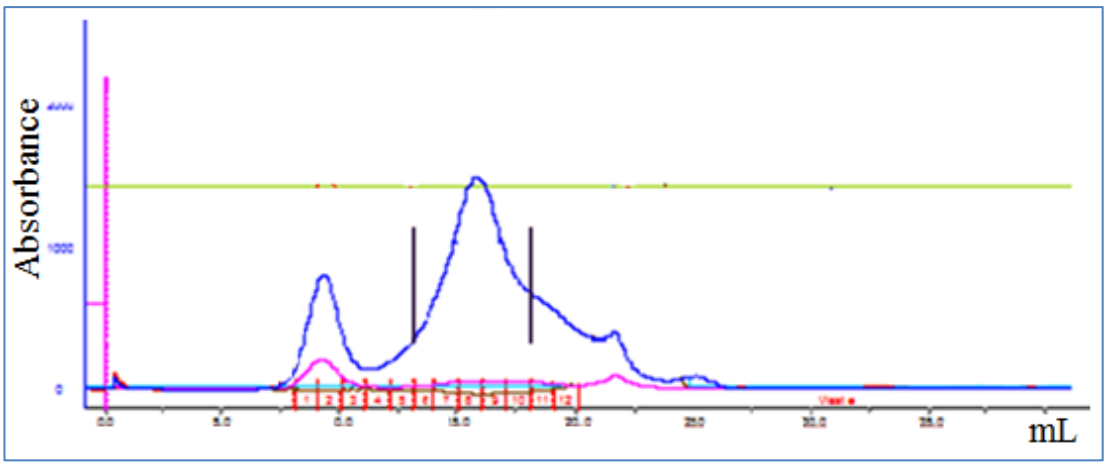

Figure 29. SEC profile of rHFn after gene expression.

Blue and pink peaks belong to the absorbances at 280 nm and 410 nm for protein and iron mineral, respectively. The fractions at the 6, 7, 8, 9, 10 mL as shown with the straight lines were collected and subjected to the anion exchange column (Figure 30).

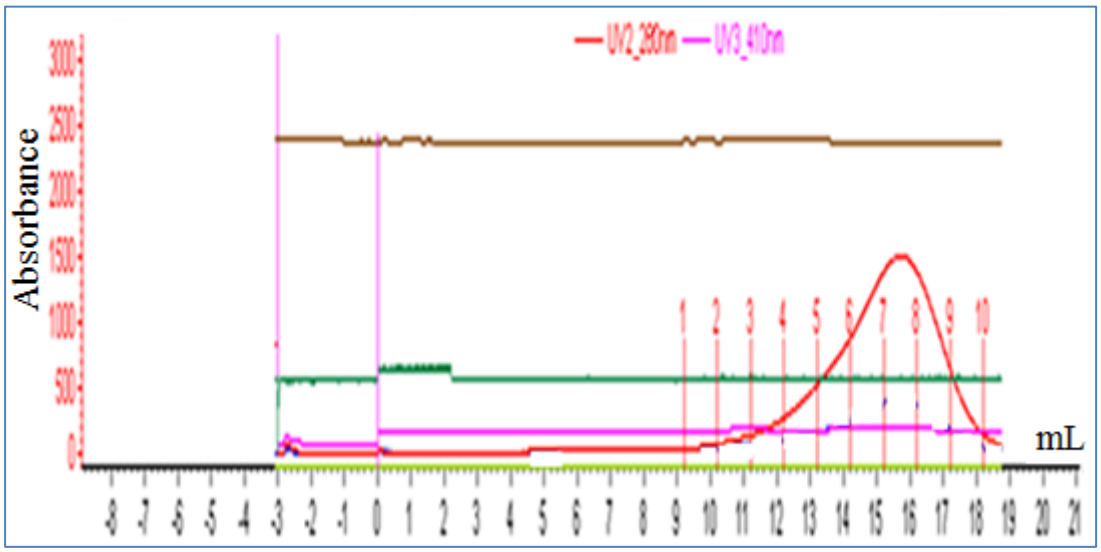

Figure 30. Anion exchange column profile of rHFn after SEC. Red and pink peaks belong to the absorbances at 280 nm and 410 nm, respectively.

The fractions at the 5, 6, 7, 8, 9 mL as seen on the profile were collected and each fraction was subjected to SDS for the proof of the purification after chromatography (Figure31).

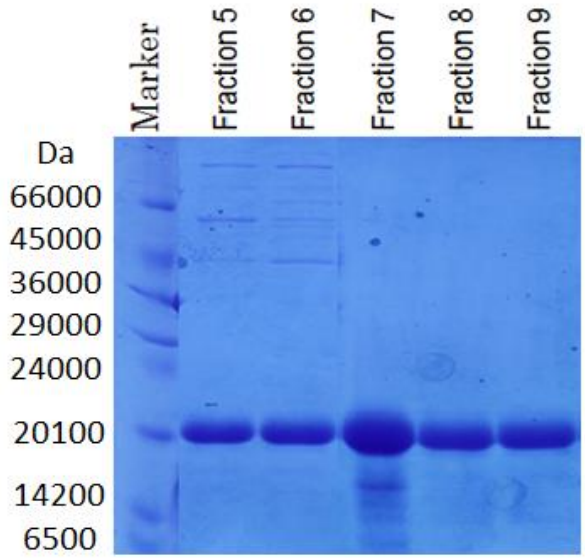

Figure 31. SDS result for the fractions after anion exchange column with a low weight marker (Sigma, M3913) with the molecular weight range between 6500 and 66000 Da.

The molecular weight of one subunit of the protein is around 20000 Da. Therefore the comigration of all the fractions at nearly the same place with the marker of 20100 Da can be seen from Figure 32. This indicates that the protein was totally purified after anion exchange column. Moreover, there is no smear before and after the lanes in the fractions.

3.2 Characterization of FeOOH Nanoparticles Synthesized in rHFn

The ferrihydrite nanoparticles were synthesized in rHFn cages without any oxidant added to the system. The nanoparticle formation occurred by air oxidation with the ferroxidase centers catalytic effect at the nucleation sites.

The synthesized ferrihydrite nanoparticles come out with colour yellow differing from brown/dark brown magnetite or maghemite nanoparticles as seen in Figure 32.

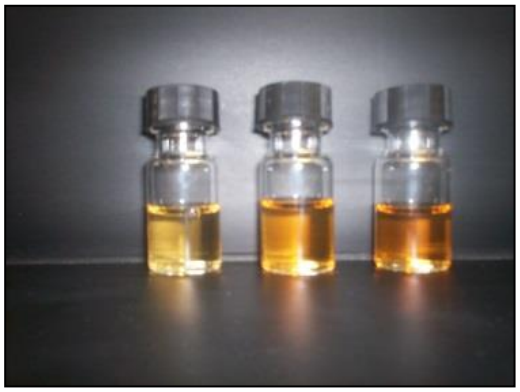

Figure 32. Ferrihydrite nanoparticles in ferritin cage with theoretical Fe loading factors of 1000 Fe, 2000 Fe and 3000 Fe per protein cage, respectively.

TEM data was collected in order to visualize the ferrihydrite (FeOOH) mineral prepared in the cavity of rHFn and to determine the core size of the nanoparticles.

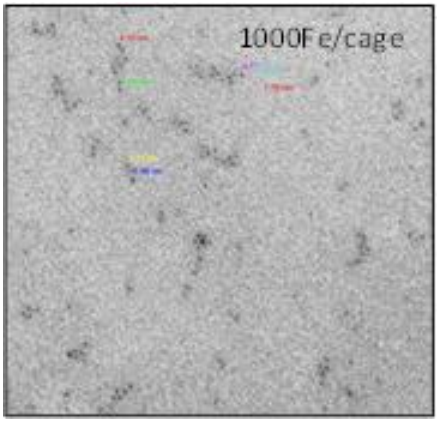

Figure 33. TEM image of ferrihydrite nanoparticles in ferritin cage with theoretical Fe loading factor of 1000 Fe with an average size of 3.78 ± 1.65 nm.

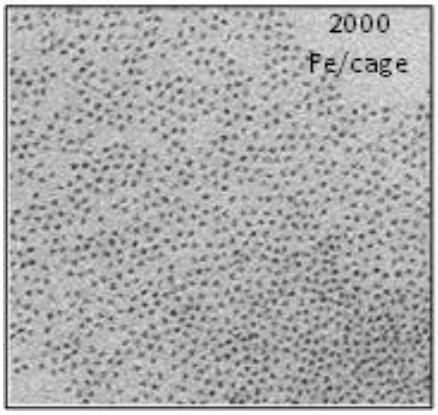

Figure 34. TEM image of ferrihydrite nanoparticles in ferritin cage with theoretical Fe loading factor of 2000 Fe with an average size of 5.30 ± 0.64 nm.

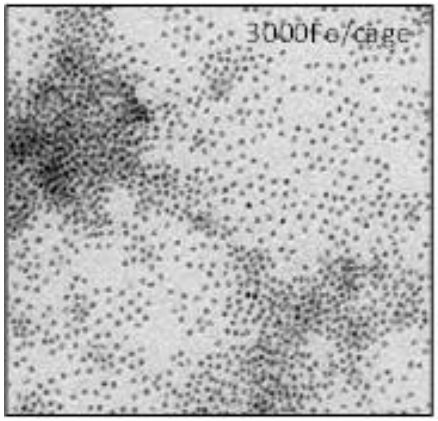

Figure 35. TEM image of ferrihydrite nanoparticles in ferritin cage with theoretical Fe loading factor of 3000 Fe with an average size of 6.68 ± 0.74 nm.

As Fe loading factor increases, the colour of the sample becomes more intense and the sizes of the nanoparticles formed in the cavity increase as seen in TEM images (Figure 33, Figure 34 and Figure 35).

Under biological conditions, the iron molecules are stored as a ferrihydrite core by ferritin, so ferrihydrite mineralization was the beginning point to be used as a ‘proof

of concept' to understand as much about the biological processes as possible, rather than merely mimic the end result.

Since the aim is to prepare a magnetic nanoparticle for targeting and for using as an MRI contrast agent, the ferrimagnetic mineral magnetite prepared is characterized in detail**.**

3.3 Characterization of Magnetoferritin Samples Synthesized in rHFn

We have used the rHFn for the synthesis of iron oxide nanoparticles, with a range of iron loadings per protein cage, and evaluated these materials as active catalysts and MRI contrast agents for a previously reported peroxidase reaction. The particle size dependent properties of catalytic activity and T_1, T_2 have also been investigated. The reaction apparatus and the images of the samples are seen in Figure 36 and Figure 37, respectively.

Figure 36. The apparatus for the protein mineralization reactions.

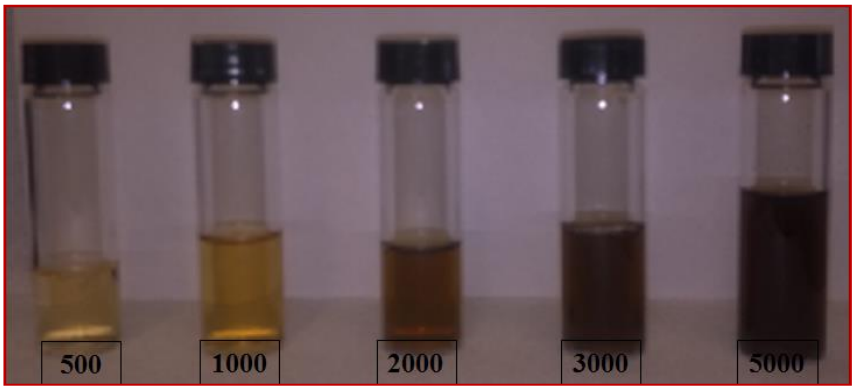

Figure 37. Magnetoferritin samples with different theoretical Fe loading factors of 500Fe, 1000Fe, 2000Fe, 3000Fe, and 5000Fe per protein cage.

rHFn samples were analyzed before and after mineralization by SEC. The collected fractions of the mineralized protein from column were again subjected to SEC in order to check the purity. Elutions from the column were monitored at both 280 nm for protein and 410 nm for the presence of iron oxide mineral. The empty protein did not show absorption at 410 nm before the mineralization, the mineralized protein showed some aggregation however collected fractions that are shown with straight line, did not have aggregated product in SEC profile (Figure 38).

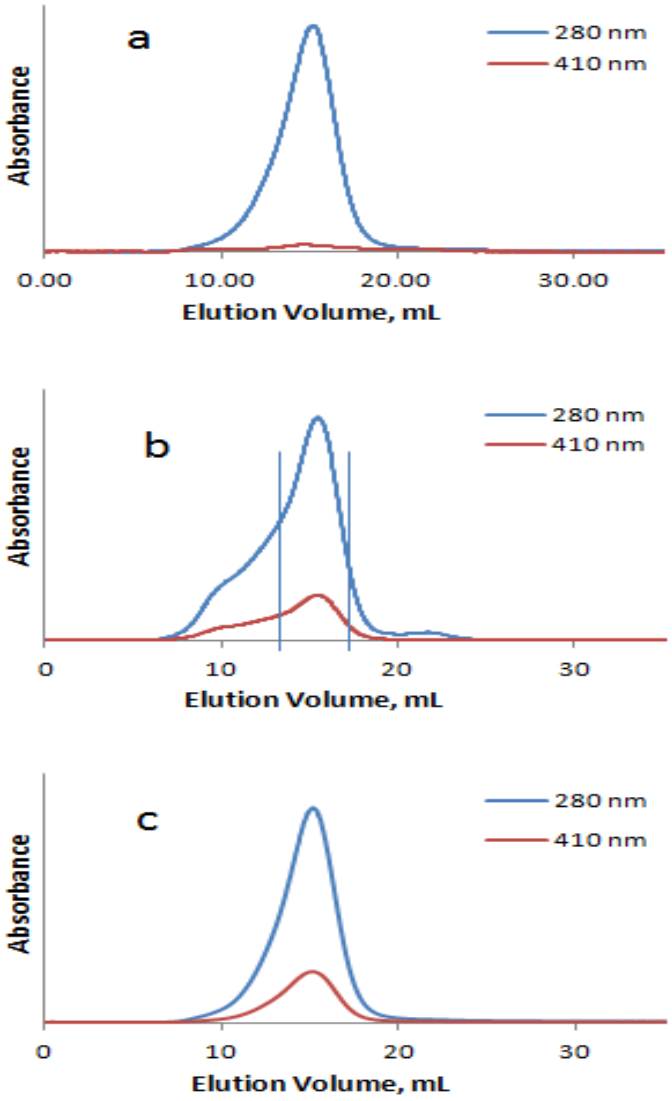

Figure 38. SEC profile of a. rHFn before mineralization reaction, b. mineralized protein with the theoretical iron loading of 1000 Fe/cage, c. collected fractions of the mineralized protein from column.

The SEC profile of the rHFn after mineralization with different loading factors showed the coelution behavior of iron oxide mineral (410 nm) and protein (280 nm). The latter was eluted at the same time (volume) as the native (unmineralized) rHFn as shown in Figure 39.

This indicates the formation of a composite material and that the protein cage remains intact after the mineralization reaction with the mineral component encapsulated within the cage.

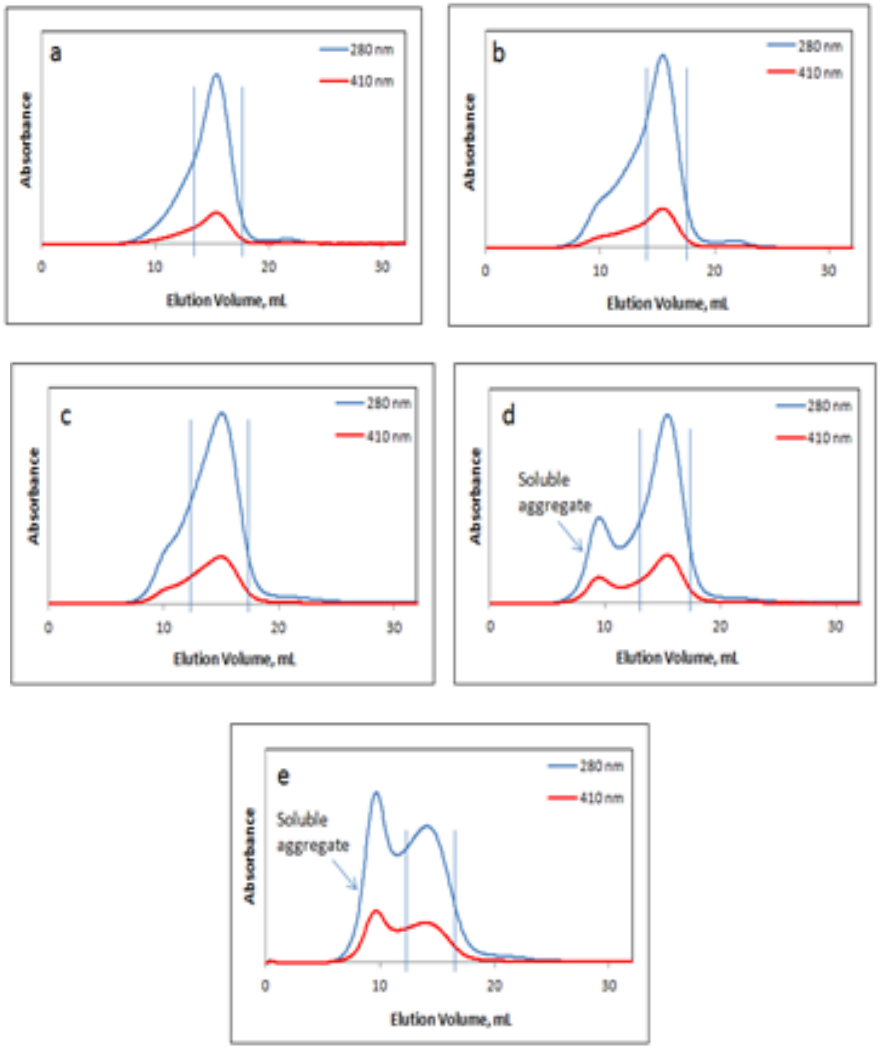

Figure 39. SEC profiles of the mineralized samples.

In the SEC profiles, the band at 280 nm corresponds with the protein and the band at 410 nm with the metallic core. Straight lines show the fractions that were collected. The profiles belong to the samples with the theoretical loadings of a. 500 Fe/cage b. 1000 Fe/cage c. 2000 Fe/cage d. 3000 Fe/cage e. 5000 Fe/cage (Figure 38).

In order to quantify the number of Fe atoms/cage the protein concentration and iron concentration were determined by Bradford Assay and Atomic Absorbtion Spectroscopy (AAS), respectively. Theoretical and experimental numbers of Fe atom per protein cage are seen in Table 13 for all mineralized samples.

Table 13. Results of the Bradford Assay and AAS measurement of magnetoferritin samples.

Theoretical Fe/cage	Experimentally found Fe/cage	Experimentally found Fe/cage
500	252	410
1000	707	798
2000	1315	1386
3000	2590	2866
5000	4406	5329

Theoretical Fe/cage here describes the input iron number per cage for the mineralization reaction and experimental Fe/cage was obtained from the AAS and Bradford Assay experiments. According to the theoretical and experimental results, measured ratios of Fe/cage do not match exactly to the theoretical number of Fe/cage. This may result from the loss of iron that might have been adsorbed on the protein cage during the synthesis or the free iron in the reaction environment, since after the addition of sodium citrate to complex the free iron, iron precipitation is always seen or this may result from the loss of protein that may be precipitated due to aggregate formation during the reaction.

Three different mineralized magnetoferritin samples, with different Fe loadings, were investigated by transmission electron microscopy (TEM) to determine the size of the iron oxide nanoparticles and to directly visualize the rHFn cage (Figure 40 and Figure 41).

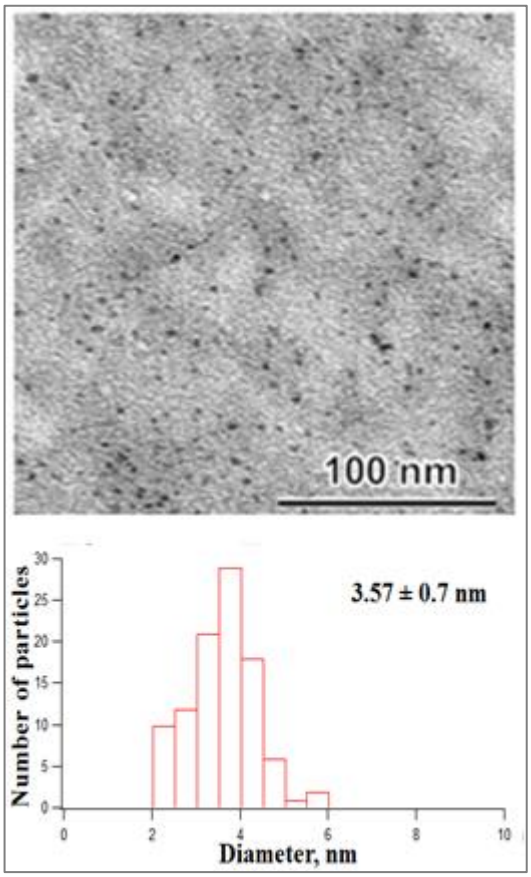

Figure 40. TEM image of mineralized iron oxide nanoparticles within rHFn for the the samples with the experimental loading factors of 410 Fe/cage.

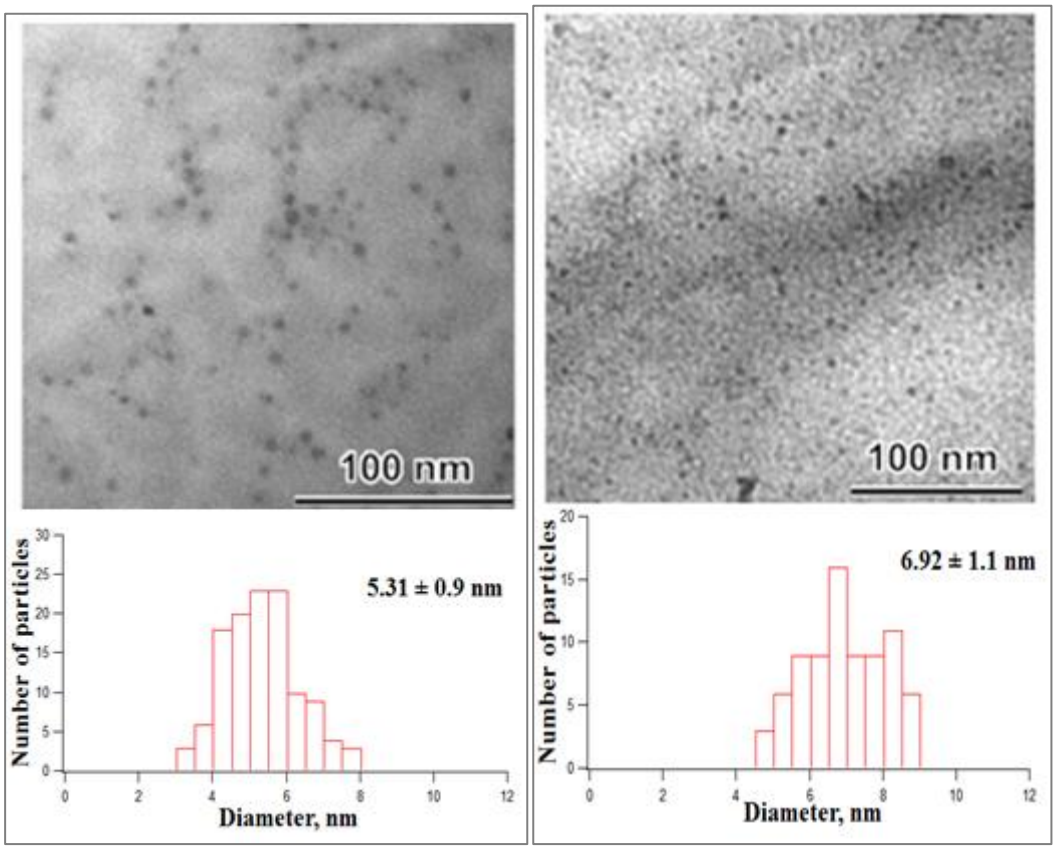

Figure 41. TEM images of mineralized iron oxide nanoparticles within rHFn for the the samples with the experimental loading factors of 2183 Fe/cage and 5551 Fe/cage, respectively.

For the the samples with the experimental loading factors of 410 Fe/cage, 2183 Fe/cage and 5551 Fe/cage, size distribution histograms of the particles were obtained from the TEM images by measuring the diameters of more than 100 particles. The values on the histograms are given as mean size ± standard deviation.

As shown in TEM images, the sizes of the particles increase with increasing Fe stoichiometry in the reaction and correlate well with the measured Fe atom/cage loadings. The average size of the particles were measured as 3.6 nm, 5.3 nm and 6.9 nm for experimental loading factors of 410 Fe/cage, 2183 Fe/cage and 5551 Fe/cage, respectively.

The particle sizes were also calculated by using the results of iron and protein analysis (AAS and Bradford measurements) of the mineralized samples, that is called as ‘calculated size’.

For the calculations of experimental sizes of magnetoferritin nanoparticles, the number of iron atoms existing in a unit cell was found from the crystal structure model of Linnaeite (Co_3S_4), since that is given as prototype of magnetite (Fe_3O_4) structure [119]. In the structure, there are 32 oxygen atoms and 24 iron atoms (Figure 42).

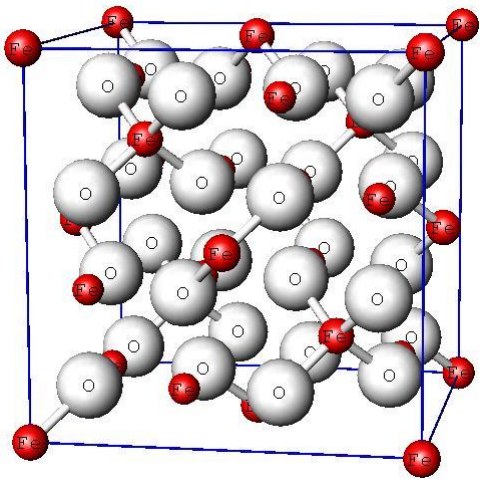

Figure 42. Linnaeite (Co_3S_4) crystal structure (prototype of magnetite (Fe_3O_4)).

The calculations are given in Table 14 for the sample with the loading of 410 Fe/cage.

Table 14. The calculations for the experimental sizes of magnetoferritin sample with the loading of 410 Fe/cage.

	Magnetite (Fe_3O_4)
For a unitcell, a;	0,8397 nm
Volume of unitcell, a3;	0,592 nm^3
For a unitcell, Z;	8
Number of Fe atoms/unit cell	8 x 3 =24

Magnetoferritin sample (410 Fe/cage)	**Experimentally obtained values**
Mole of protein:	$0.24x10^{-9}$
Mole of Fe:	$9.69x10^{-8}$
Total # of Fe atoms:	$9.69x10^{-8} x N_A = 5.83 x 10^{16}$
Total # of protein:	$0.24x10^{-9} x N_A = 1.44 x 10^{14}$
Number of Fe atom/protein:	$5.83x10^{16}/1.44x10^{14} = 403.5$
Number of Fe atom/protein:	24x(Number of unit cell)
Number of unit cell:	16,8 = Volume of particle/0.592
Volume of particle:	9.95 nm^3 = 4/3 x 3.14 x (r)3
Radius (r):	1.33 nm
Diameter:	2.67 nm

In Table 14;

a is the dimension of unit cell. (0,8397 nm).

Z is the repeating siplest formula for one unit cell (8).

Number of iron atoms in a unit cell is 24 (Fe_3O_4 x 8 = $Fe_{24}O_{32}$)

N_A is the Avagadro's number (6.02×10^{23}).

Calculated sizes are given in Figure 43 together with the TEM sizes for these three samples.

Number of Fe/cage	TEM size, nm	Calculated size, nm
410	3.57 ± 0.73	2.67 ± 0.16
2183	5.31 ± 0.92	4.68 ± 0.31
5551	6.92 ± 1.12	6.39 ± 0.49

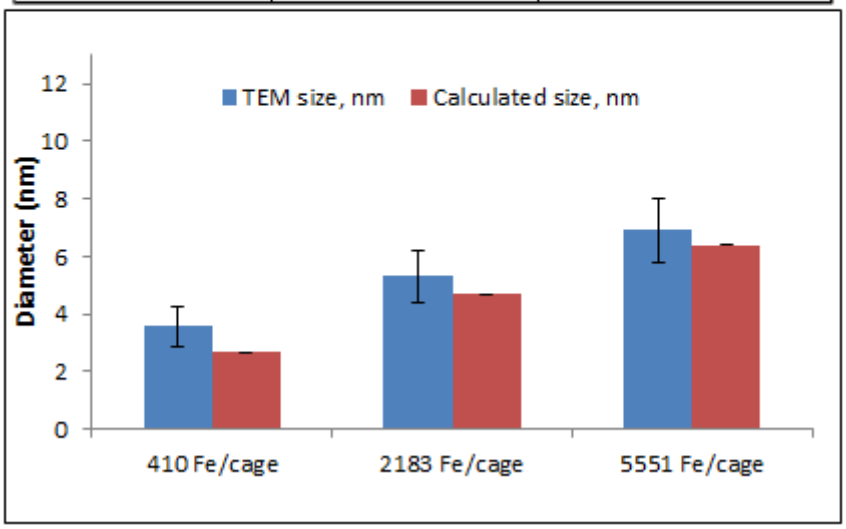

Figure 43. The plots for sizes obtained from TEM images and experimental calculations.

The standart deviations of the calculated sizes include the deviations from the results of Bradford assay and AAS measurements. The standart deviation from a (dimension of unit cell) was not taken into consideration. The results give good correlation between the sizes and this shows that iron atoms were distributed homogenously throughout the protein cages during the synthesis. The differences in size (diameter, nm) from the TEM measurements may result from the possibility of biased measurements and aggregation on TEM grid during sample preparation.

3.4 Characterization of Magnetoferritin Samples Synthesized in HoSF

HoSF protein cages were demineralized by the reductive dialysis method and iron oxide nanoparticles were synthesized in the 8 nm sized cavity of the protein under elevated pH and temperature (pH 8.5, 65 °C) to direct the ferrimagnetic phase Fe_3O_4. Protein samples were purified and analyzed before and after mineralization by SEC

as described above. From the AAS and Bradford analysis for this sample, loading factor was found to be 1855 Fe/cage. Elutions from the Sephadex column were collected and monitored at both 280 nm and 410 nm for protein and iron oxide nanoparticles, respectively. Analysis of both apoferritin and mineralized ferritin by SEC exhibited identical elution times that indicate the intact protein cage after mineralization (Figure 44).

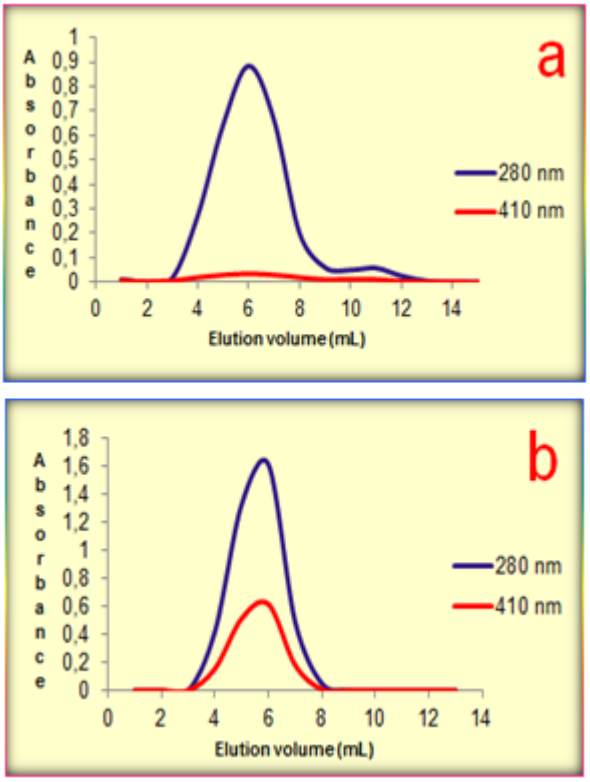

Figure 44. SEC profile of a. HoSF before mineralization reaction, b. Mineralized ferritin.

Mineralized sample was negatively stained with 1% uranyl acetate solution and investigated by TEM to determine the size of the iron oxide nanoparticles and to show protein shells around each particle.

The average size of the particles was measured as 4.52 ± 1.2 nm and the image shows the expected spherical cage like structure (Figure 45).

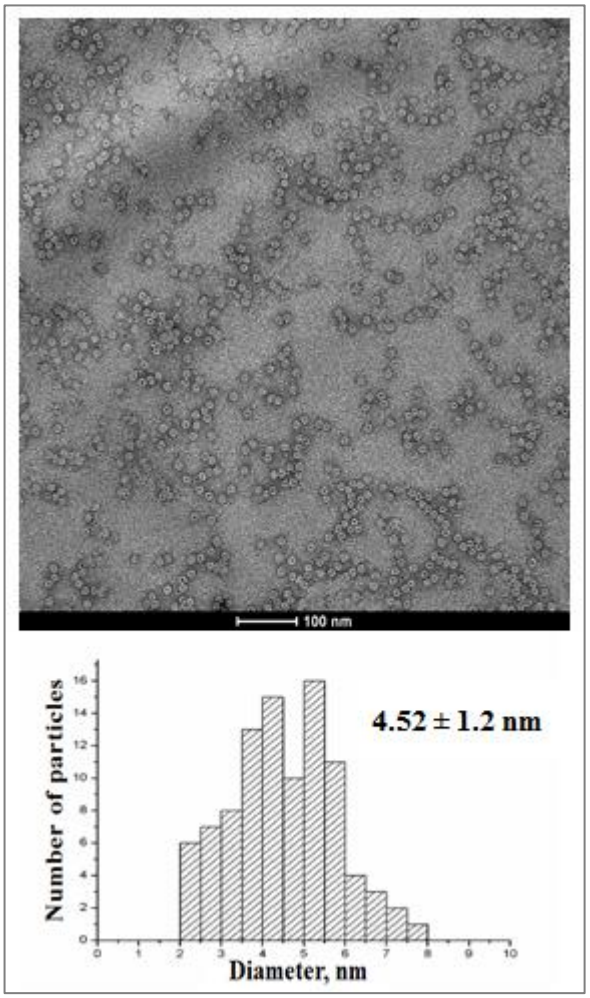

Figure 45. TEM image and the size distribution histogram of magnetoferritin sample. Size distribution histograms of the particles analyzed from the TEM image obtained by measuring the diameters of more than 100 particles. The value on the histogram is given as mean ± standard deviation.

3.5 Surface Modification of Protein Exterior Surface

Ferritin provide a constrained reaction environment for the synthesis of the iron oxide based nanoparticles as mentioned before and the surface modification in order to incorporate a radioactive label on the protein cage exterior to be used as magnetic carriers for radioactive isotopes.

Here, for the surface modification experiments, magnetoferritin samples synthesized from HoSF protein were purified and analyzed before and after mineralization by SEC as described above were used. Then surface was modified by immobilization of histidine molecules through glutaraldehyde crosslinker as seen in Figure 46. Thus, a suitable platform was obtained for the attachment of the rhenium complex, since it is stated that $[M(CO)_3(H_2O)_3]^+$ (M = Tc, Re) does not form stable complexes with aliphatic amines and thioethers, but prefers the ‘‘soft’’ sp^2 nitrogen of aromatic amines [120].

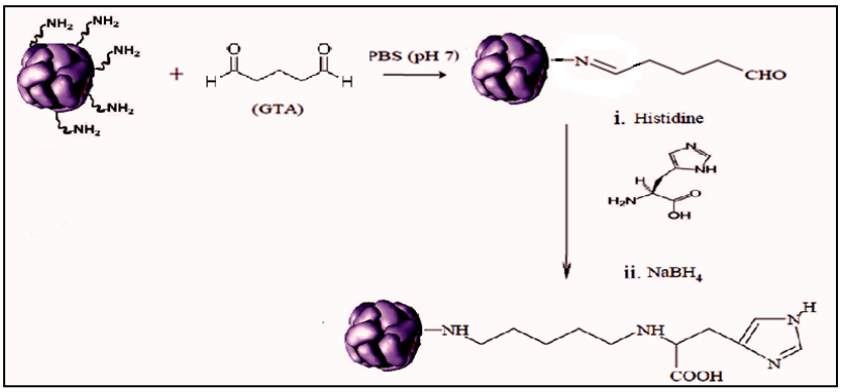

Figure 46. Procedure for histidine immobilization on ferritin surface [71].

3.5.1 Spectrophotometric Determination of Histidine on the Protein Surface

This method used is a specific spectrophotometric method for the determination of histidine from the other amino acids present in the medium.

The amino group of sulfanilic acid reacts with sodium nitrite to give a diazonium salt of sulfanilic acid in the presence of hydrochloric acid. The formation of a yellow colour was occured upon the diazotization reaction between histidine and diazotized sulfanilic acid. The yellow colour product was stable for around 10 min. and the absorbances were measured at the sixth min. at 405 nm for all the reaction products [121].

The UV-VIS spectra of the histidine binded magnetoferritin and magnetoferritin samples are given in Figure 47. The magnetoferritin sample was used as control here. The band at 405 nm is seen apparently thus the method was especially useful for the qualitative proof of histidine exposed on the protein surface.

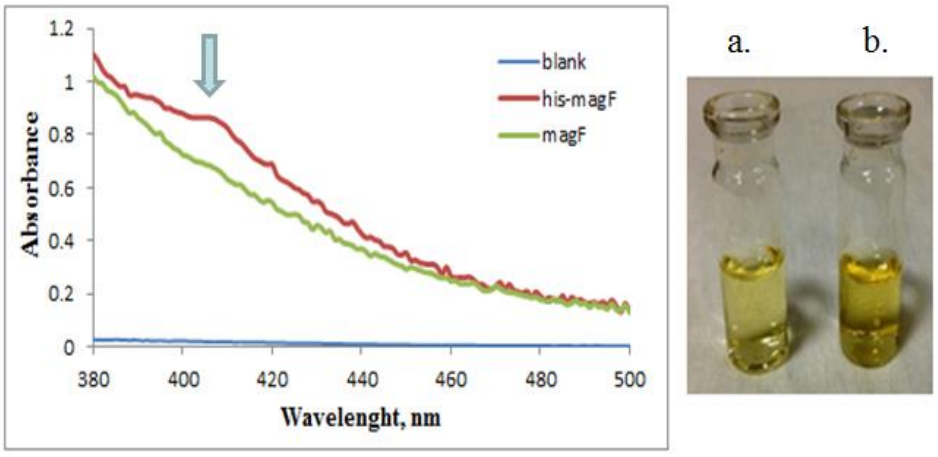

Figure 47. UV-Vis spectrum of magnetoferritin and histidine immobilized magnetoferritin. a. Magnetoferritin sample, b. His-magnetoferritin sample.

3.6 Characterization of Rhenium Complex by HPLC-ICP-MS

A non-radioactive rhenium isotope was used for the preparation of rhenium carbonyl complex, $[Re(CO)_3(H_2O)_3]^+$, since studying with radioactive elements was not suitable in our laboratories.

In all studies, non-radioactive rhenium salt ($NaReO_4$) was used. Perrhenate anion (ReO_4^-) which was mixed with phosphoric acid was reacted with CO gas in a reductive environment. Amineborane ($NH_3.BH_3$) was used as a reducing agent.

HPLC system equipped with S5 SAX anion exchange column is connected to the nebulizer of ICP-MS for characterizing the formed rhenium species. The mobile phase was 5.0 mM sodium citrate in 10.0% MeOH at pH 4.5.

Chromatograms of standard ReO_4^- and the blank solution which was the mixture of $ReO4^-$, BH_3NH_3 and H_3PO_4 used for synthesis of rhenium carbonyl complex are given in Figure 48.

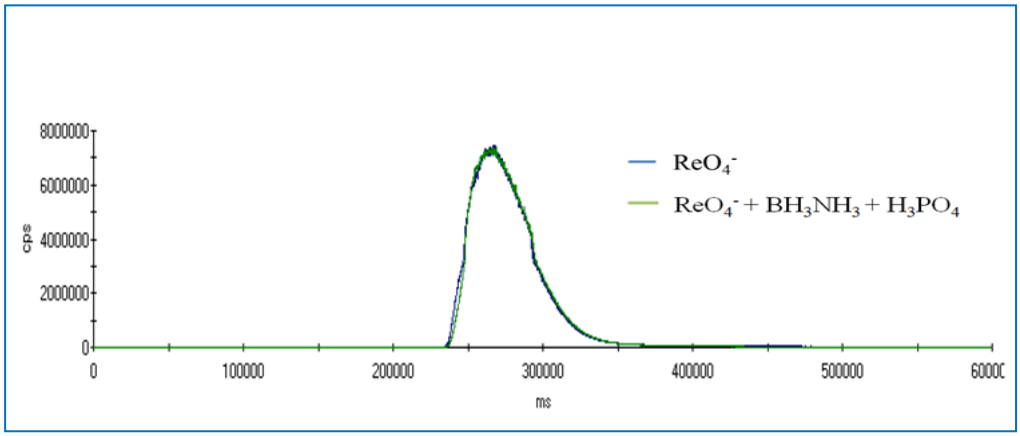

Figure 48. HPLC-ICP-MS chromatograms of standard solution of ReO_4^- and the solution including (ReO_4^- , BH_3NH_3 and H_3PO_4) except $CO_{(g)}$.

As can be seen from the Figure 48, the chromatograms of ReO_4^- standard solution and the blank solution are overlapping completely. This result indicates that BH_3NH_3 and H_3PO_4 do not have any effect on the chromatogram.

Carboxylation reaction of rhenium takes place in this acidic medium in the presence of carbon monoxide gas. Once the reaction was finished, the solution taken from the reaction vessel was injected to HPLC-ICP-MS system for characterization.

The chromatogram is depicted in Figure 49, together with that of the standard solution of ReO_4^- and the blank solution.

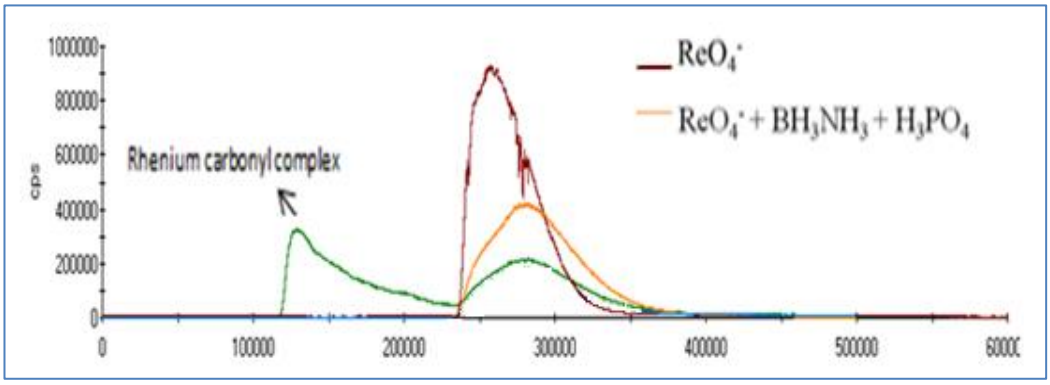

Figure 49. HPLC-ICP-MS chromatograms of reaction medium after the synthesis of rhenium complex, standard solution of ReO_4^- and the solution including ($ReO4^-$, BH_3NH_3 and H_3PO_4) except $CO_{(g)}$.

As shown in the Figure 49**,** there are mainly two peaks in the chromatogram (green) of the reaction medium after the synthesis of rhenium complex. An anion exchange resin was used in HPLC column, therefore, it was expected that the positively charged species would appear early during elution. Therefore the former was assigned to the rhenium carbonyl complex due to its positive charge. Whereas the latter which overlaps with the peak of standard perrhenate solution is connected to the unreacted perranate ion remaining in the solution.

The optimization studies were carried out by changing the amounts of $BH_3.NH_3$ and H_3PO_4 and the reaction time. The concentration of ReO_4^- was kept constant at $4.4x10^{-5}$ M. Time duration for CO gas that was passed through the vial was tried over 10 min and 20 min. As mentioned before, after the completion of complex formation, the solution taken from the reaction vessel was injected to HPLC-ICP-MS system for characterization the complex formation yield (efficiency) was calculated by taking the area ratio of each peak with respect to the total chromatogram.

3.6.1 Effect of $BH_3.NH_3$ Amount on Complex Formation Efficiency

The amount of $BH_3.NH_3$ was changed in the range of 5 mg and 15 mg. The volume of H_3PO_4 was kept at 40 µL and CO was passed through the vial for 10 min. The chromatograms for the complex after the synthesis were taken as shown in Figure 50.

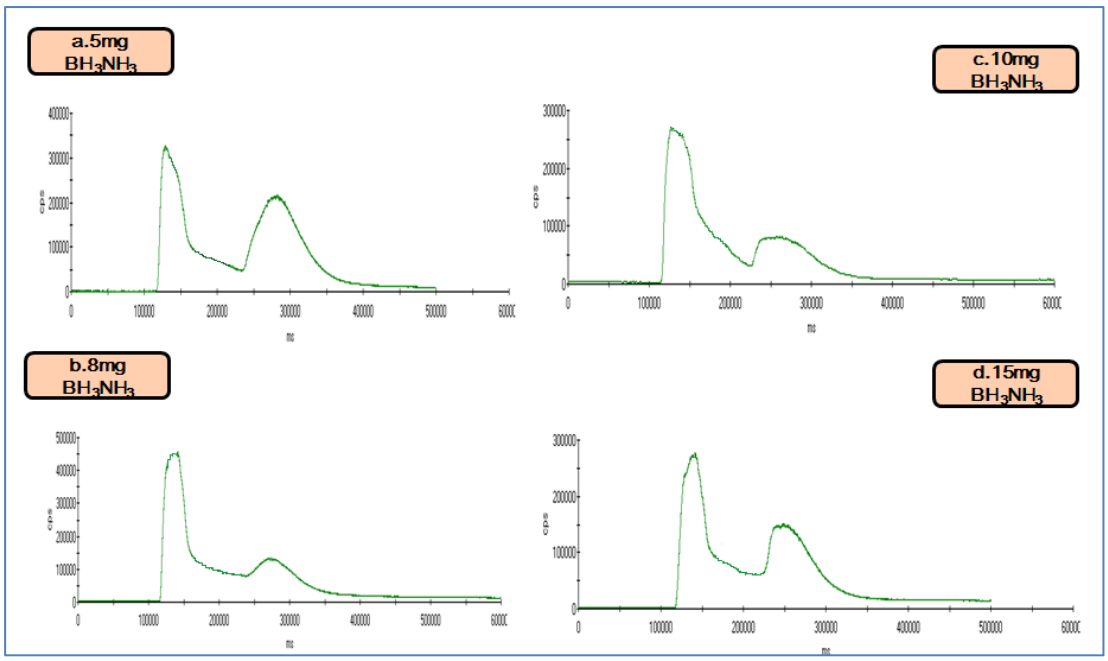

Figure 50. HPLC-ICP-MS chromatograms of reaction medium after the synthesis of rhenium complex.

Since the complex formation efficiency was calculated by taking the area ratio of each peak with respect to the total chromatogram, the efficiencies were found for each experiment as; **a.** 31%, **b.** 39.1%, **c.** 64%, **d.** 32.1.

The maximum efficiency for the optimization experiments was 64% which was obtained when 10 mg $BH_3.NH_3$ was used.

3.6.2 Effect of Acidity on Complex Formation Efficiency

The other important parameter is the acidity of the medium. The concentration of H_3PO_4 in the reaction medium should be adjusted properly to reduce rhenium completely. The volume of acid were 60 µL, 40 µL and 20 µL. The amount of $BH_3.NH_3$ was kept at 10 mg and CO was passed through the vial over 10 min. The chromatograms for the reaction medium after the synthesis are presented in Figure 51.

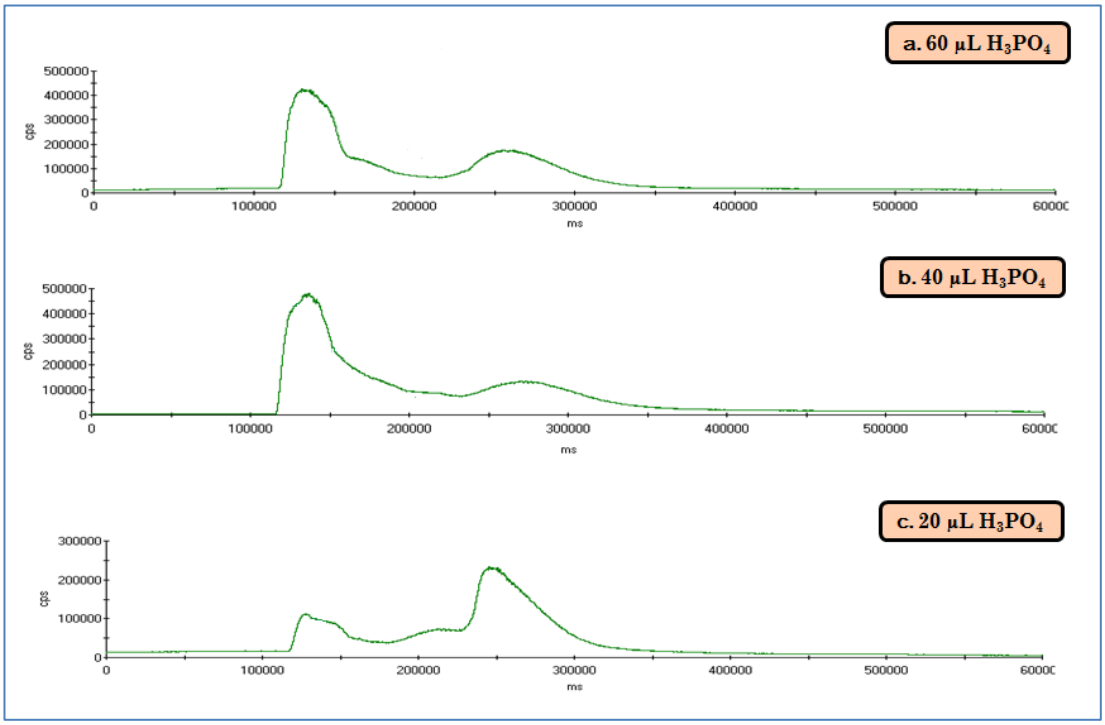

Figure 51. HPLC-ICP-MS chromatograms of reaction medium after the synthesis of rhenium complex.

The complex formation efficiencies were found for each experiment as **a.** 55%, **b.** 62%, **c.** 30%. The maximum efficiency for the optimization experiments was 62% which was obtained when 40 µL H_3PO_4 was used.

3.6.3 Effect of CO(g) Flushing Time on Complex Formation Efficiency

CO(g) flushing time is the last optimization parameter tried to improve the complex formation yield. In the presence of 10mg BH_3NH_3, and 40 μL H_3PO_4, CO flushing time was varied as 10 min. and 20 min. Chromatograms for the 10 min. and 20 min. reaction is shown in Figure 52 and Figure 53, respectively.

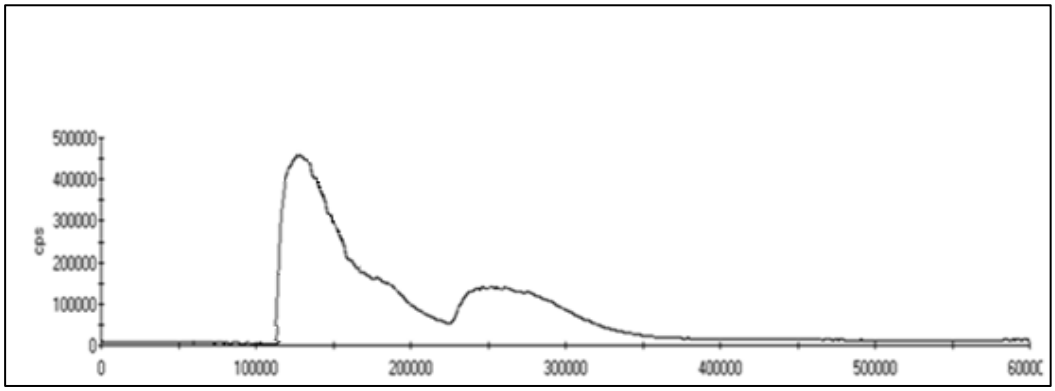

Figure 52. HPLC-ICP-MS chromatogram of reaction medium after the synthesis of rhenium complex.

CO gas was passed over 10 min. and the efficiency was found as 65%.

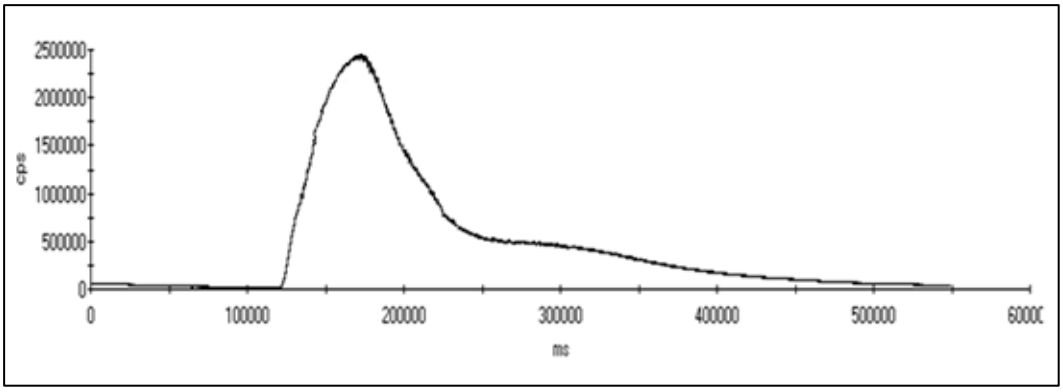

Figure 53. HPLC-ICP-MS chromatogram of reaction medium after the synthesis of rhenium complex.

CO gas was passed over 20 min. and the efficiency was found as 70%.

Complex formation efficiency was getting increased slightly when CO (g) flushing time was 20 min. However, this result was not consistent, in most of the other trials; 20 min flushing time did not show a considerable change in the efficiency (Figure 53).

As a summary, it was observed that around 65% of the rhenium was reacted to give rhenium carbonyl complex in most of the complex formation experiments.Therefore the optimum condition for the maximum complex formation efficiency was set as 10mg of $BH_3.NH_3$, 40 µL H_3PO_4 and the CO flushing time of 10 min. The chromatogram of the reaction medium after the synthesis of the rhenium carbonyl complex at the optimized condition is given in Figure 54.

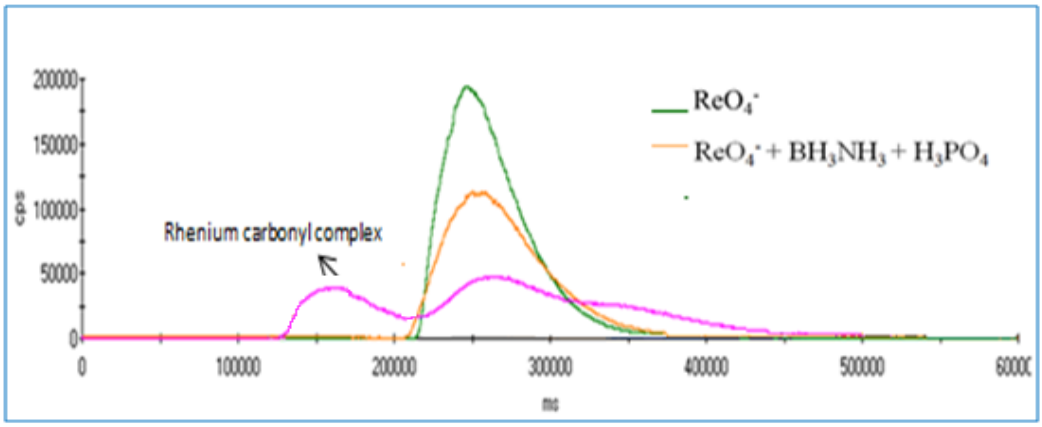

Figure 54. HPLC-ICP-MS chromatograms of reaction medium after the synthesis of rhenium complex, standard solution of ReO_4^- and the solution including ($ReO4^-$, BH_3NH_3 and H_3PO_4) except $CO_{(g)}$.

Since the reaction yield was 65 % in the synthesis of the rhenium carbonyl complex, an anion exchange resin column was used in order to separate the renium carbonyl complex from other reaction products or left overs.

The success of purification was evaluated by injecting the eluate to an HPLC-ICP-MS system equipped with the same type anion exchange column.

The same eluent (5.0 mM sodium citrate in 10.0% MeOH at pH 4.5) was used both in the purification and in the HPLC columns. The chromatogram of the eluent from the purification column, the blue one, is presented in Figure 55.

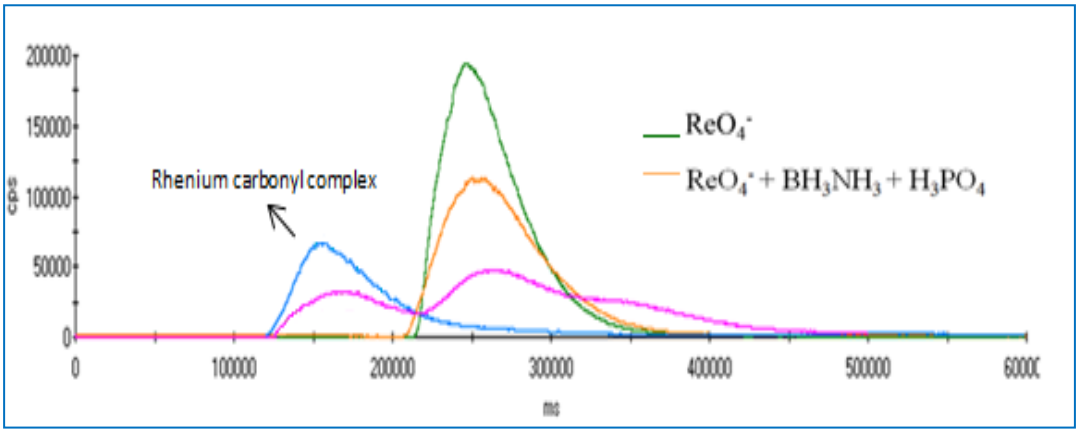

Figure 55. HPLC-ICP-MS chromatograms of rhenium complex before (pink signal) and after (blue signal) purification through anion exchange column, standard solution of ReO_4^- and the solution including ($ReO4^-$, BH_3NH_3 and H_3PO_4) except $CO_{(g)}$.

In order to improve the separation efficiency, the pH of the mobile phase was rendered more acidic. The chromatogram of the eluate having a pH of 3.0 is given in Figure 56.

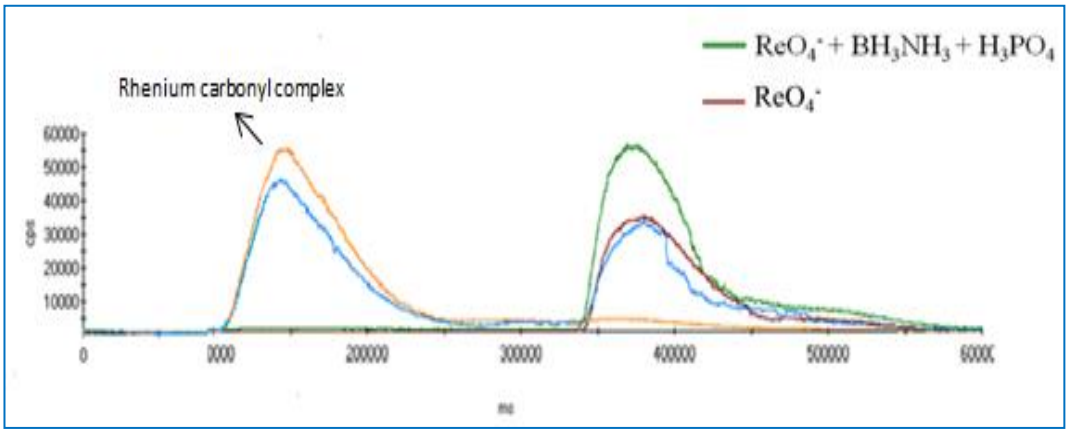

Figure 56. HPLC-ICP-MS chromatograms of rhenium complex before (blue signal) and after (yellow signal) using anion exchange resin, standard solution of ReO_4^- and the solution including ($ReO4^-$, BH_3NH_3 and H_3PO_4) except $CO_{(g)}$.

When (5.0 mM sodium citrate in 10.0% MeOH at pH 3.0) was used as the mobile phase, a better separation of the peaks were obtained.

3.7 Labeling of Histidine Immobilized Nanoparticles with Rhenium Complex

It is assumed that there are 72 lysine groups exposed to the solution on the exterior surface of the protein. For the immobilization of histidine to magnetoferritin surface via glutaraldehyde crosslinker, 10 fold excess amounts of glutaraldehyde and histidine compared to the total number of surface lysine groups were used for the surface modification experiments. The rhenium complex was bound to the protein surface through histidine groups as seen in Figure 55. After the synthesis, the unbound reactants were removed by exhaustive dialysis. The synthesized final product was illustrated in Figure 57.

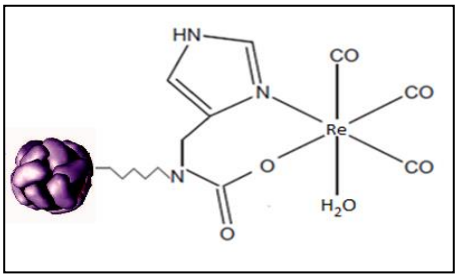

Figure 57. The Re-labeled magnetoferritin protein.

3.7.1 Effect of Histidine Immobilization on the Binding Efficiency of Re Carbonyl Complex

In order to see the effect of histidine modification for appending the renium carbonyl complex on the protein surface a blank test was carried out.

Histidine modified and unmodified magnetoferritin particles (1855 Fe/cage) were labeled with rhenium complex and the labeling efficiencies in both case were compared. For that purpose, rhenium labeled samples were subjected to size separation by means of G-25 Sephadex column and 1 mL fractions were collected for UV-Vis and ICP-MS measurements to determine the protein and Re concentrations respectively. The distrubition of rhenium and protein amounts in the collected fractions are shown in Figure 58-a and Figure 58-b.

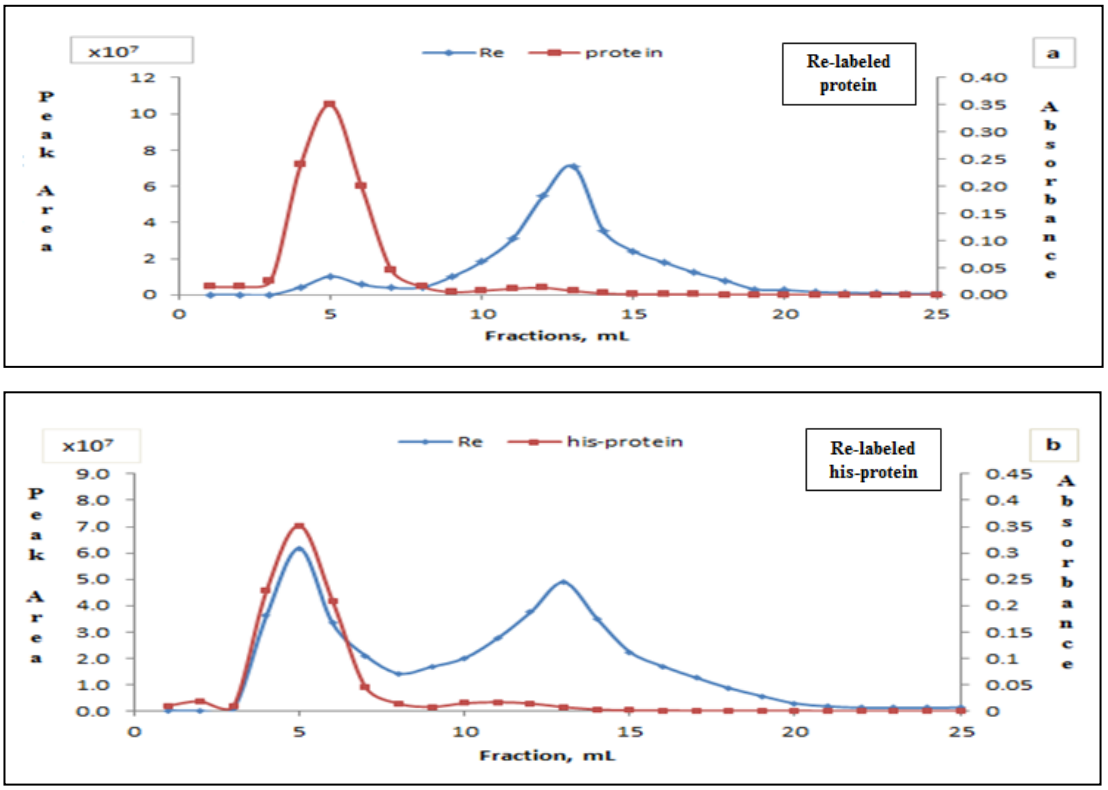

Figure 58. SEC profile of a. Magnetoferritin (1855 Fe/cage) b.Histidine immobilized magnetoferritin.

As can be seen from Figure 58, rhenium carbonyl complex appears after the column is washed with about 9 mL of eluent or after the collection of eight fractions due to its small size compared to that of protein. It comes early only if it is attached to the protein surface. In Figure 58-a, it was thought that rhenium complex was binded to protein via naturally existed amine groups (lysine) on the surface.

However, according to the Re amount binded to the proteins, it was found that Re complex was binded to histidine immobilized magnetoferritin ~ 6 fold more than magnetoferritin. Protein and Re concentrations in the protein containing fractions are given in Table 15.

Table 15. Protein and Re concentrations in the protein containing fractions.

Samples	ICP Peak Area	Re Conc. (ppb)	Protein Conc. (mg/mL)	Re (ppb)/protein (mg/mL)
his-Ferritin	180068130	18.30	0.48	38.36
Ferritin	24207559	2.72	0.43	6.36

3.7.2 Stability Tests by SEC

To test the stability of labeled protein, the protein was purified by SEC using G-25 Sephadex column after 72 h to remove the free Re complex that might have broken away from the protein and 1 mL of fractions were collected for UV-Vis and ICP-MS measurements to determine the protein and Re concentrations (Figure 59).

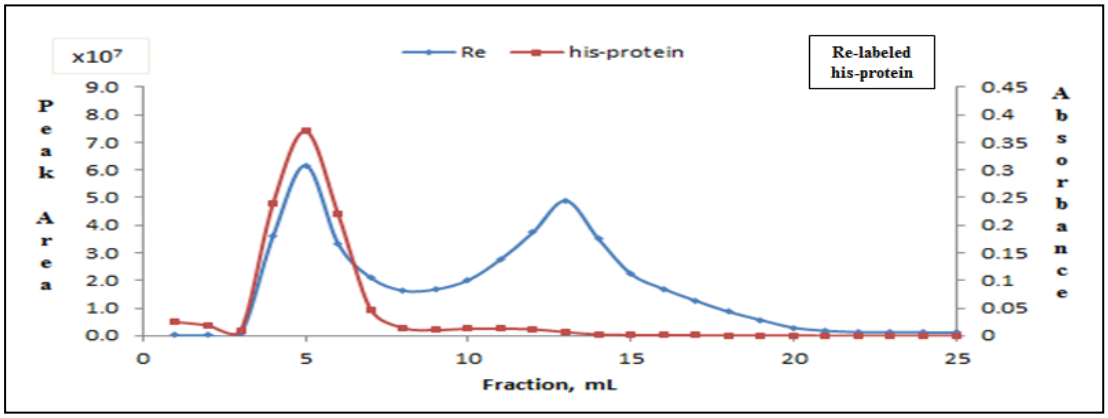

Figure 59. SEC profile of protein (1855 Fe/cage) 72 h after labeling process.

It was found that %92 of rhenium complex was still binded on the protein surface and the protein cage remains still intact 72 h after labeling process. Protein and Re concentrations in the protein containing fractions are given in Table 16.

Table 16. Protein and Re concentrations in the protein containing fractions after 72 h.

Samples	ICP Peak Area	Re Conc. (ppb)	Protein Conc. (mg/mL)	Re (ppb)/protein (mg/mL)
his-Ferritin	180068130	18.30	0.48	38.36
his-Ferritin (after 3 days)	153058000	15.61	0.44	35.56

3.7.3 Serum Stability Test

The stability of the prepared biomaterial is of importance for its biocompatibility, thus it was tested in serum and PBS buffer (0.1 M NaCl, pH 7.0) by dialysis of the Re-labeled proteins for 72h. The change in Re concentration in proteins versus time is given in Figure 60.

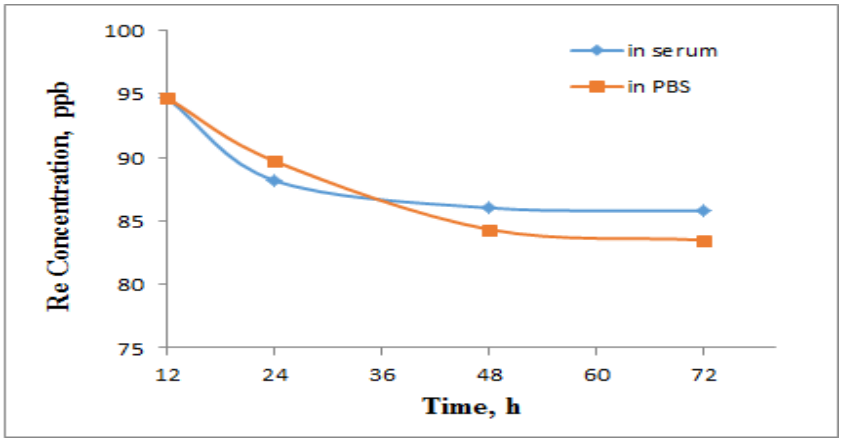

Figure 60. Re concentration in serum and PBS buffer versus time.

After 24h dialysis, it was seen from the graph that 93% ± 1.6 of the Re was still binded to protein that was suspended in serum and this value is 95% ± 1.8 for the protein in PBS.

The amount of rhenium binded to protein was then decrease slowly during 48h dialysis, this indicates that most of the Re that was detached from the protein surface occured in 24h.

After 72h dialysis, the amounts of Re still binded to protein goes to 90.6% ± 2.0 and 88% ± 1.8 for serum and PBS buffer respectively. It is seen that this results are so consistent with the SEC results (Figure 59).

3.7.4 Native Gel Electrophoresis

The stability of native ferritin, histidine immobilized magnetoferritin and Re-labeled magnetoferritin samples were electrophoretically analyzed by using polycrylamide gel (PAGE), under native (nondenaturing) conditions. The comigration of both (lanes 2, 3 and 4) indicates firstly that the protein remained intact after iron oxide nanoparticle loading and histidine and rhenium bound to the magnetoferritin surface (Figure 61).

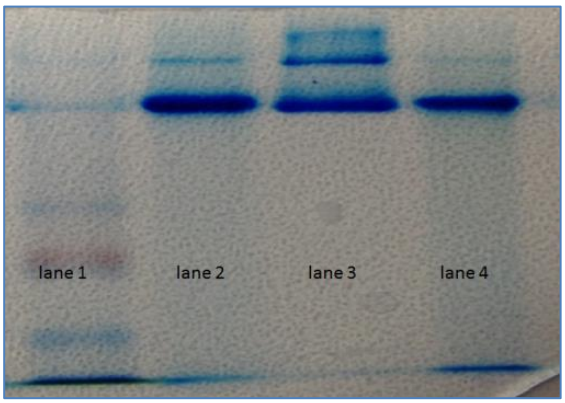

Figure 61. Native polyacrylamide gel stained electrophoresis (Coomassie Brilliant Blue R250). Lane 1 is 180 KDa markers, lane 2 is Re binded magnetoferritin, lane 3 is histidine mobilized magnetoferritin and lane 4 is native ferritin.

3.8 Biological Tests for Prepared Biomaterial

3.8.1 XTT Cytotoxicity Assay of Re-labeled Magnetoferritin

The cytotoxicity of the apoferritin, magnetoferritin, rhenium standards, rhenium complex and Re-labeled magnetoferritin samples was tested on both MDA-MB-231 and MCF-10A cells for 24, 48 and 72h by XTT assay with different concentrations ranging from 0.1-2 mg/mL for protein samples and 10-50 ppb for rhenium species. The cells not treated with any rhenium species and protein samples were used as control and named as ‘untreated’ in the graphs as seen in Figure 62. The percentage of cell viability in the control group was designated as 100%.

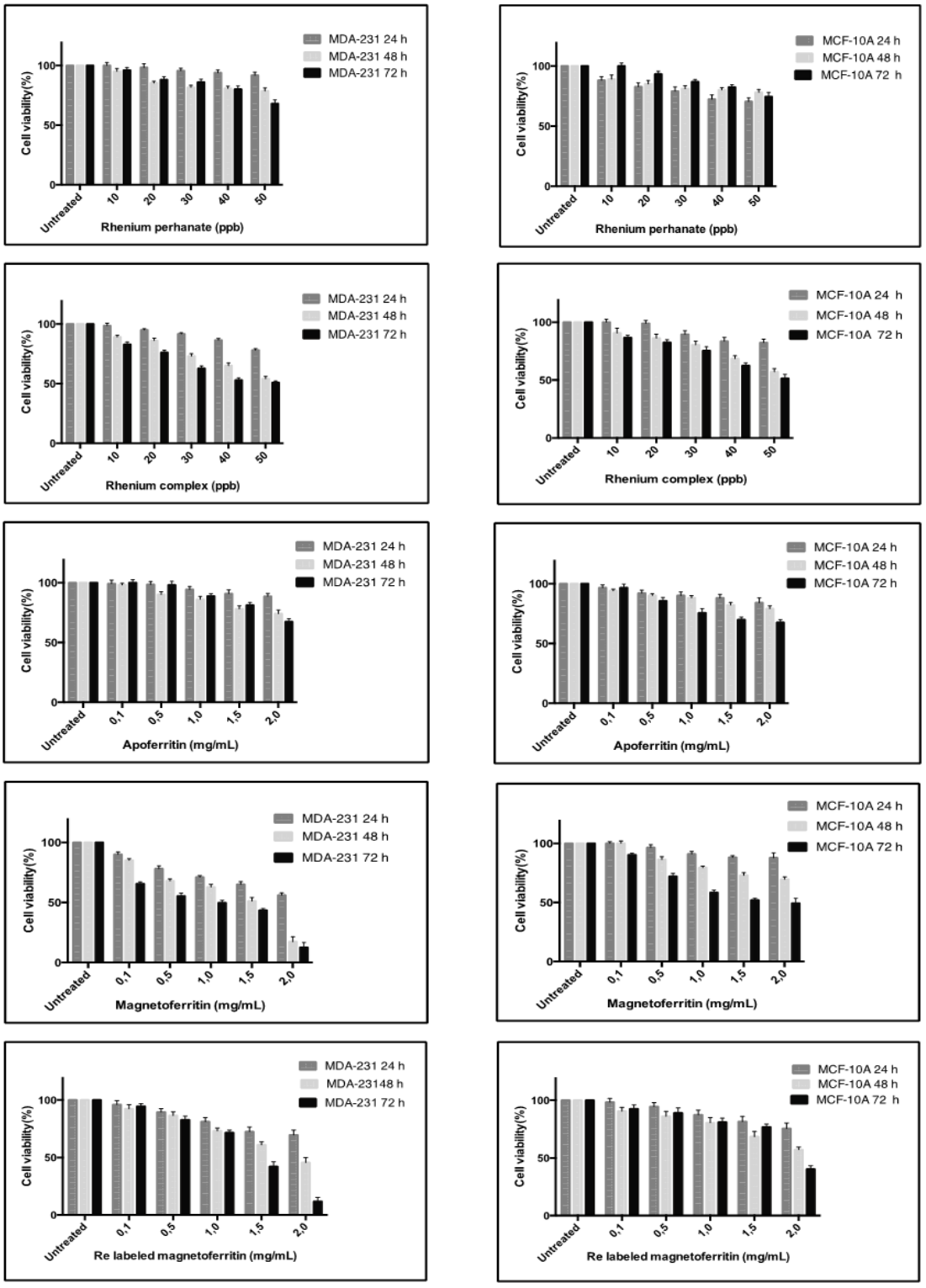

Figure 62. XTT assay results for MDA-MB-231 and MCF-10A cell lines

XTT assay results for MDA-MB-231 and MCF-10A cell lines were obtained following 24, 48, 72h exposure to the nanoparticles and rhenium species; these are apoferritin, magnetoferritin, rhenium standarts, rhenium complex and Re-labeled magnetoferritin samples. Error bars represent the standard deviation of the absorbance at 415 nm (Figure 62).

The viability of the cells for rhenium standarts exhibited no significant cytotoxicity upon treatments up to 72h. Rhenium complex showed a dose-dependent cytotoxicity within the concentration range and time tested, the cell viability reached to nearly 50% when the concentration reached 50ppb (Figure 62).

The biocompatibility is still protected for apoferritin samples in both MDA-MB-231 and MCF-10A cells as the concentration and time duration exposed to the cells increased, since more than 80% of cells still survived after treatment with 2 mg/mL for 72h (Figure 62). Thus, encapsulation of nanoparticles within a non-toxic apoferritin protein cage holds promise for cancer therapy with a reduced toxicity.

It was wondered whether Re-labeled magnetoferritin had any distinct effect on the cell viability compared with the magnetoferritin protein nanoparticles. Re-labeled magnetoferritin demonstrate a comparable cytotoxic profile with that of magnetoferritin nanoparticles. The cell viability decreased to less than 50% when the protein concentration exceeded 1 mg/mL at 72h for especially cancerous cell lines (MDA-MB-231) and the cytotoxicity in healthy cell lines are lower than cancerous cell lines over the whole incubation time for both protein samples.

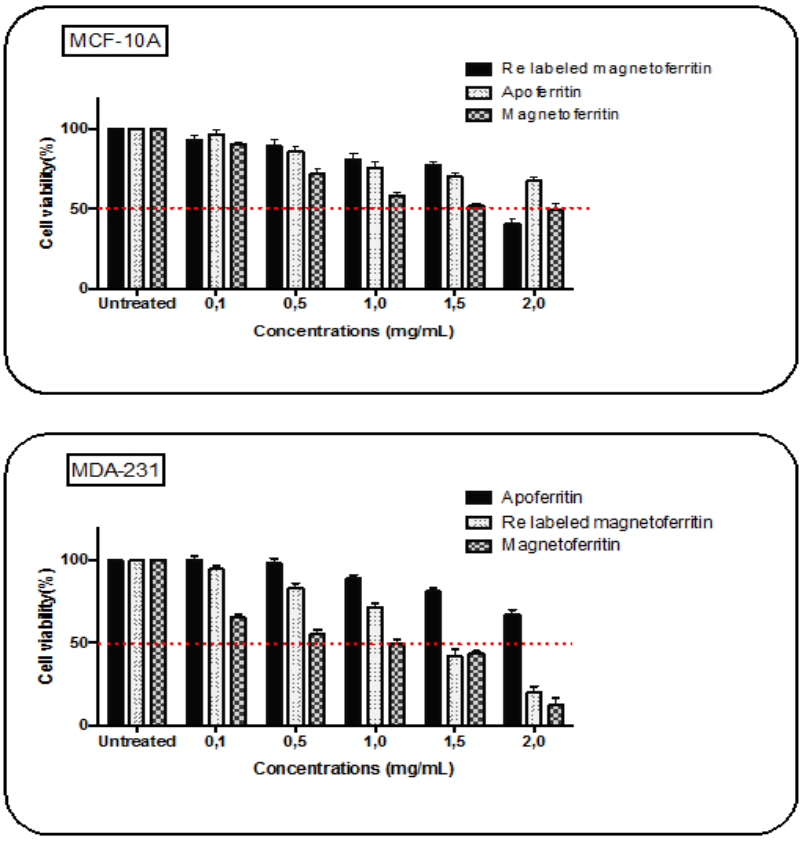

Figure 63. XTT assay results for MDA-MB-231 and MCF-10A cell lines following 72h exposure to apoferritin, magnetoferritin, and Re-labeled magnetoferritin samples. Error bars represent the standard deviation of the absorbance at 415 nm.

As seen in Figure 63, the cytotoxicity of apoferritin was lower than that of magnetoferritin and Re-labeled magnetoferritin even at high protein concentrations.

IC_{50} values of Re-labeled magnetoferritin sample were determined for MCF-10A and MDA-MB-231 cells at 72h and it was found to be 1,83 mg/mL and 1,34 mg/mL, respectively and these values were 1,73 mg/mL and 0,96 mg/mL for magnetoferritin sample. Since the cytotoxic effects of the samples in cancerous cells are of importance for the future investigations, IC_{50} concentration was found to be 1 mg/mL according to the toxic concentration in cancerous cells.

3.8.2 Annexin V-FITC/PI Assay

To understand the apoptotic nature of cell death in cancerous and noncancerous cells upon exposure of the Re-labeled magnetoferritin protein nanoparticles, three distinct concentrations and exposure times, that were 0.5, 1, 1.5 mg/mL (0,5 IC_{50}, IC_{50} and 1,5 IC_{50} values, respectively) as concentrations and 24, 48, 72h as exposure times, were performed in the wake of XTT assay.

Typical flow cytometry profiles for the MDA-MB-231 and MCF-10A cells treated with Re-labeled magnetoferritin samples at 0.5 mg/mL, 1 mg/mL and 1.5 mg/mL for 24, 48, 72h. The datum is shown in Appendix A and Appendix B.

Cell cycle histograms of untreated cells, used as negative control, showed a characteristic growth profile and etoposite were used as positive control that indicated the assay system was working correct since etoposite is a drug that is known to be undergoing apoptosis. Annexin V and PI stains were used to detect apoptotic and necrotic population, respectively. In the profiles, Area A1 gives the population of viable cells, A2 is for necrotic population, A3 and A4 is for late and early apoptotic populations, respectively.

Evaluation of the cells treated with nanoparticles showed distinct populations indicative of cells progressing through early- and late-stage apoptosis, thus it is confered from the cytometry profiles that cell deaths mostly result from apoptotic events rather than necrotic ones since necrotic events' proportion over total events is between 0.2 – 2.3 % based upon the concentration and/or exposure time, so it is seen that apoptosis is the main mechanism of cell damage in both cell types exposed to nanoparticles. From the flow cytometry profiles, apoptotic cell populations, considering the total population of early and late apoptosis, were obtained and given in Figure 64.

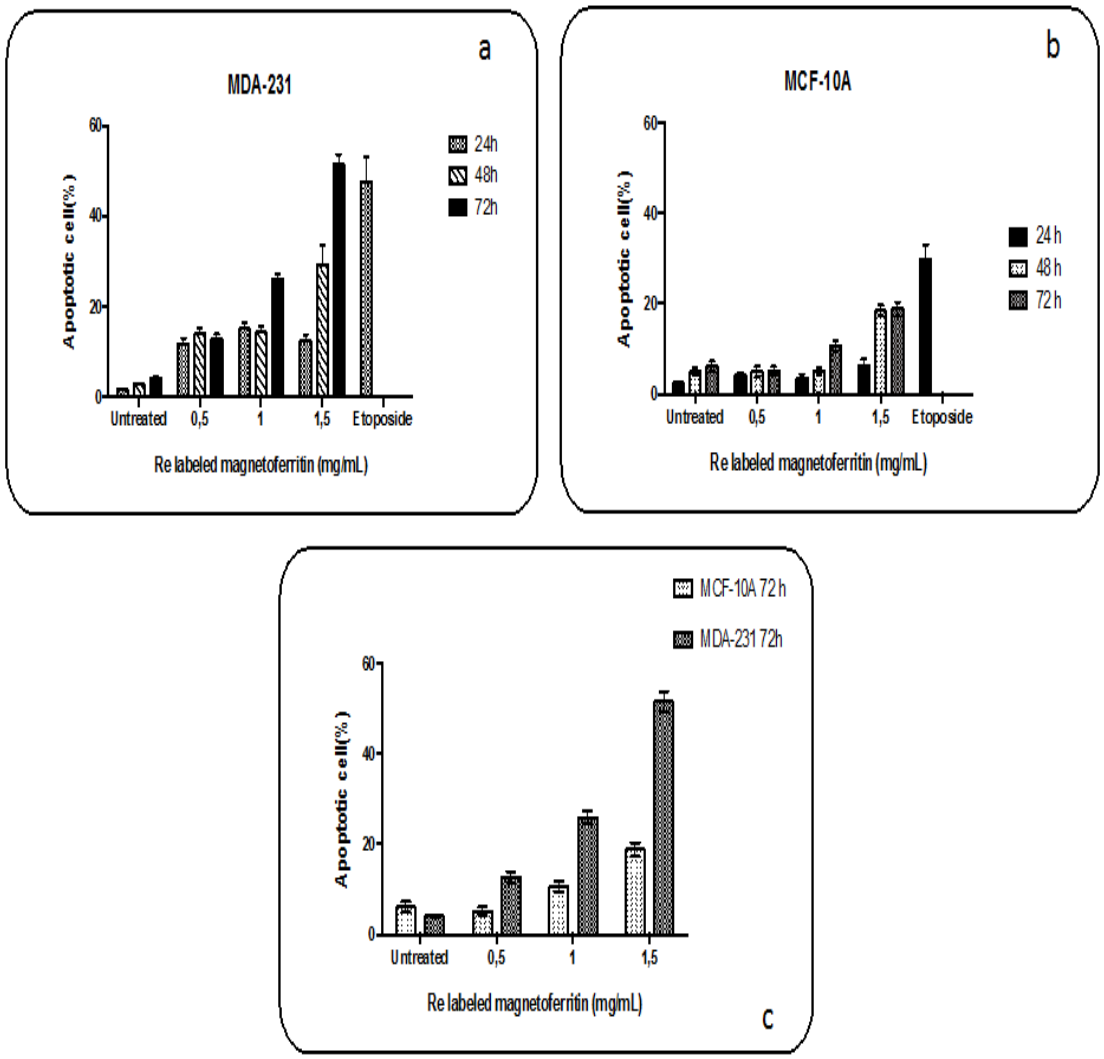

Figure 64. Graphs for the apoptotic cell populations at different concentrations and times upon the exposure to Re-labeled magnetoferritin nanoparticles over 3 experiments. Error bars indicate the standard deviation.

Following 72h exposure of nanoparticles with the concentration of 1.5 mg/mL, MDA-MB-231 cell cycle profiles changed dramatically and the apoptotic cell percentange increased over 50% while that was still below 50% for MCF-10A cells. The reason of cancerous cells having higher apoptosis rate than healthy cells is their characteristics showing susceptibility of cancer cells to the nanoparticles.

Thus, the induction of apoptosis in cancerous cells may be a guide for experimental cancer therapies.

3.8.3 Uptake Studies

In order to quantify the amount of rhenium taken up by the cells, MDA-MB-231 and MCF-10A cells were incubated with Re-labeled magnetoferritin samples under varying incubation times.

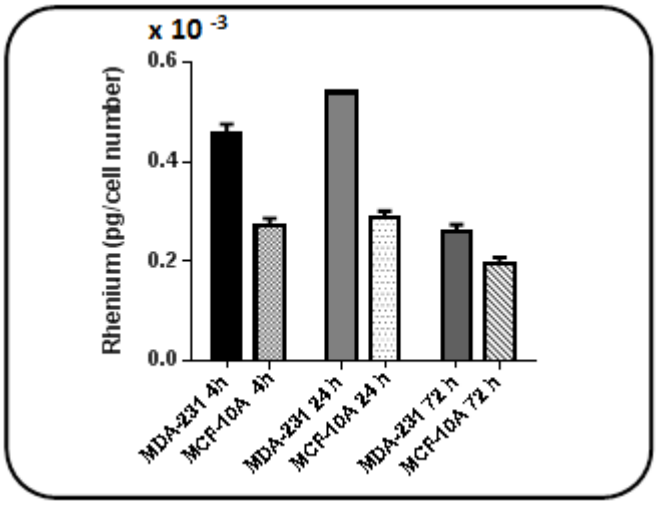

Figure 65. Rhenium concentration in MDA-MB-231 and MCF-10A cells exposed to Re-labeled magnetoferritin nanoparticles at the concentration of 1 mg/mL for 4h, 24h and 72h.

In Figure 65, it was seen that the uptake of nanoparticles by both of the cells significantly increased in the first 4 hours and showed a time-dependent feature, however the uptake rate gradually slowed after 24h incubation. Compared with the healthy cells, cancerous cells exhibited the highest uptake rate.

The uptake amount increased by 15.3% and by 5.4% for 24h incubated cells when compared with the 4h incubated cells, respectively in MDA-MB-231 and MCF-10A

cells when the dosing concentration of nanoparticles was at the constant concentration of 1 mg/mL.

There was also a significant decrease in the uptake of nanoparticles in the cells after 72h incubation. It was thought that exocytosis of the nanoparticles had started in 72h incubation and the uptake rate showed a higher decrease in cancerous cells than the healthy cells since the membrane integrity might have been disturbed in the cancerous cells upon exposure and/or absorbtion of the nanoparticles on the cell membrane. The reduction was 52.2% and 31.2% for 72h incubated cells, respectively in MDA-MB-231 and MCF-10A cells when compared with the 24h incubated cells.

3.8.4 Prussian Blue Staining

Prussian blue staining was utilized for qualitative detection of iron remained within the cells. As control treatments, MDA-MB-231 and MCF-10A cells without incubation of nanoparticles were stained. According to the uptake assay results, rhenium uptakes in both cell lines after 24h incubation are higher than that of after 4h and 72h incubations, thus staining experiments were performed after 24h incubation with the nanoparticles. As seen in Figure 66, Figure 67 and Figure 68, it was seen that rhenium labeled nanoparticles were taken up by both cell types.

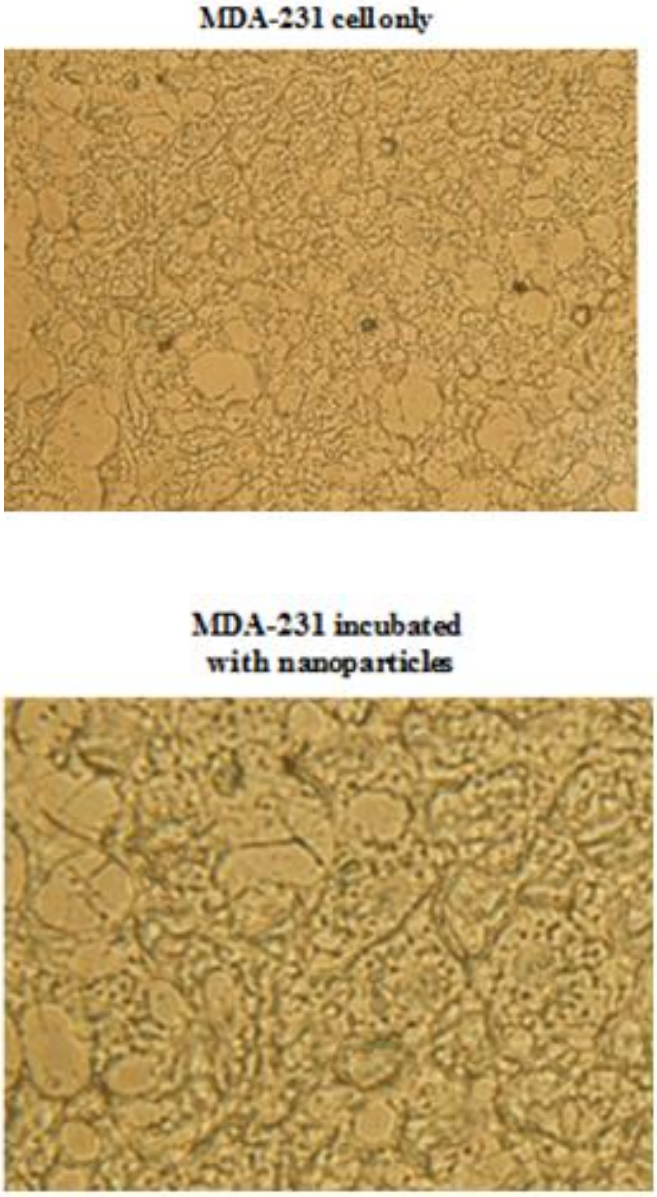

Figure 66. Optical micrographs of Prussian blue staining of MDA-MB-231cells incubated for 24h with magnetoferritin samples.

The scale bar in the images is 20 mm.

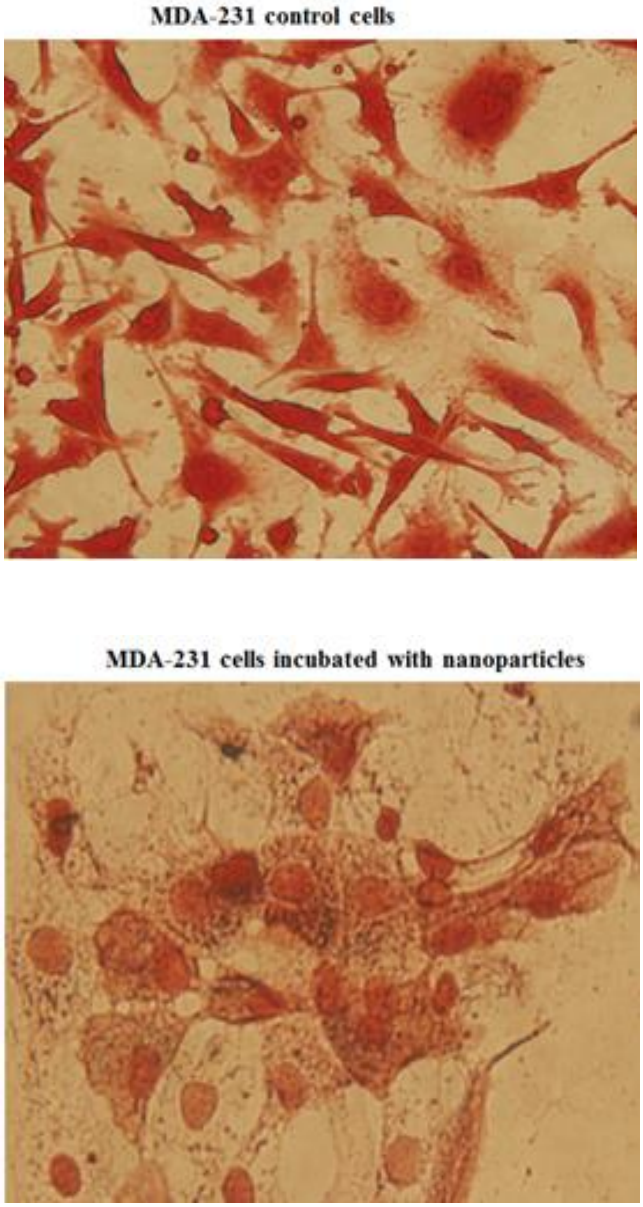

Figure 67. Optical micrographs of Prussian blue staining and following counterstaining with nuclear fast red of MDA-MB-231 cells.

Both cells were incubated for 24h with magnetoferritin samples. The scale bar in the images is 200 mm.

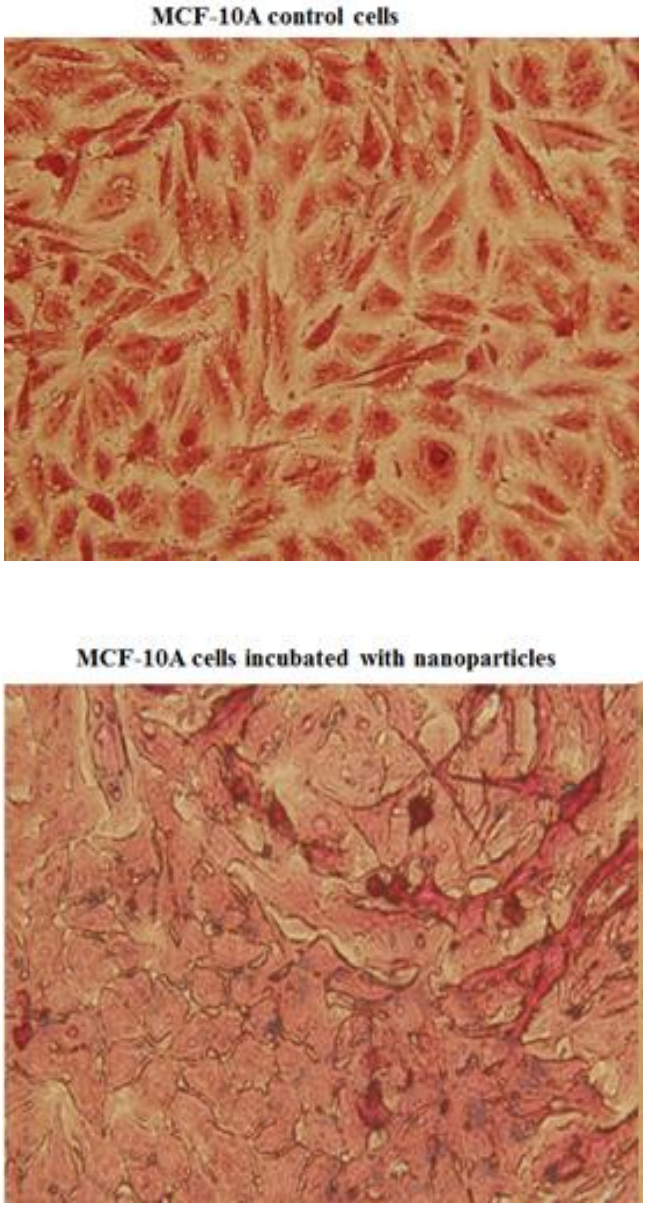

Figure 68. Optical micrographs of Prussian blue staining and following counterstaining with nuclear fast red of MCF-10A cells.

Both cells were incubated for 24h with magnetoferritin samples. The scale bar in the images is 200 mm**.** It was seen that nanoparticles were taken up by cancerous cell lines more than the healthy cells as expected (Figure 66 and Figure 67).

It is also obvious that the nanoparticles are accumulated in cytoplasm and it could be seen by the help of counterstain, especially in Figure 67.

3.9 Peroxidase-like Activity of Magnetoferritin Samples

In the previous studies, it was found that magnetoferritin catalyzes hydrogen peroxide oxidation of substrates such as 3,3′-Diaminobenzidine (DAB). To understand the mechanism of magnetoferritin based peroxidase like reaction and the effect of iron loading on the activity, we monitored the activity of magnetoferritin samples by using the same concentrations of protein and same concentrations of iron, in separate experiments.

When DAB and H_2O_2 is added, the reaction proceeds like other enzymatic reactions with this substrate. The radical formations occur on the surface of the nanoparticle and the radicals formed during the reaction give rise to the catalytic oxidation of DAB. The oxidized DAB produces a brown reaction product and water as shown in the Figure 69.

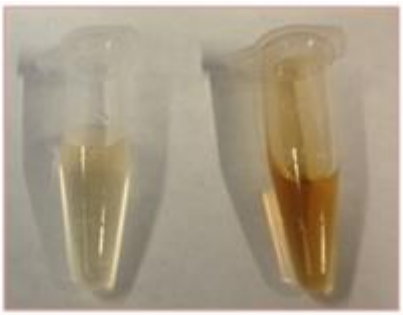

$$Fe^{2+} + H_2O_2 \longrightarrow Fe^{3+} + OH^- + \cdot OH$$

$$Fe^{3+} + H_2O_2 \longrightarrow Fe^{2+} + H^+ + \cdot HO_2$$

$$DAB + H_2O_2 \text{ ----------Magnetoferritin----------> } DAB\ ppt + H_2O$$

Figure 69. The picture of the samples before and after the redox reaction and the oxidation mechanism of DAB.

Activity tests were carried out on magnetoferritin samples with 798 Fe, 2590 Fe and 5329 Fe loadings by using two sets of experiments by following absorbance of oxidized DAB for 1 hour at 455 nm.

First set of experiment includes the reactions that were carried out with the same concentrations of protein, so with varying iron concentrations and the second set of experiments includes the reactions that were carried out the same concentrations of iron.

The plots for the samples with different loadings were compared with the control experiments as seen in Figure 70. A control experiment is done with apoferritin instead of magnetoferritin and the other is done with reaction buffer in the absence of protein.

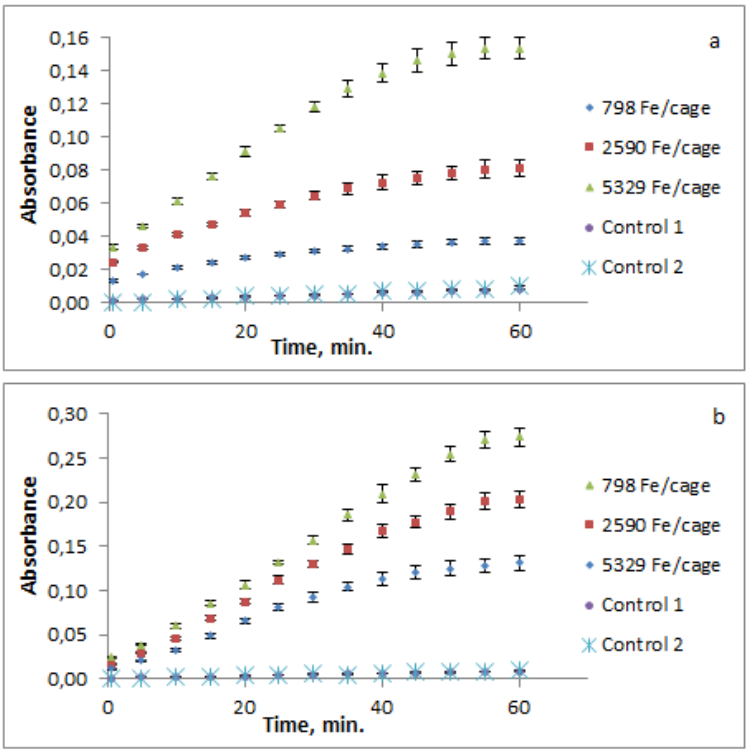

Figure 70. Plot of Absorbance versus time for samples with a. the same protein concentration, b. the same iron concentration.

Samples with different iron loadings give rise to different initial absorbances as seen in the graphs (Figure 70). Control 1 defines activity test with apoferritin sample and control 2 defines activity test with the absence of protein.

It was seen from the control experiments that apoferritin did not show any activity under same conditions and in the absence of magnetoferritin, oxidation of DAB is negligible. As seen in the Figure a, magnetoferritin samples showed different levels of activity towards DAB in the order of increased iron loadings. Since the radical formation is promoted by the amount of iron ions on the surface, the peroxidase activities are dependent on iron content, with higher iron content having higher activities. We also observed a decrease for the samples with the higher iron loadings when the same iron amounts used for the experiment as seen in Figure b. When the same amount of iron used for the samples with different loadings, the number of protein cages will be higher in the samples with the lower loadings that means higher number of nanoparticle cores. Thus this will result in higher number of iron atoms on the surface in the sample with lower loading and so higher activity.

3.10 Magnetic Relaxivity Properties of Magnetoferritin Samples: Effect of Loading Factor

To investigate the effect of iron loading and particle size on the relaxivity, T_2 and T_1 times of magnetoferritin samples were measured at two different frequencies, 90 and 300 MHz.

For the T1 measurements, an inversion recovery pulse sequence (90º pulse width of 6.3 μs with 8 experiments of 4 scan at 90 MHz frequency and 90º pulse of 15 μs with 16 experiments of 4 scan at 300 MHz frequency) at 298 K, where the relaxation delay was set to six times the estimated T1, was used.

For the T2 measurements, an CPMG pulse sequence (90º pulse of 6.3 μs with 8 experiments of 4 scan at 90 MHz frequency and 90º pulse of 15 μs with 16 experiments of 4 scan at 300 MHz frequency) at 298 K, was used.

A plot of the inverse T_1 or T_2 versus iron concentration (mM) was used to determine the relaxivity values (r_1, r_2), ($mM^{-1}.s^{-1}$), where relaxivity per iron is equal to the slope of the line. As shown in Figure 71 and Figure 72, ($1/T_2$ and $1/T_1$) as a function of Fe concentration are plotted.

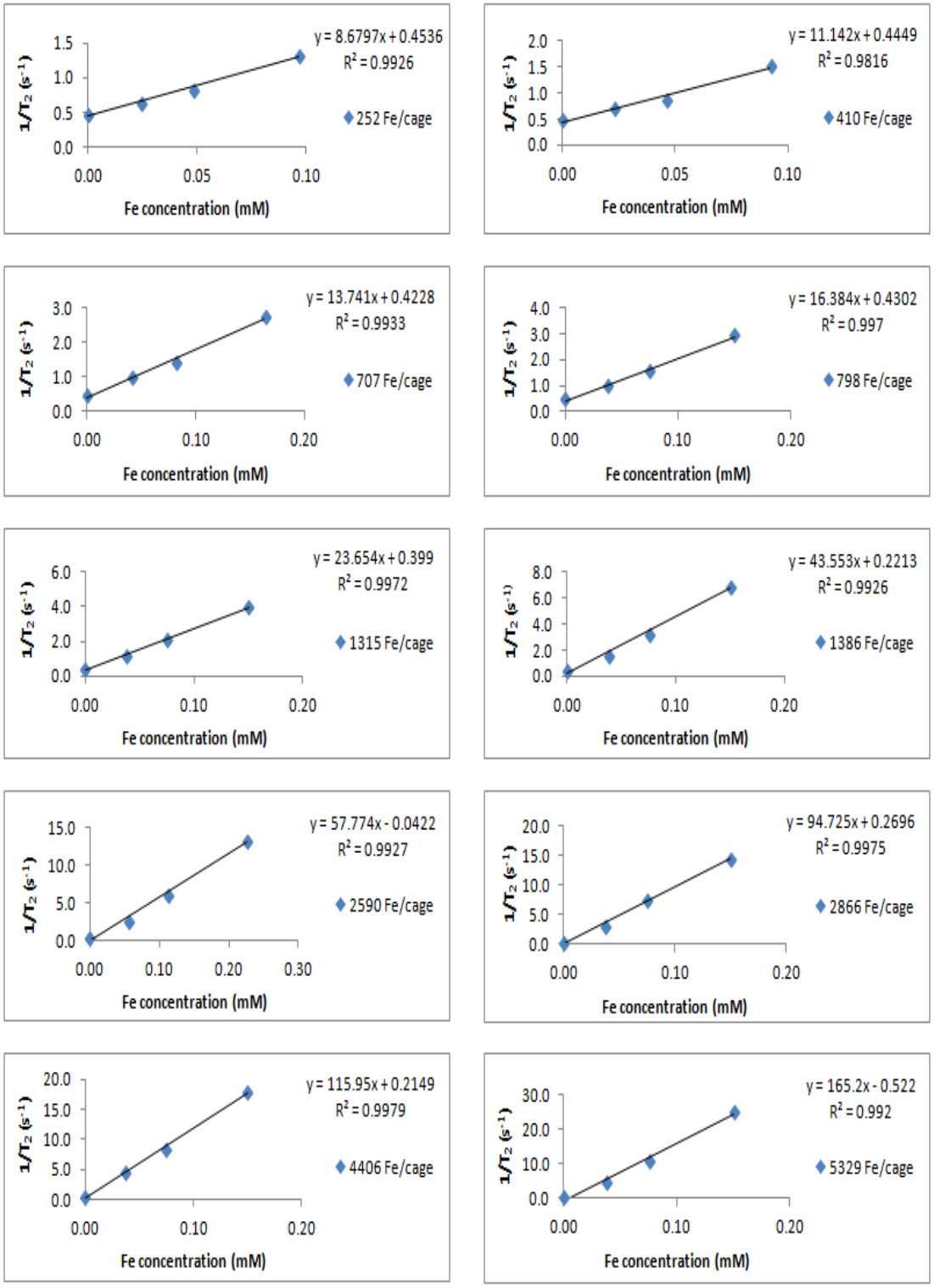

Figure 71. Plot of $1/T_2$ (s^{-1}) versus Fe concentration (mM) under 300 MHz.

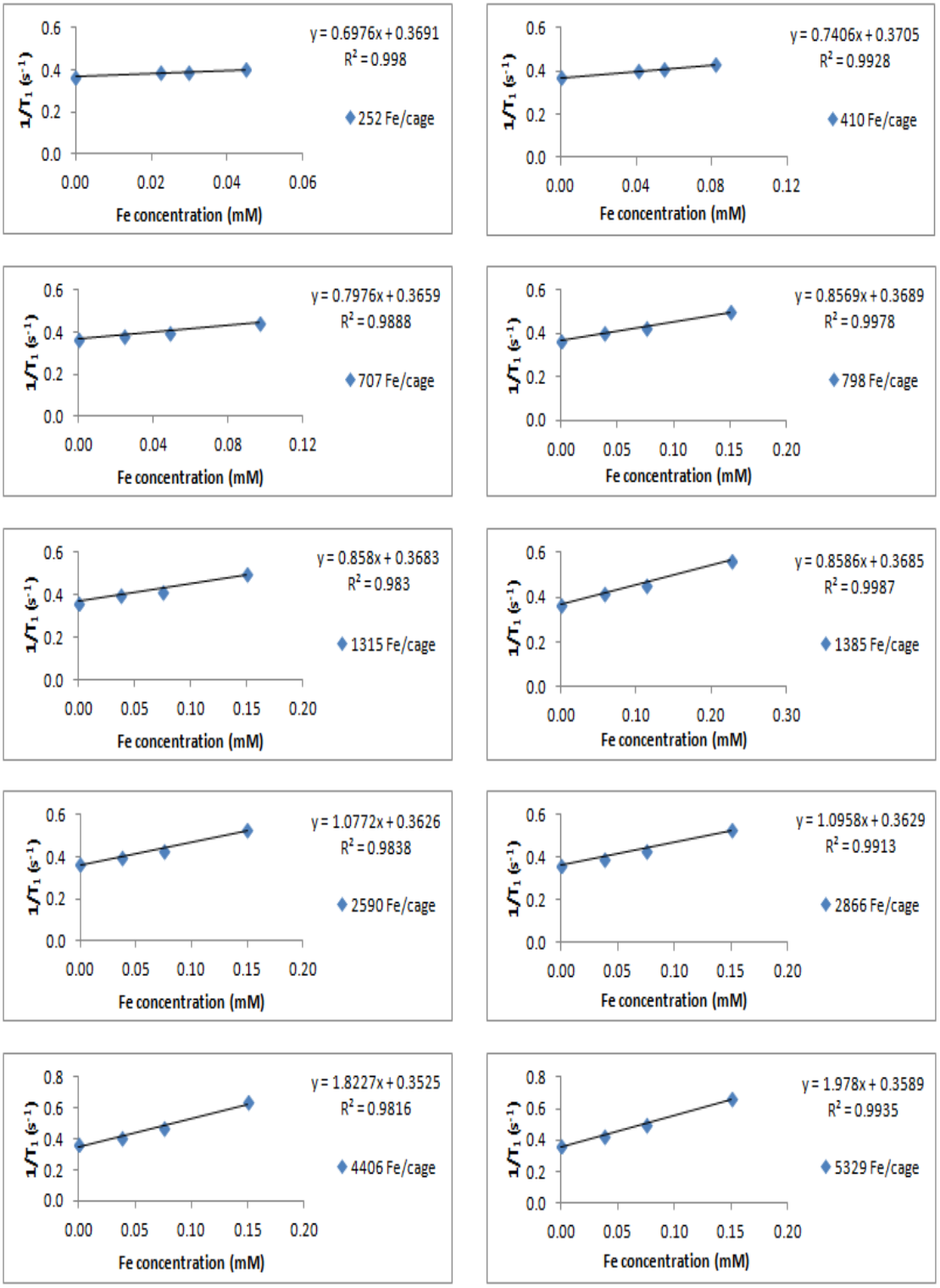

Figure 72. Plot of $1/T_1$ (s^{-1}) versus Fe concentration (mM) under 300 MHz.

In Figure 71 and Figure 72, R^2 value that is close to 1 indicates a good fit, with slope equal to ionic relaxivity.

In order to evaluate the r_2 and r_1 trend obtained under 300 MHz for the magnetoferritin samples with increasing Fe loadings, the plot of r_2 $(mM.s)^{-1}$ and r_1 $(mM.s)^{-1}$ versus the number of Fe/cage were fitted as seen in Figure 73.

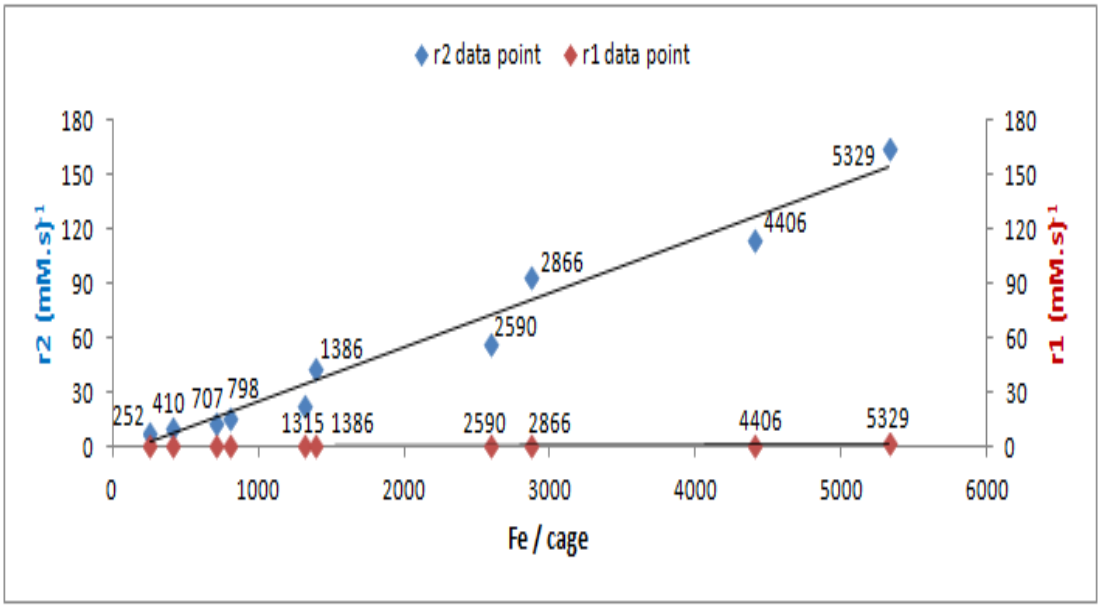

Figure 73. Plot of r_2 $(mM.s)^{-1}$ and r_1 $(mM.s)^{-1}$ versus number of Fe/cage.

It was seen from the plots that the r_2 relaxivity increases with increasing loading factors and r_1 relaxivity does not show a considerable change with different loadings. T_2 and T_1 relaxation times of samples with a low Fe loading and a high Fe loading were also measured under 90 MHz magnet in order to evaluate the frequency dependence of relaxation.

Figure 74 and Figure 75 shows ($1/T_1$ and $1/T_2$) as a function of Fe concentration, respectively, with the results from both 90 MHz and 300 MHz and the slopes evaluated as the relaxivities r2 and r1 ($mM^{-1}.s^{-1}$).

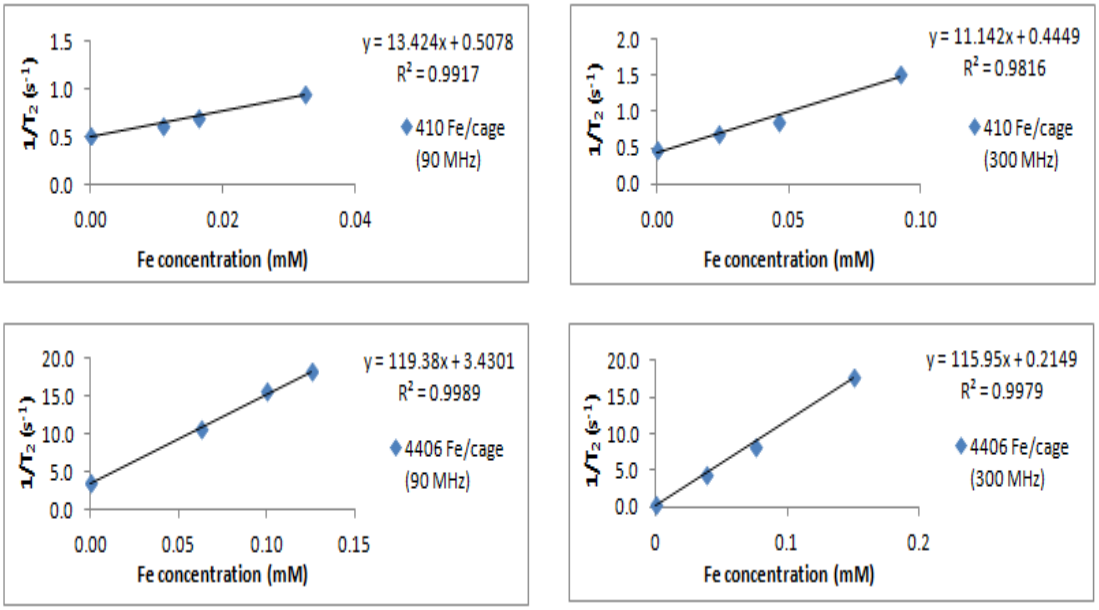

Figure 74. Plot of $1/T_1$ (s^{-1}) versus Fe concentration (mM) obtained by both 90 MHz and 300 MHz magnet.

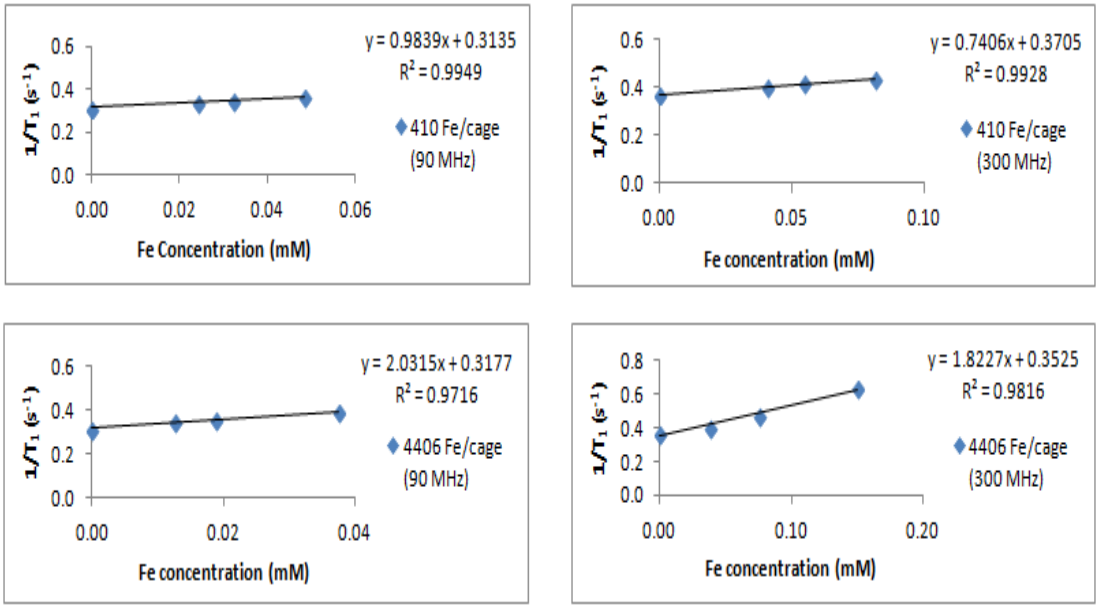

Figure 75. Plot of $1/T_2$ (s^{-1}) versus Fe concentration (mM) obtained by both 90 MHz and 300 MHz magnet.

It was seen that r2 and r1 relaxivities measured under 90 MHz were slightly higher than that of 300 MHz instrument and the results of the samples with low and high loadings showed the similar trend under lower frequency when compared to that of higher frequency instrument.

As a result, by using cage like architecture of HFn for the synthesis of iron oxide nanoparticles, the mineralization of HFn with different iron loadings can be controlled. This control over provides us to investigate the effect of loading factors on peroxidase-like activity and r1, r2 relaxation of magnetoferritin.

Based on the peroxidase activity tests, it was found that the apoferritin sample, without a mineral core, exhibited no activity that means the observed activity arises from the iron oxide nanoparticles. Magnetoferritin samples showed different levels of activity according to their iron loading factors. As H_2O_2 diffuses into the ferritin cavity, radical formation mechanism occurs by the interaction of iron ions on the surface of the iron oxide nanoparticle. Peroxidase activity depends on the radical formation on the nanoparticle suface, since the radicals formed oxidizes the substrate. So, it is important to be existed more iron ions on the surface for the higher activity. As expected, activity increased considerably with the iron loading factors.

Interestingly, it was also seen a decrease in activity for the samples with the higher loadings when the same iron amounts of samples with different loadings were used. When the same amount of iron used for the samples with different loadings, the number of protein cages will be higher in the samples with the lower loadings. Thus this will result in higher number of iron atoms on the surface in the sample with lower loading. We also inferred from this result that metal growth mechanism occurred at the different sites of the protein interior wall forming discrete nanoparticles during the mineralization reaction, so the total number of iron atoms on the discrete surfaces per cage becomes higher in lower loadings and this results in an increase in activity even if the iron concentrations are same for all the samples. This interpretation is also consistent with the relaxivity observed as discussed below.

We found that r_2 relaxivity increases with the increasing iron loading. Since r_2 relaxativity is the spin–spin relaxation that results from the dephasing of the water protons due to the net magnetization created by magnetic nanoparticles, the relaxation process arises from the interaction between water proton spins and net magnetic moment of the iron atoms. The magnetic properties of the iron oxide nanoparticles strongly depend on the particle size. The magnetic moments of the particles are proportional with the particle sizes, so as loading factor increases, particle size increases and this causes an increase in magnetic moment and relaxivity. The crystal structures of the particles also affect the magnetic properties of the particles. Magnetoferritin samples consist of mainly magnetite (Fe_3O_4) and/or maghemite (γ- Fe_2O_3) and may consist of a small amount of ferrihydrite (FeOOH) particles due to the exposure of air oxidation even to a small extent. The two iron oxide structures (magnetite and maghemite) possess similar magnetic properties and differ highly from the ferrihydrite particles. The slight deviations from the linearity in the relation between r_2 relaxivity and iron loading may result from the possibility of these crystal structure differences.

However r_1 relaxivity did not change considerably with the loading factors in contrast to r2 relaxivity. There is a very small increase with varing iron loadings in r1 ranging from 0.69 $mM^{-1}.s^{-1}$ and 1.98 $mM^{-1}.s^{-1}$ as seen in Figure 76.

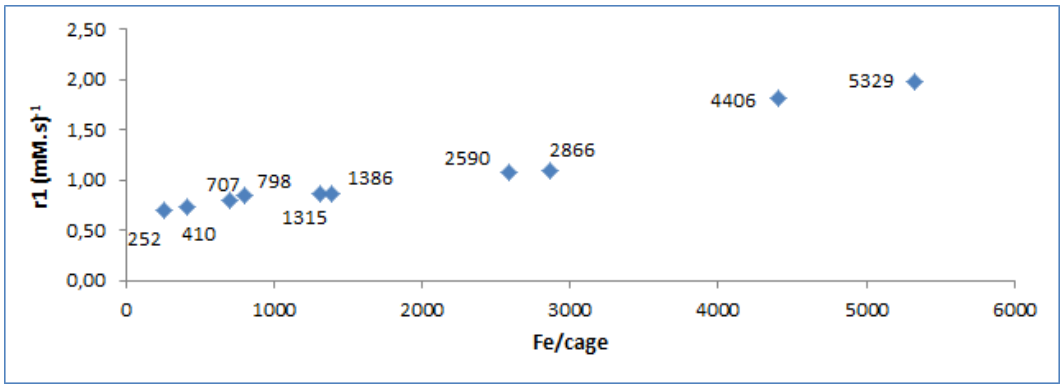

Figure 76. Plot of r_1 $(mM.s)^{-1}$ versus number of Fe/cage.

r_1 relaxivity is the spin-lattice relaxation that results from the chemical interchange between the bound water of the paramagnetic agents and the water molecules that is freely moving within the cavity and the relaxation is mainly controlled by three parameters; the mean residence lifetime for metal-bound water (τ_M), the rotational correlation time (τ_R) and the number of metal-bound water molecules (q).

The mean residence lifetime (τ_M) is determined by the diffusion rate of surrounding free water across the protein shell and the water exchange rate with the iron ions on the particle surface. For the magnetoferritin samples with different loadings, τ_M times will not vary at all between the samples since the surrounding molecule is ferritin and the water molecule exchange is with iron ions for all being compared. The rotational correlation time (τ_R) is related with the molecular weight of the protein, so it is not the parameter that is leading to the relaxivity trend since all samples were synthesized in ferritin.

Iron atoms exist on the particle surface creates r_1 relaxivity due to the the bound water with the surface iron ions; that can continuously interact with the surrounding free water and increase the T_1 relaxation of nuclear spins. So the number of metal-bound water molecules (q) is important and in order to investigate the r_1 trend with increasing iron loadings, the number of Fe atoms on the particle surface should be considered to be able to compare the relaxivities of the magnetoferritin samples.
It is conferred from the results that the formation of discrete nanoparticles occurs at the different sites of the protein interior wall most likely in the lower loadings and as the loading continues, the particles probably become part of the core. Crystal growth occurs by the addition of Fe^{2+} that is oxidized on the surface of the growing crystallite (Figure 77).

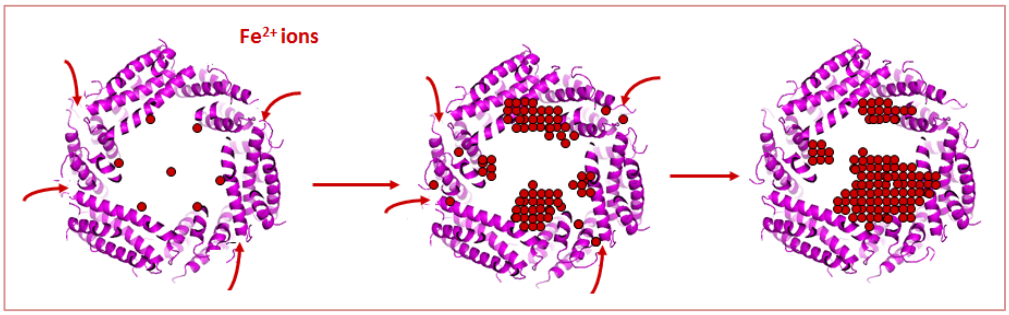

Figure 77. The passage of Fe^{2+} ions into the cavity is showed by the arrows.

As illustrated in the Figure 77, in the early stage of reaction there may be several nucleation centers, but as the core formation improves then it will be dominated by one such center. This means that at relatively low iron to protein ratios, small clusters can be formed in some of the nucleation centers.

Thus, for every relatively smaller particle in the protein cavity; the total number of iron ions on the surfaces becomes close to or bigger than that of one bigger particle. So the relaxivity does not exhibit a considerable increase with the increased loadings.

CHAPTER 4

CONCLUSION

Different sizes of magnetic Fe_3O_4, γ-Fe_2O_3 particles were successfully prepared in the ferritin protein cages (magnetoferritin). Mineralization of these magnetic materials was performed for the aim of targeting nanoparticles by magnetic field.

Rhenium tricarbonyl complex, $[Re(CO)_3(H_2O)_3]^+$ was synthesized by a reductive carboxylation process using non-radioactive isotope of rhenium salt; sodium perrhanate ($NaReO_4$), since working with radioactive elements is not possible in our laboratories. The procedure allows an easy labeling of biomolecules. The prepared complex was successfully purified from remaining perrhanate ions by passing the complex solution from an anion exchange column and characterized by a HPLC-ICP-MS system.

The chemical modification of the ferritin cage can be readily performed by immobilization of histidine molecule on the exterior surface and then protein cage can be labeled using rhenium tricarbonyl complex, $[Re(CO)_3(H_2O)_3]^+$. As a control experiment, rhenium-tri carbonyl complex was bound with the amine groups that naturally exist on the exterior surface of ferritin without surface modification. It was found that the rhenium-tri carbonyl complex was bound to histidine-conjugated ferritin surface ~ 6 fold more than those bound to non-modified ferritin surface. The stability of the Re-labeled magnetoferritin was tested in PBS and human blood serum for 3 days.

After 3 days, the amounts of Re still bound to protein went upto 91% and 88% for serum and PBS buffer, respectively. Thus, it can be proposed as an imaging agent for the diagnosis and therapy of the cancerous cells and tissues.

Toxicity tests of the Re-labeled magnetoferritin were performed bu using cancerous (MDA-MB-231) and healthy (MCF-10A) cell lines. The assays were also applied to magnetoferritin without modification and apoferritin for the comparison of the toxicity effects. It was found that the surface modification and its encapsulation with the nanoparticles of the inner cavity did not alter the biocompatibility of those different forms of ferritin nanocages to a large extent. Therefore the usage of the protein cage as a template holds promise for the future experimental cancer research. Using Annexin V/PI Staining assays, it was found that the percentage of apoptotic events is higher than that of other events (necrosis or proliferation) upon exposure to the nanoparticles, so apoptosis is the main mechanism of cell damage in both cell types. The uptake of nanoparticles by both types of the cells increased in the first 4 hours and gradually slowed down after 24 hours of incubation. Compared with the healthy cells, cancerous cells exhibited the highest uptake rate of nanoparticles.

In additon to these studies, relaxivity and peroxidase properties of magnetoferritin samples with different iron loadings were investigated at Douglas Lab. MSU, USA. The magnetoferritin samples showed a clear size dependence on their relaxivity and peroxidase properties. There was seen an increase in r2 relaxivity with the iron loadings and the sample with the highest iron loading of 5329 Fe/cage (experimentally found loading factor) has r2 value of 165,2 $mM^{-1}.s^{-1}$ at room temperature and at a frequency of 300 MHz. However there was not seen a considerable change in r_1 relaxivities with various loadings and the r1 relaxivity value for the sample with highest iron loading of 5329 Fe/cage (experimentally found loading factor) was found as 1,98 $mM^{-1}.s^{-1}$. The high r_2 value demonstrates that magnetoferritin nanoparticles may serve as T_2 contrast agents in magnetic resonance imaging with high efficiency when compared with commercially used iron oxide MRI contrast agents. It was conferred from the r1 relaxation results that during the mineralization reaction, metal growth mechanism occurred at the different sites of the protein interior wall that forms discrete nanoparticles, so the total number of iron atoms on the discrete surfaces per cage becomes higher in lower iron loadings and for each relatively smaller particle in the protein cavity; the total number of iron

ions on the surfaces becomes close to that of one bigger particle, so the relaxivity does not exhibit a considerable increase with the increased iron loadings.

This protein cage structures are good platforms for the preparation of cancer therapy and diagnosis agents, since their exterior surface can be modified by incorporating some targeting moieties and some therapeutic agents can be encapsulated inside the cavity of the proteins. Therefore, as a future work, these ferritin systems can be loaded with some drugs and directed to a specific region especially that having ferritin receptors and the drug release in the region can be investigated.

REFERENCES

[1] R. Ladj, A. Bitar, M. Eissa, Y. Mugnier, R. Le Dantec, H. Fessi, et al., Individual inorganic nanoparticles: preparation, functionalization and in vitro biomedical diagnostic applications, J. Mater. Chem. B. 1 (2013) 1381–1396. doi:10.1039/c2tb00301e.

[2] P. Tartaj, M.P. Morales, T. González-Carreño, S. Veintemillas-Verdaguer, C.J. Serna, Advances in magnetic nanoparticles for biotechnology applications, J. Magn. Magn. Mater. 290-291 (2005) 28–34. doi:10.1016/j.jmmm.2004.11.155.

[3] D.K. Yi, S.S. Lee, G.C. Papaefthymiou, J.Y. Ying, B. Way, T. Nanos, et al., Nanoparticle Architectures Templated by SiO_2 / Fe_2O_3 Nanocomposites, 18 (2006) 614–619.

[4] A.K. Nikumbh, R.A. Pawar, D.V. Nighot, G.S. Gugale, M.D. Sangale, M.B. Khanvilkar, et al., Structural, electrical, magnetic and dielectric properties of rare-earth substituted cobalt ferrites nanoparticles synthesized by the co-precipitation method, J. Magn. Magn. Mater. 355 (2014) 201–209. doi:10.1016/j.jmmm.2013.11.052.

[5] A.H. Lu, E.L. Salabas, F. Schüth, Magnetic nanoparticles: synthesis, protection, functionalization, and application., Angew. Chem. Int. Ed. Engl. 46 (2007) 1222–44. doi:10.1002/anie.200602866.

[6] Z. Ma, Y. Guan, H. Liu, Superparamagnetic silica nanoparticles with immobilized metal affinity ligands for protein adsorption, J. Magn. Magn. Mater. 301 (2006) 469–477. doi:10.1016/j.jmmm.2005.07.027.

[7] I. Pastoriza-santos, J. Pe, L.M. Liz-marza, Silica-Coating and Hydrophobation of CTAB-Stabilized Gold Nanorods, Chem. Mater. 18 (2006) 2465–2467.

[8] W. Wu, Q. He, C. Jiang, Magnetic iron oxide nanoparticles: synthesis and surface functionalization strategies., Nanoscale Res. Lett. 3 (2008) 397–415. doi:10.1007/s11671-008-9174-9.

[9] V. Sundaresan, J.U. Menon, M. Rahimi, K.T. Nguyen, A.S. Wadajkar, Dual-responsive polymer-coated iron oxide nanoparticles for drug delivery and imaging applications., Int. J. Pharm. 466 (2014) 1–7. doi:10.1016/j.ijpharm.2014.03.016.

[10] V.K. Gupta, N. Atar, M.L. Yola, Z. Üstündağ, L. Uzun, A novel magnetic Fe@Au core–shell nanoparticles anchored graphene oxide recyclable nanocatalyst for the reduction of nitrophenol compounds, Water Res. 48 (2014) 210–217. doi:10.1016/j.watres.2013.09.027.

[11] E.N. Esenturk, A.R. Hight Walker, Gold nanostar @ iron oxide core–shell nanostructures: synthesis, characterization, and demonstrated surface-enhanced Raman scattering properties, J. Nanoparticle Res. 15 (2012) 1364–1373. doi:10.1007/s11051-012-1364-9.

[12] M. Uchida, M.L. Flenniken, M. Allen, D.A. Willits, B.E. Crowley, S. Brumfield, et al., Targeting of Cancer Cells with Ferrimagnetic Ferritin Cage Nanoparticles, J. Am. Chem. Soc. 312 (2006) 16626–16633.

[13] H. Yoshimura, Protein-assisted nanoparticle synthesis, Colloids Surfaces A Physicochem. Eng. Asp. 282-283 (2006) 464–470.

[14] B.M. Allen, D. Willits, J. Mosolf, M. Young, T. Douglas, Protein Cage Constrained Synthesis of, Adv. Mater. 14 (2002) 2000–2003.

[15] M. Uchida, M.T. Klem, M. Allen, P. Suci, M. Flenniken, E. Gillitzer, et al., Biological Containers: Protein Cages as Multifunctional Nanoplatforms, Adv. Mater. 19 (2007) 1025–1042. doi:10.1002/adma.200601168.

[16] P. Bhattacharya, D. Du, Y. Lin, Bioinspired nanoscale materials for biomedical and energy applications., J. R. Soc. Interface. 11 (2014) 1067–1080. doi:10.1098/rsif.2013.1067.

[17] A. Chen, Y. Bao, X. Ge, Y. Shin, D. Du, Y. Lin, Magnetic particle-based immunoassay of phosphorylated p53 using protein cage templated lead phosphate and carbon nanospheres for signal amplification, RSC Adv. 2 (2012) 11029–11034. doi:10.1039/c2ra20994b

[18] L. Schoonen, J.C.M. van Hest, Functionalization of protein-based nanocages for drug delivery applications., Nanoscale. 6 (2014) 7124–41. doi:10.1039/c4nr00915k.

[19] N.M. Molino, S.-W. Wang, Caged protein nanoparticles for drug delivery., Curr. Opin. Biotechnol. 28 (2014) 75–82. doi:10.1016/j.copbio.2013.12.007.

[20] N.P. King, J.B. Bale, W. Sheffler, D.E. McNamara, S. Gonen, T. Gonen, et al., Accurate design of co-assembling multi-component protein nanomaterials., Nature. 510 (2014) 103–108. doi:10.1038/nature13404.

[21] R.M. Kramer, C. Li, D.C. Carter, M.O. Stone, R.R. Naik, B. Group, et al., Engineered Protein Cages for Nanomaterial Synthesis, J. Am. Chem. Soc. (2004) 13282–13286.

[22] M.L. Flenniken, D. a Willits, A.L. Harmsen, L.O. Liepold, A.G. Harmsen, M.J. Young, et al., Melanoma and lymphocyte cell-specific targeting incorporated into a heat shock protein cage architecture., Chem. Biol. 13 (2006) 161–70. doi:10.1016/j.chembiol.2005.11.007.

[23] M. Uchida, S. Kang, C. Reichhardt, K. Harlen, T. Douglas, The ferritin superfamily: Supramolecular templates for materials synthesis., Biochim. Biophys. Acta. 1800 (2010) 834–45. doi:10.1016/j.bbagen.2009.12.005.

[24] B.S. Mann, F.C. Meldrum, Controlled Synthesis of Inorganic Materials using Supramolecular Assemblies, Adv. Mater. 3 (2000) 316–318.

[25] S.P. Martsev, a. P. Vlasov, P. Arosio, Distinct stability of recombinant L and H subunits of human ferritin: calorimetric and ANS binding studies, Protein Eng. Des. Sel. 11 (1998) 377–381. doi:10.1093/protein/11.5.377.

[26] W. Jin, H. Takagi, B. Pancorbo, E.C. Theil, “Opening” the Ferritin Pore for Iron Release by Mutation of Conserved Amino Acids at Interhelix and Loop Sites, Biochemistry. 40 (2001) 7525–7532. doi:10.1021/bi002509c.

[27] K. Kumar, Iron Assay and Size Exclusion High Performance Liquid Chromatography of Ferritin and Magnetoferritin, J. Liq. Chromatogr. Relat. Technol. 20 (1997) 3351–3364. doi:10.1080/10826079708005836.

[28] D.M. Vriezema, M.C. Aragone, J.A.A.W. Elemans, J.J.L.M. Cornelissen, A.E. Rowan, R.J.M. Nolte, Self-Assembled Nanoreactors, Chem. Rev. 105 (2005) 1445–1489.

[29] P.M. Proulx-curry, N.D. Chasteen, Molecular aspects of iron uptake and storage in ferritin, Coord. Chem. Rev. 144 (1995) 347–368.

[30] B.K.K.W. Wong, S. Mann, Biomimetic synthesis of cadmium sulfide-ferritin nanocomposites, Adv. Mater. 8 (1996) 928–932.

[31] J.-W. Kim, S.H. Choi, P.T. Lillehei, S.-H. Chu, G.C. King, G.D. Watt, Cobalt oxide hollow nanoparticles derived by bio-templating., Chem. Commun. (Camb). (2005) 4101–4103. doi:10.1039/b505097a.

[32] Washington University, (2000), http://www.chemistry.wustl.edu/~edudev/LabTutorials/Ferritin/Ferritin.html. [Last accessed on 17.02.2015]

[33] S. Levisq, A. Luzzagoll, G. Cesarenill, A. Cozzis, F. Franceschinellis, A. Albertiniss, et al., Mechanism of Ferritin Iron Uptake : Activity of the H-chain and Deletion Mapping of the Ferro-oxidase Site, J. Biol. Chem. 263 (1988) 18086–18092.

[34] R.R. Crichton, Structure and function of ferritin., Angew. Chem. Int. Ed. Engl. 12 (1973) 57–65. doi:10.1002/anie.197300571.

[35] X. Yang, P. Arosio, N.D. Chasteen, Molecular Diffusion into Ferritin : Pathways , Temperature Dependence , Incubation Time , and Concentration Effects, Biophys. J. 78 (2000) 2049–2059.

[36] T. Douglas, D.R. Ripoll, Calculated electrostatic gradients in recombinant human H-chain femtin, Protein Sci. 7 (1998) 1083–1091.

[37] E. Simsek, M. Akif Kilic, Magic ferritin: A novel chemotherapeutic encapsulation bullet, J. Magn. Magn. Mater. 293 (2005) 509–513. doi:10.1016/j.jmmm.2005.01.066.

[38] J. Lee, H. Seo, E. Jeon, O.S. Park, K. Lee, C. Park, et al., Cooperative Activity of Subunits of Human Ferritin Heteropolymers in Escherichia coli, Biochem. Mol. Biol. 34 (2001) 365–370.

[39] F. Structure, E.C. Theil, Ferritin: Structure, Gene Regulation, And Cellular Function In Animals, Plants, And Microorganisms, Ann. Rev. Biochem. 56 (1987) 289–315.

[40] I. Bjork, W.W. Fish, Native and Subunit Molecular Weights of Apoferritin, Biochemistry. 10 (1969) 2844–2848.

[41] D.M. Lawson, A. Treffry, P.J. Artyrniuk, P.M. Harrison, S.J. Yewdall, A. Luzzago, et al., Identification of the ferroxidase centre in ferritin, Febs Lett. 254 (1989) 207–210.

[42] N.D. Chasteen, P.M. Harrison, Mineralization in ferritin: an efficient means of iron storage., J. Struct. Biol. 126 (1999) 182–94. doi:10.1006/jsbi.1999.4118.

[43] P. Santambrogio, S. Levi, A. Cozzi, B. Corsi, P. Arosio, Evidence that the specificity of iron incorporation into homopolymers of human ferritin L- and H-chains is conferred by the nucleation and ferroxidase centres, Biochem. J. 314 (1996) 139–144.

[44] G. Zhao, F. Bou-Abdallah, P. Arosio, S. Levi, C. Janus-Chandler, N.D. Chasteen, Multiple pathways for mineral core formation in mammalian apoferritin. The role of hydrogen peroxide., Biochemistry. 42 (2003) 3142–50. doi:10.1021/bi027357v.

[45] S. Levi, S.J. Yewdall, P.M. Harrison, P. Santambrogio, A. Cozzi, E. Rovida, et al., Evidence that H- and L-chains have co-operative roles in the iron-uptake mechanism of human ferritin, Biochem. J. 288 (1992) 591–596.

[46] N. Gálvez, B. Fernandez, E. Valero, P. Sánchez, R. Cuesta, J.M. Domínguez-Vera, Apoferritin as a nanoreactor for preparing metallic nanoparticles, C. R. Chim. 11 (2008) 1207–1212. doi:10.1016/j.crci.2008.09.003.

[47] F.K. Kálmán, S. Geninatti-Crich, S. Aime, Reduction/dissolution of a beta-MnOOH nanophase in the ferritin cavity to yield a highly sensitive, biologically compatible magnetic resonance imaging agent., Angew. Chem. Int. Ed. Engl. 49 (2010) 612–5. doi:10.1002/anie.200904731.

[48] C.C. Jolley, M. Uchida, C. Reichhardt, R. Harrington, S. Kang, M.T. Klem, et al., Size and crystallinity in protein-templated inorganic nanoparticles., Chem. Mater. 22 (2010) 4612–4618. doi:10.1021/cm100657w.

[49] T. Douglas, V.T. Stark, Nanophase Cobalt Oxyhydroxide Mineral Synthesized within the Protein Cage of Ferritin, Inorg. Chem. 39 (2000) 1828–1830.

[50] O. Kasyutich, A. Ilari, A. Fiorillo, D. Tatchev, A. Hoell, P. Ceci, Silver Ion Incorporation and Nanoparticle Formation inside the Cavity of Pyrococcus furiosus Ferritin : Structural and Size-Distribution Analyses, J. Am. Chem. Soc. 132 (2010) 3621–3627.

[51] C. Sun, H. Yang, Y. Yuan, X. Tian, L. Wang, Y. Guo, et al., Controlling assembly of paired gold clusters within apoferritin nanoreactor for in vivo kidney targeting and biomedical imaging., J. Am. Chem. Soc. 133 (2011) 8617–24. doi:10.1021/ja200746p.

[52] D. Ensign, M. Young, T. Douglas, Photocatalytic synthesis of copper colloids from CuII by the ferrihydrite core of ferritin., Inorg. Chem. 43 (2004) 3441–6. doi:10.1021/ic035415a.

[53] N. Galvez, P. Sanchez, J.M. Dominguez-Vera, A. Soriano-Portillo, M. Clemente-Leon, E. Coronado, Apoferritin-encapsulated Ni and Co superparamagnetic nanoparticles, J. Mater. Chem. 16 (2006) 2757–2761. doi:10.1039/b604860a.

[54] E. Valero, S. Tambalo, P. Marzola, M. Ortega-mu, F.L. Javier, F. Santoyo-gonz, et al., Magnetic Nanoparticles-Templated Assembly of Protein Subunits : A New Platform for Carbohydrate-Based MRI Nanoprobes, J. Am. Chem. Soc. 133 (2010) 4889–4895.

[55] B. Hennequin, L. Turyanska, T. Ben, A.M. Beltrán, S.I. Molina, M. Li, et al., Aqueous Near-Infrared Fluorescent Composites Based on Apoferritin-Encapsulated PbS Quantum Dots, Adv. Mater. 20 (2008) 3592–3596. doi:10.1002/adma.200800530.

[56] S. Aime, L. Frullano, Compartmentalization of a Gadolinium Complex in the Apoferritin Cavity : A Route To Obtain High Relaxivity Contrast Agents for Magnetic Resonance Imaging, Angew. Chem. Int. Ed. Engl. 521 (2002) 2001–2003.

[57] Z. Yang, X. Wang, H. Diao, J. Zhang, H. Li, H. Sun, et al., Encapsulation of platinum anticancer drugs by apoferritin, Chem. Commun. 7345 (2007) 3453–3455. doi:10.1039/b705326f.

[58] B. Fernández, N. Gálvez, P. Sánchez, R. Cuesta, R. Bermejo, J.M. Domínguez-Vera, Fluorescence resonance energy transfer in ferritin labeled with multiple fluorescent dyes., J. Biol. Inorg. Chem. 13 (2008) 349–55. doi:10.1007/s00775-007-0323-x.

[59] K.K.W. Wong, N.T. Whilton, T. Douglas, S. Mann, H. Cölfen, Hydrophobic proteins: synthesis and characterisation of organic-soluble alkylated ferritins, Chem. Commun. (1998) 1621–1622. doi:10.1039/a802627k.

[60] J. Swift, W.A. Wehbi, B.D. Kelly, X.F. Stowell, J.G. Saven, I.J. Dmochowski, et al., Design of Functional Ferritin-Like Proteins with Hydrophobic Cavities, J. Am. Chem. Soc. 128 (2006) 6611–6619.

[61] N. Gálvez, B. Fernández, P. Sánchez, J. Morales-Sanfrutos, F. Santoyo-González, R. Cuesta, et al., Magnetic–fluorescent Langmuir–Blodgett films of fluorophore-labeled ferritin nanoparticles, Solid State Sci. 11 (2009) 754–759. doi:10.1016/j.solidstatesciences.2008.04.026.

[62] M.V. Clavijo Jordan, S.C. Beeman, E.J. Baldelomar, K.M. Bennett, Disruptive chemical doping in a ferritin-based iron oxide nanoparticle to decrease r2 and enhance detection with T1-weighted MRI., Contrast Media Mol. Imaging. 9 (2014) 323–32. doi:10.1002/cmmi.1578.

[63] A. Makino, H. Harada, T. Okada, H. Kimura, H. Amano, H. Saji, et al., Effective encapsulation of a new cationic gadolinium chelate into apoferritin and its evaluation as an MRI contrast agent., Nanomedicine. 7 (2011) 638–46. doi:10.1016/j.nano.2011.01.015.

[64] X. Lin, J. Xie, G. Niu, F. Zhang, H. Gao, M. Yang, et al., Chimeric Ferritin Nanocages for Multiple Function Loading and Multimodal Imaging, Nano Lett. 11 (2010) 814–819.

[65] F.C. Meldrum, B.R. Heywood, S. Mann, Magnetoferritin : In Vitro Synthesis of a Novel Magnetic Protein, Science 257 (1992) 522–523.

[66] K.K.W. Wong, T. Douglas, S. Gider, D.D. Awschalom, S. Mann, Biomimetic Synthesis and Characterization of Magnetic Proteins (Magnetoferritin), Chem. Mater. 4756 (1998) 279–285.

[67] D.P.E. Dickson, S. A. Walton, S. Mann, K. Wong, Properties of magnetoferritin: A novel biomagnetic nanoparticle, Nanostructured Mater. 9 (1997) 595–598. doi:10.1016/S0965-9773(97)00133-5.

[68] B.R. Jarrett, D.L. Kukis, A.Y. Louie, Synthesis of Cu 64-Labeled Magnetic Nanoparticles for Multimodal Imaging, Bioconjug. Chem. 19 (2008) 1496–1504.

[69] M. Hamoudeh, M.A. Kamleh, R. Diab, H. Fessi, Radionuclides delivery systems for nuclear imaging and radiotherapy of cancer., Adv. Drug Deliv. Rev. 60 (2008) 1329–46. doi:10.1016/j.addr.2008.04.013.

[70] R. Schibli, R. Schwarzbach, R. Alberto, K. Ortner, H. Schmalle, Steps toward High Specific Activity Labeling of Biomolecules for Therapeutic Application : Preparation of Precursor $[^{188}Re(H_2O)_3(CO)_3]^+$ and Synthesis of Tailor-Made Bifunctional Ligand Systems, Bioconjug. Chem. 3 (2002) 750–756.

[71] J. Cao, Y. Wang, J. Yu, J. Xia, Preparation and radiolabeling of surface-modified magnetic nanoparticles with rhenium-188 for magnetic targeted radiotherapy, J. Magn. Magn. Mater. 277 (2004) 165–174. doi:10.1016/j.jmmm.2003.10.022.

[72] F.L. Thorp-Greenwood, M.P. Coogan, Multimodal radio - (PET/SPECT) and fluorescence imaging agents based on metallo-radioisotopes: current applications and prospects for development of new agents., Dalton Trans. 40 (2011) 6129–43. doi:10.1039/c0dt01398f.

[73] R. Tavaré, J. Williams, K. Howland, P.J. Blower, G.E.D. Mullen, $[Re(CO)_3]^+$ labelling of a novel cysteine/hexahistidine tag : Insights into binding mode by liquid chromatography-mass spectrometry, J. Inorg. Biochem. 114 (2012) 24–27. doi:10.1016/j.jinorgbio.2012.04.006.

[74] G. Wunderlich, J. Pinkert, M. Andree, M. Stintz, F.F.K. Jr, J. Kropp, et al., Preparation and biodistribution of rhenium-188 labeled albumin microspheres B 20 : a promising new agent for radiotherapy, Appl. Radiat. Isot. 52 (2000) 63–68.

[75] M. Hamoudeh, H. Salim, D. Barbos, C. Paunoiu, H. Fessi, Preparation and characterization of radioactive dirhenium decacarbonyl-loaded PLLA nanoparticles for radionuclide intra-tumoral therapy., Eur. J. Pharm. Biopharm. 67 (2007) 597–611. doi:10.1016/j.ejpb.2007.04.003.

[76] G. Pauer, S. Failing, G. Tapolsky, Radiolabeling of magnetic particles with rhenium-188 for cancer therapy, J. Magn. Magn. Mater. 225 (2001) 73–78.

[77] U. Abram, R. Alberto, Technetium and Rhenium - Coordination Chemistry and Nuclear Medical Applications, 17 (2006) 1486–1500.

[78] J. R. Dilworth, S. J. Parrott, The biomedical chemistry of technetium and rhenium, Chem. Soc. Rev. 27 (1998) 43–55.

[79] D.A. Skoog, F.J. Holler, S.R. Crouch, Principles of Instrumental Analysis, 5th ed., Harcourt Brace and Company, United States of America, 1998.

[80] Gustavus Adolphus College, http://homepages.gac.edu/~cellab/chpts/chpt4/intro4.html. [Last accessed on 17.02.2015]

[81] J.B. Hutchins, S.W. Barger, Why neurons die: cell death in the nervous system., Anat. Rec. 253 (1998) 79–90.

[82] Kimball's Biology Pages, 2014, http://users.rcn.com/jkimball.ma.ultranet/BiologyPages/A/Apoptosis.html. [Last accessed on 17.02.2015]

[83] Wikipedia, (2014), http://en.wikipedia.org/wiki/Necrosis. [Last accessed on 17.02.2015]

[84] P. Meier, A. Finch, G. Evan, Apoptosis in development, Nature. 407 (2000) 796–801.

[85] D.A. Scudiere, R.H. Shoemaker, K.D. Paul, A. Monks, S. Tierney, T.H. Nofziger, et al., Evaluation of a Soluble Tetrazolium/Formazan Assay for Cell Growth and Drug Sensitivity in Culture Using Human and Other Tumor Cell Lines, Cancer Res. 48 (1988) 4827–4833.

[86] BioChemica, (2015), https://www.applichem.com/en/literature/applications/no-12-cell-proliferation-assay-xtt/. [Last accessed on 17.02.2015]

[87] Catalog invitrogen, FITC Annexin V/Dead Cell Apoptosis Kit with FITC annexin V and PI , for Flow Cytometry, (2010) 1–5.

[88] Advanced Biochemical Engineering Class, https://seallab.wordpress.com/research/7-cytotoxicity-measurements/. [Last accessed on 17.02.2015]

[89] H. Wei, E. Wang, Nanomaterials with enzyme-like characteristics (nanozymes): next-generation artificial enzymes., Chem. Soc. Rev. 42 (2013) 6060–93. doi:10.1039/c3cs35486e.

[90] Bio-Rad, (2015), http://www.bio-rad.com/en-us/applications-technologies/detection-methods. [Last accessed on 17.02.2015]

[91] L. Gao, J. Zhuang, L. Nie, J. Zhang, Y. Zhang, N. Gu, et al., Intrinsic peroxidase-like activity of ferromagnetic nanoparticles., Nat. Nanotechnol. 2 (2007) 577–83. doi:10.1038/nnano.2007.260.

[92] J. Fan, J.-J. Yin, B. Ning, X. Wu, Y. Hu, M. Ferrari, et al., Direct evidence for catalase and peroxidase activities of ferritin-platinum nanoparticles., Biomaterials. 32 (2011) 1611–8. doi:10.1016/j.biomaterials.2010.11.004.

[93] L. Ottobrini, P. Ciana, a Biserni, G. Lucignani, a Maggi, Molecular imaging: a new way to study molecular processes in vivo., Mol. Cell. Endocrinol. 246 (2006) 69–75. doi:10.1016/j.mce.2005.11.013.

[94] M. Terashima, M. Uchida, H. Kosuge, P.S. Tsao, M.J. Young, S.M. Conolly, et al., Human ferritin cages for imaging vascular macrophages., Biomaterials. 32 (2011) 1430–7. doi:10.1016/j.biomaterials.2010.09.029.

[95] M. Uchida, M. Terashima, C.H. Cunningham, Y. Suzuki, D. Willits, A.F. Willis, et al., A human ferritin iron oxide nano-composite magnetic resonance contrast agent., Magn. Reson. Med. 60 (2008) 1073–81. doi:10.1002/mrm.21761.

[96] D.G. Mitchell, M.S. Cohen, MRI principles, 2. ed., Elsevier, Pennsylvania, 1999.

[97] McGraw-Hill Higher Education, (2000), http://www.mhhe.com/physsci/chemistry/carey/student/olc/ch13nmr.html. [Last accessed on 17.02.2015]

[98] Wikidoc, (2008), http://wikidoc.org/index.php/Basic_MRI_Physics. [Last accessed on 17.02.2015]

[99] R.B. Lauffer, Paramagnetic metal complexes as water proton relaxation agents for NMR imaging: theory and design, Chem. Rev. 87 (1987) 901–927. doi:10.1021/cr00081a003.

[100] L. Helm, Relaxivity in paramagnetic systems: Theory and mechanisms, Prog. Nucl. Magn. Reson. Spectrosc. 49 (2006) 45–64.

[101] J.R. Hwu, Y.S. Lin, T. Josephrajan, M.-H. Hsu, F.-Y. Cheng, C.-S. Yeh, et al., Targeted Paclitaxel by conjugation to iron oxide and gold nanoparticles., J. Am. Chem. Soc. 131 (2009) 66–8. doi:10.1021/ja804947u.

[102] L. Babes, J. Jacques, L. Jeune, P. Jallet, Synthesis of Iron Oxide Nanoparticles Used as MRI Contrast Agents : A Parametric Study, J. Colloid Interface Sci. 482 (1999) 474–482.

[103] C. Sun, J.S.H. Lee, M. Zhang, Magnetic nanoparticles in MR imaging and drug delivery., Adv. Drug Deliv. Rev. 60 (2008) 1252–65.

[104] G.-P. Yan, L. Robinson, P. Hogg, Magnetic resonance imaging contrast agents: Overview and perspectives, Radiography. 13 (2007) 5–19. doi:10.1016/j.radi.2006.07.005.

[105] S. Laurent, D. Forge, M. Port, A. Roch, C. Robic, L. Vander Elst, et al., Magnetic iron oxide nanoparticles: synthesis, stabilization, vectorization, physicochemical characterizations, and biological applications., Chem. Rev. 108 (2008) 2064–110. doi:10.1021/cr068445e.

[106] E. Strable, J.W.M. Bulte, B. Moskowitz, K. Vivekanandan, M. Allen, T. Douglas, Synthesis and Characterization of Soluble Iron Oxide - Dendrimer Composites, Chem Mater. 13 (2001) 2201–2209.

[107] C. Sangregorio, J.K. Wiemann, C.J. O'Connor, Z. Rosenzweig, A new method for the synthesis of magnetoliposomes, J. Appl. Phys. 85 (1999) 5699. doi:10.1063/1.370256.

[108] L.O. Liepold, M.J. Abedin, E.D. Buckhouse, J. a Frank, M.J. Young, T. Douglas, Supramolecular protein cage composite MR contrast agents with extremely efficient relaxivity properties., Nano Lett. 9 (2009) 4520–6. doi:10.1021/nl902884p.

[109] S. Aime, L. Calabi, C. Cavallotti, A new structural entry for an improved generation of MRI contrast agents, Inorg. Chem. 43 (2004) 7588–7590.

[110] P.H. Fries, E. Belorizky, Enhancement of the water proton relaxivity by trapping Gd3+ complexes in nanovesicles., J. Chem. Phys. 133 (2010) 024504. doi:10.1063/1.3456987.

[111] H. Shokrollahi, Contrast agents for MRI, Mater. Sci. Eng. C. 33 (2013) 4485–97. doi:10.1016/j.msec.2013.07.012.

[112] D.K. Kim, M. Mikhaylova, F.H. Wang, J. Kehr, Starch-Coated Superparamagnetic Nanoparticles As MR Contrast Agents, Chem Mater. 15 (2003) 4343–4351.

[113] S. Mornet, S. Vasseur, F. Grasset, E. Duguet, Magnetic nanoparticle design for medical diagnosis and therapy, J. Mater. Chem. 14 (2004) 2161. doi:10.1039/b402025a.

[114] K. Müller, J.N. Skepper, M. Posfai, R. Trivedi, S. Howarth, C. Corot, et al., Effect of ultrasmall superparamagnetic iron oxide nanoparticles (Ferumoxtran-10) on human monocyte-macrophages in vitro., Biomaterials. 28 (2007) 1629–42. doi:10.1016/j.biomaterials.2006.12.003.

[115] J. Terrovitis, M. Stuber, A. Youssef, S. Preece, M. Leppo, E. Kizana, et al., Magnetic resonance imaging overestimates ferumoxide-labeled stem cell survival after transplantation in the heart, Circulation. 117 (2008) 1555–62.

[116] J.W.M. Bulte, T. Douglas, S. Mann, R.B. Frankel, Magnetoferritin : Characterization of a Novel Superparamagnetic MR Contrast Agent, J. Magn. Reson. Imaging. 24 (2008) 497–505.

[117] J.W.M. Bulte, T. Douglas, S. Mann, et al, Biomineralization as a novel molecular approach in the design of iron oxide based magnetic resonance contrast agents, Invest. Radiol. 29 (1994) 12–14.

[118] M. Bradford, A Rapid and Sensitive Method for the Quantitation of Microgram Quantities of Protein Utilizing the Principle of Protein-Dye Binding, Anal. Biochem. 72 (1976) 248–254. doi:10.1006/abio.1976.9999.

[119] Crystal Structure, http://www.geocities.jp/ohba_lab_ob_page/structure6.html. [Last accessed on 17.02.2015]

[120] J. Cao, Y. Wang, J. Yu, J. Xia, C. Zhang, D. Yin, et al., Preparation and radiolabeling of surface-modified magnetic nanoparticles with rhenium-188 for magnetic targeted radiotherapy, J. Magn. Magn. Mater. 277 (2004) 165–174. doi:10.1016/j.jmmm.2003.10.022.

[121] M. Bapna, et al, Spectrophotometric Determination of Histidine Hydrochloride Monohydrate in Pharmaceutical Formulations, Int. J. Pharmtech Res. 1 (2009) 852–856.

APPENDIX A

A: Cell Cycle Histograms of MDA-MB-231 Cells

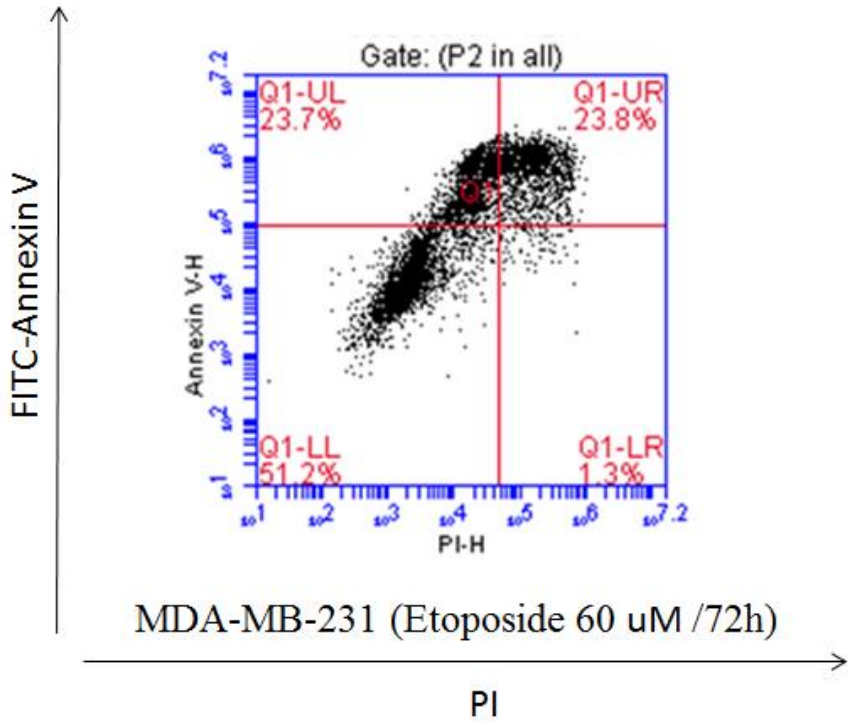

Figure 1. The cell cycle histogram of MDA-MB-231 for etoposide.

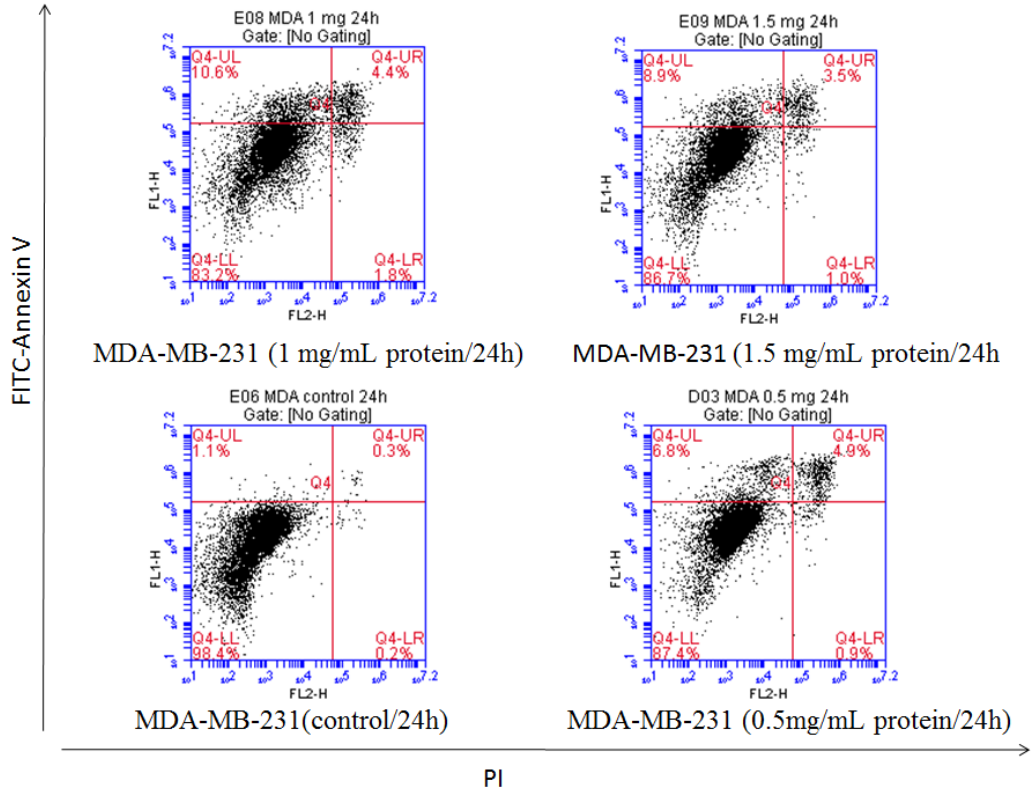

Figure 2. The cell cycle histogram of MDA-MB-231 for protein samples for 24h.

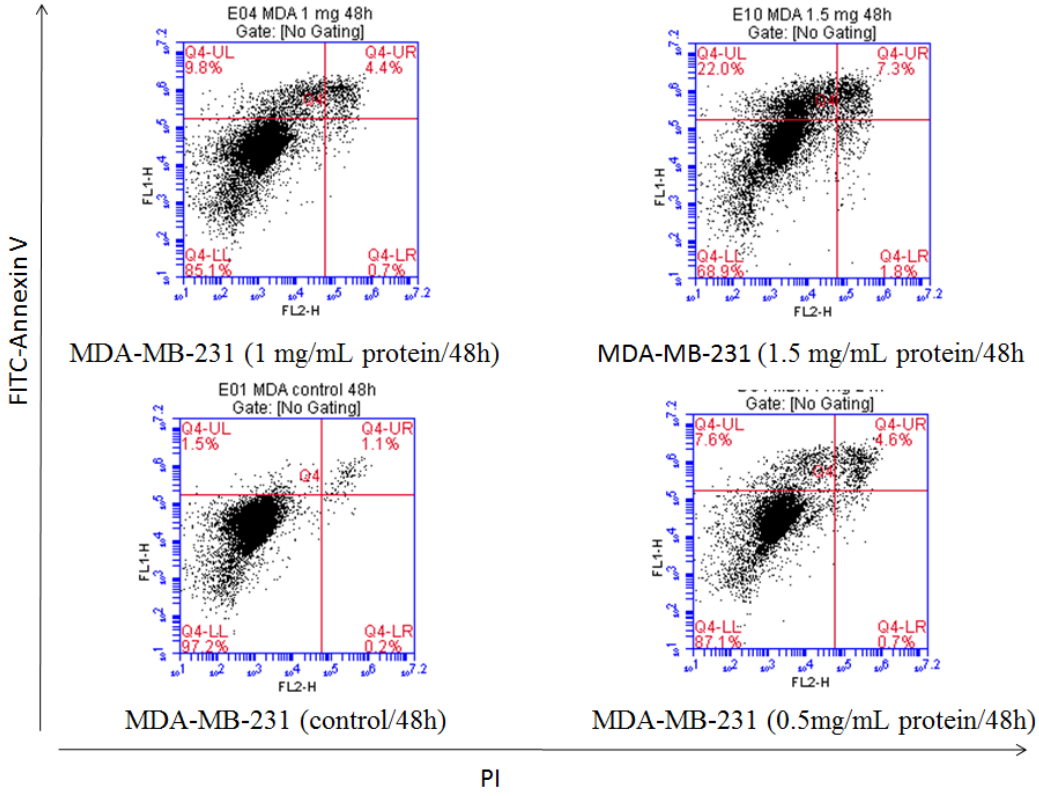

Figure 3. The cell cycle histogram of MDA-MB-231 for protein samples for 48h.

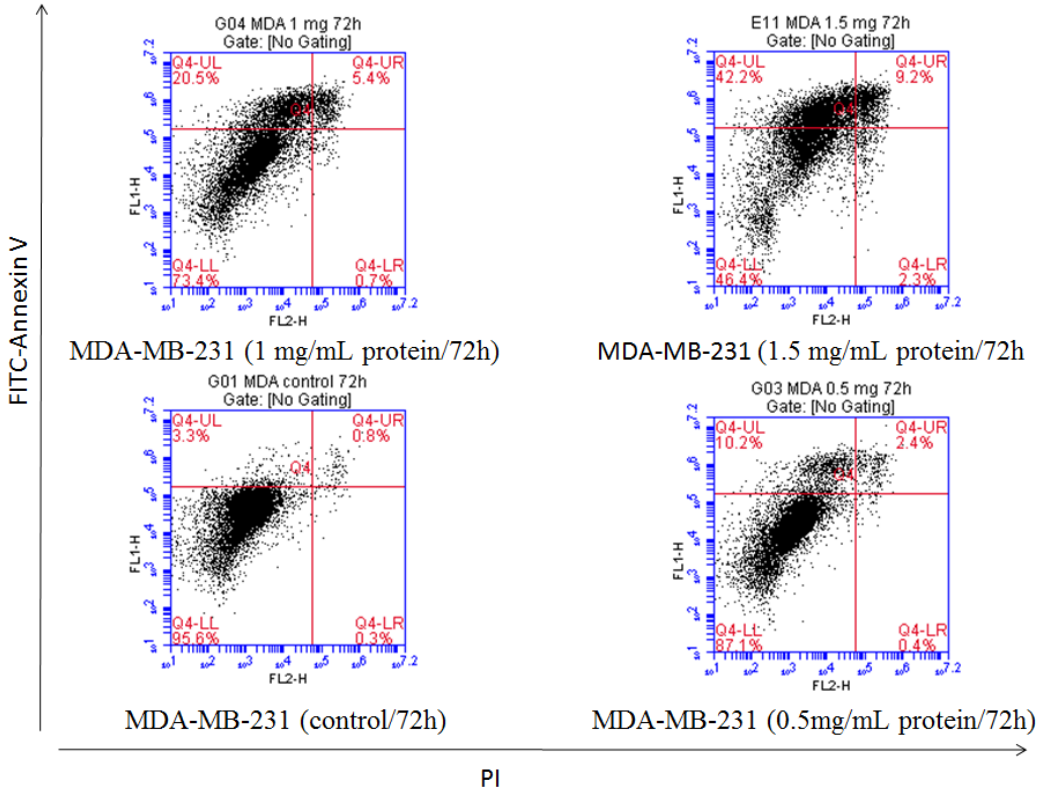

Figure 4. The cell cycle histogram of MDA-MB-231 for protein samples for 72h.

APPENDIX B

B: Cell Cycle Histograms of MCF-10A Cells

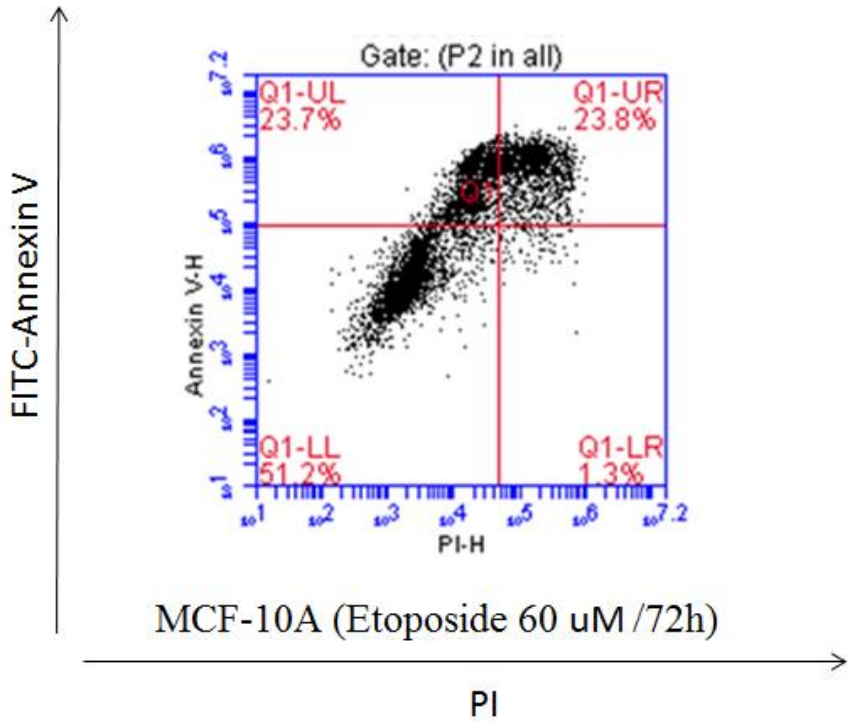

Figure 5. The cell cycle histogram of MCF-10A for etoposide.

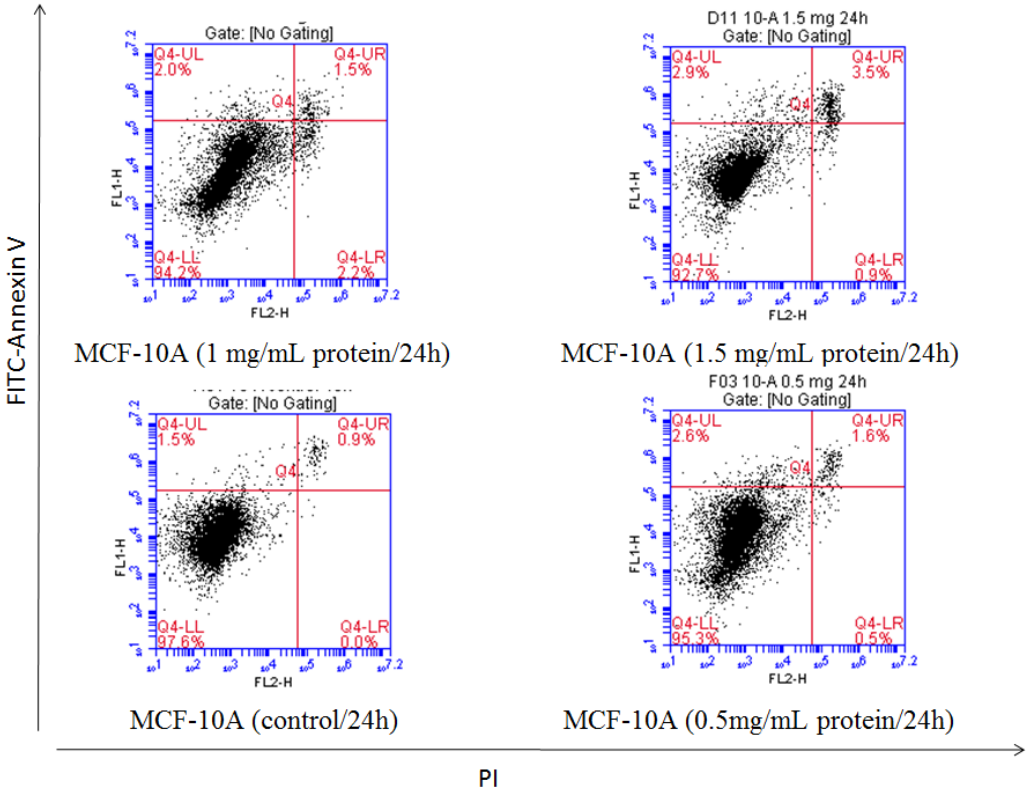

Figure 6. The cell cycle histogram of MCF-10A for protein samples for 24h.

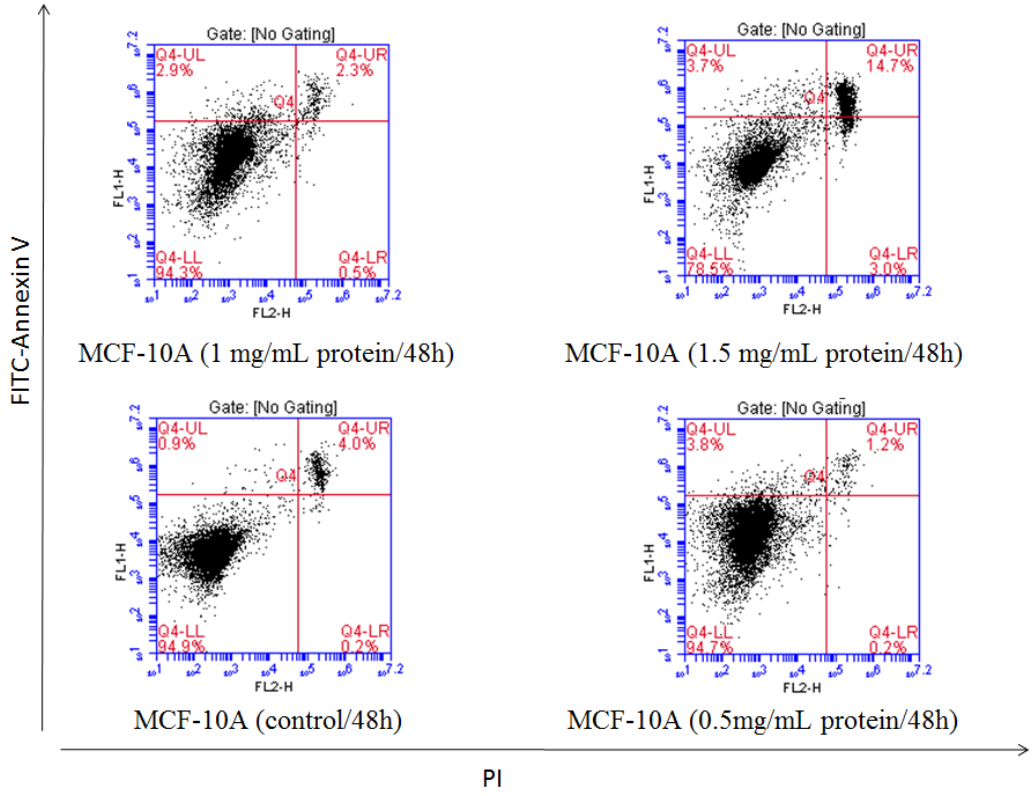

Figure 7. The cell cycle histogram of MCF-10A for protein samples for 48h.

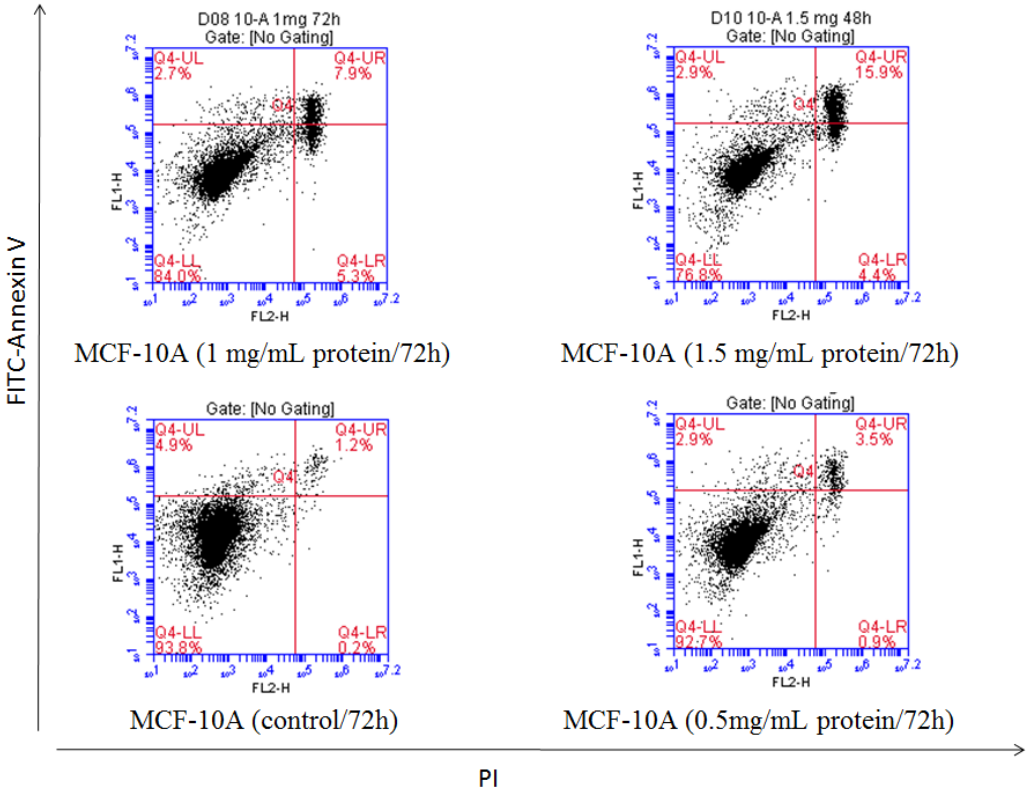

Figure 6. The cell cycle histogram of MCF-10A for protein samples for 72h.

VITA

Tuğba Nur Aslan

Tel: +90 505 857 4270

e-mail: tugba_nur_alp@yahoo.com.tr

Education	**1999-2003 BS Degree in Chemistry** Ege University - İzmir, Turkey **2003-2005 MSc Degree in Chemistry** Ege University - İzmir, Turkey
Working Experience	**01/2007- to date** Chemistry Department - METU Research Assistant
Publication	Hüseyin Yıldıran, Sevda Ayata, Sevgi Arzık, Tuğba Nur Alp, 'A theoretical study on calculation of absolute hydration enthalpies for some univalent ions', Ionics, 14, 541–543, 2008.